

**PROCESSING, STRUCTURE, PROPERTIES, AND JOULE
HEATING APPLICATION OF POLYACRYLONITRILE /CARBON
NANOTUBES COMPOSITE FIBERS**

A Dissertation
Presented to
The Academic Faculty

by

Mingxuan Lu

In Partial Fulfillment
of the Requirements for the Degree
Doctor of Philosophy in the
School of Chemical & Biomolecular Engineering

Georgia Institute of Technology
December 2020

COPYRIGHT © 2020 BY MINGXUAN LU

**PROCESSING, STRUCTURE, PROPERTIES, AND JOULE
HEATING APPLICATION OF POLYACRYLONITRILE /CARBON
NANOTUBES COMPOSITE FIBERS**

Approved by:

Dr. Satish Kumar, Advisor
School of Materials Science and
Engineering
Georgia Institute of Technology

Dr. J. Carson Meredith, Co-advisor
School of School of Chemical &
Biomolecular Engineering
Georgia Institute of Technology

Dr. Victor Breedveld
School of School of Chemical &
Biomolecular Engineering
Georgia Institute of Technology

Dr. William J. Koros
School of School of Chemical &
Biomolecular Engineering
Georgia Institute of Technology

Dr. Donggang Yao
School of Materials Science and
Engineering
Georgia Institute of Technology

Date Approved: Nov 23, 2020

ACKNOWLEDGEMENTS

First of all, I would like to thank my advisor, Dr. Satish Kumar, for his guidance and support throughout my study. I am particularly thankful for his advice and emphasis on critical thinking and decision-making that help me grow as a student and as a researcher. I would like to thank my co-advisor, Dr. Carson Meredith, and my committee member Dr. Victor Breedveld for their contribution of time and expertise in my research. Without their guidance and suggestions, the completion of the thesis would not be possible. I am thankful to Dr. William Koros and Dr. Donggang Yao for taking their time to serve on my thesis committee and for their advice on my research.

I am grateful to Dr. Huibin Chang, Dr. Prabhakar Gulgunje, Dr. Po-Hsiang Wang, and Dr. Jeffrey Luo for teaching me their experimental methods. I am thankful to Dr. Kishor Gupta, Pedro J. Arias-Monje, Jyotsna Ramachandran, Mohammad Hamza Kirmani, Narayan Shirolkar, Adam Maffe, and Jiawei Xu for their help with various experiments and discussions. I want to thank my collaborator Jianshan Liao for helping with rheological studies and Dr. Sandip Agarwal from Vuronyx Technologies for helping with the Joule heating studies. I am grateful to the U.S. Department of Energy and U. S. Air Force Office of Scientific Research for funding the research.

Finally, I would like to thank my parents and my fiancée for their support, understanding, and encouragement. I am also grateful to all my friends throughout my studies.

TABLE OF CONTENTS

ACKNOWLEDGEMENTS	iii
LIST OF TABLES	vi
LIST OF FIGURES	viii
SUMMARY	xiii
CHAPTER 1. Introduction	1
1.1 PAN and PAN fiber	1
1.2 Carbon nanotubes (CNT) and polymer/CNT composites	3
1.3 Bi-component fiber	5
1.4 Rheological behavior of polymer nanocomposites	8
1.5 Stabilization of PAN	12
1.6 Joule heating applications	13
1.7 Thesis objectives	14
CHAPTER 2. Rheological Behavior and Fiber Spinning of Polyacrylonitrile (PAN)/Carbon Nanotube (CNT) Dispersions at High CNT Loading	15
2.1 Introduction	15
2.2 Experimental procedures	16
2.2.1 Materials	16
2.2.2 Solution and dispersion preparation	17
2.2.3 Solution and dispersion characterization	17
2.2.4 Fiber spinning	19
2.3 Results and discussion	19
2.4 Conclusion	31
CHAPTER 3. Structure, Properties, and Applications of Polyacrylonitrile (PAN)/Carbon Nanotube (CNT) Fibers at low CNT Loading	33
3.1 Introduction	33
3.2 Experimental procedures	33
3.3 Results and discussion	36
3.4 Conclusion	46
CHAPTER 4. Stabilization of Polyacrylonitrile (PAN) Fibers with Carbon Nanotubes (CNT)	48
4.1 Introduction	48
4.2 Experimental procedures	48
4.2.1 Materials	48
4.2.2 Fiber manufacturing	49
4.2.3 Fiber characterization	50
4.3 Results and discussion	51

4.4	Conclusion	63
CHAPTER 5. Continuous Stabilization of Polyacrylonitrile (PAN) - Carbon Nanotube (CNT) Fibers by Joule Heating		
5.1	Introduction	65
5.2	Experimental procedures	65
5.2.1	Materials	65
5.2.2	Solution preparation	66
5.2.3	Precursor fiber manufacturing	67
5.2.4	Fiber characterization	67
5.2.5	Joule heating and convective heating	68
5.3	Results and discussion	71
5.4	Conclusion	81
CHAPTER 6. Conclusion and Recommendations		
6.1	Conclusions	83
6.2	Recommendations	85
APPENDIX A. A Comprehensive Study of Polyacrylonitrile (PAN) in Various Solvents and Solvent Mixtures: Gelation Behavior, Gel Spinning, and Hansen's Solubility Parameter Predictions		
A.1	Introduction	88
A.2	Experimental procedures	89
A.3	Results and discussion	92
A.4	Conclusion	108
APPENDIX B. Supporting Information for Chapter 2		
APPENDIX C. Supporting Information for Chapter 3		
APPENDIX D. Supporting Information for Chapter 4		
APPENDIX E. Supporting Information for Chapter 5		
REFERENCES		
		131

LIST OF TABLES

Table 1.1	Summary of properties of core-sheath fibers incorporating with CNT.	7
Table 1.2	Rheological behavior of multiple polymer nanocomposites.	10
Table 3.1	Summary of processing parameters of bi-component PAN core and PAN-CNT sheath fibers.	38
Table 3.2	Structural parameters of PAN core and PAN-CNT sheath (90/10) fibers before annealing.	43
Table 3.3	Structural parameters of PAN core and PAN-CNT sheath fibers after annealing.	43
Table 3.4	Mechanical properties of the core-sheath fibers.	44
Table 3.5	Structural parameters, morphology, electrical conductivity, and mechanical properties of various A2 core-sheath fibers containing 4.4 wt% CNTs and different draw ratios.	45
Table 4.1	Area ratios, CNT wt%, draw ratios, and diameters of various fibers.	52
Table 5.1	Listing of CNT amount, draw ratio, diameter, and electrical conductivity for the fibers used in this study.	74
Table A1	Solution preparation and fiber spinning conditions of PAN in various solvents and solvent mixtures.	92
Table A2	Results of rheology study of solvent and solvent mixtures and relation to Hansen's solubility parameters.	98
Table A3	Summary of mechanical and structural properties of as-spun fibers from PAN/DMF and PAN/DMF/water solutions.	100
Table A4	Summary of mechanical and structural properties of fully drawn fibers from PAN/DMF and PAN/DMF/water solutions.	101
Table A5	Solvents and solvent mixtures for PAN that show low Hansen's solubility parameter R_a for PAN[79].	102
Table A6	DMF and solvent mixtures with DMF used for fiber spinning, and the resulting fiber tensile properties.	103
Table A7	Solubility parameters and complex viscosity of PAN in DMF, sulfolane, PC, sulfolane/PC, and sulfolane/toluene mixtures	105

Table A8	Solubility parameters and complex viscosity of PAN in DMF, sulfolane, PC, sulfolane/PC, and sulfolane/toluene mixtures	106
Table A9	Tensile properties and structural parameters of PAN precursor fibers made from DMF, sulfolane/PC (50/50), and from literature.	107
Table B1	Composition and processing parameters of pure PAN solution and of PAN/CNT and PAN/CNC dispersions.	110
Table B2	Log G' – log G'' slope when $\omega \rightarrow 0$ for PAN solution and PAN/CNT dispersions at different temperatures.	111
Table B3	Summary of fiber spinning parameters and continuous jetting time for PAN/CNT dispersions.	112
Table C1	Comparison of electrical conductivity measurement results from the 2-probe and 4-probe method for three select samples of 4.4 wt% CNT.	113
Table C2	Processing conditions and temperature measured by an IR sensor near the center of fibers bundle during Joule heating experiments.	113
Table C3	Summary of results from electrical conductivity measurements.	114
Table D1	Mechanical properties and structural parameters of PAN and PAN/CNT precursor fibers.	115
Table D2	Calculated kinetic parameters from Kissinger's equation.	117
Table E1	Summary of solution preparation and fiber spinning parameters for single and bi-component fibers.	122
Table E2	Joule heating conditions for single-component fibers.	123
Table E3	Joule heating conditions for bi-component fibers.	123
Table E4	The electrical conductivity of single and bi-component fibers before and after various annealing conditions.	123
Table E5	Summary of tensile properties and structural parameters for single and bi-component precursor fibers used for this study.	125

LIST OF FIGURES

Figure 1.1	Chemical structure of monomer repeat unit of PAN.	1
Figure 2.1	The scheme of the fiber gel spinning apparatus.	19
Figure 2.2	Shear viscosity (η , open symbols), and complex viscosity (η^* , solid symbols) of PAN/DMF and PAN/CNT/DMF samples at ~ 7 g/dL solid content, as measured at 20 °C.	21
Figure 2.3	(a) Log-log plot of G' versus G'' , and (b) loss factor ($\tan \delta$) as a function of frequency ω for PAN/DMF and PAN/CNT/DMF systems at ~ 7 g/dL solid content. as measured at 20 °C.	22
Figure 2.4	Log-log plot of G' versus G'' of (a) PAN, (b) PAN/CNT-4, (c) PAN/CNT-10, and (d) PAN/CNT-15 at various temperatures in the frequency range 0.63 – 242 rad/s.	25
Figure 2.5	Temperature response of $\tan \delta$ for PAN, PAN/CNT-4, PAN/CNT-10, and PAN/CNT-15 from dynamic frequency measurements at oscillatory frequencies of (a) 1 rad/s, and (b) 93.5 rad/s.	25
Figure 2.6	(a) Log-log plot of G' versus G'' , and (b) $\tan \delta$ as a function of ω for PAN/CNT dispersions at 7 g/dL (PAN/CNT-10), 4.5 g/dL (PAN/CNT-10 Dilute), and 11.5 g/dL (PAN/CNT-10-2); data measured for all samples at 20°C across the frequency range 0.63 – 242 rad/s	27
Figure 2.7	Schematic log-log plot of G' versus G'' of (a) PAN solution, or PAN/CNT at low CNT loading (0 or 4 wt% CNT); (b) highly elastic-like PAN/CNT dispersion at high CNT loading (15 wt% CNT), (c) relatively dilute PAN/CNT dispersion at high CNT loading(10 wt% CNT), and (d) PAN/CNT at high CNT loading(10 wt% CNT) with reduced elasticity relative to (b). Arrows indicate the direction of increasing frequency (ω). <input checked="" type="checkbox"/> indicates that the solution/dispersion is desirable for continuous fiber spinning, <input type="checkbox"/> indicates that the dispersion is not desirable for continuous fiber spinning; the formulation may lead to failure to jetting, frequent breakage of fiber spinning, or require spinning with low shear.	29
Figure 2.8	(a) Log-log plot of G' versus G'' , and (b) $\tan \delta$ as a function of ω for PAN/CNC dispersions measured at room temperature. Rheology data of PAN/CNC-20 and PAN/CNC-40 are from a study by Chang et al. [53]. PAN/CNC-60 was made in this work following the previous protocol.	30
Figure 3.1	Optical micrographs of PAN core and PAN-CNT sheath (with 10 wt% CNT in the sheath) bi-component fibers.	40

Figure 3.2	Scanning electron micrographs of A1 fibers embedded in epoxy. (a) low magnification image. (b) higher magnification image showing core-sheath interface morphology. (c) High magnification image showing CNTs embedded in PAN in the fiber sheath.	40
Figure 3.3	Electrical conductivity of (a) PAN core PAN-CNT sheath as-spun fibers with different CNT wt%. (b) A2 fibers after annealing for 30 minutes at different temperatures. (c) A2 fibers with various annealing times at 180°C. (d) A2 drawn fibers at 3 and 30 minutes of annealing at 180 °C. A2-2 pre-annealed fiber conductivity could not be measured and is less than 10 ⁻⁴ S/m.	42
Figure 3.4	(a) before annealing, (b) after annealing at 210 °C for 30 minutes at constant length, (c, d, e) Joule heating (JH) between 1.2 – 1.5 kV for 1, 2, and 3 hours. (a) before annealing, (b) after annealing at 210 °C for 30 minutes at constant length, (c, d, e) Joule heating (JH) between 1.2 – 1.5 kV for 1, 2, and 3 hours.	46
Figure 4.1	Optical image of cross-sections of as-spun fibers of (a) PAN, (b) PAN/CNT-1, (c) PAN/CNT-2, and (d) PAN/CNT-3. The scale bar represents 100 μm. PAN/CNT (10wt%) appears in black color in these optical images.	52
Figure 4.2	DSC curves of PAN, PAN/CNT fibers, and PAN powder under (a) air and (b) N ₂ at 10 °C/min. The area under the DSC curves was used to calculate the heat of reaction, as shown in Figure D1.	54
Figure 4.3	The heat of stabilization ($\Delta H_{reaction}$) of various samples in air and in N ₂ . $\Delta H_{reaction}$ of PAN/CNT fibers were corrected for PAN weight percentage.	54
Figure 4.4	Activation energies (E_a) with different $A_{PAN-CNT}/A_{total}$ area ratios.	57
Figure 4.5	Integrated WAXD scans of PAN and PAN/CNT-2 fibers after stabilization in the air for the indicated times.	59
Figure 4.6	Representative surface (upper) and cross-section (lower) of (a)&(d) PAN, (b)&(e) PAN/CNT-2, (c)&(f) PAN/CNT-3 precursor fibers before stabilization.	61
Figure 4.7	Representative surface (upper) and cross-section (middle and lower) of (a), (d)&(g) PAN, (b), (e)&(h) PAN/CNT-2, (c), (f)&(i) PAN/CNT-3 fibers after stabilization.	61
Figure 4.8	Schematic plot of core-sheath fibers with PAN/CNT sheath during stabilization.	63
Figure 5.1	Continuous resistive stabilizer (CoRe-Stab) for Joule heating. Inset shows the Joule heating schematic.	71

Figure 5.2	Optical micrographs of fiber cross-sections of (a) single-component and (b) bi-component core-sheath geometry fibers.	73
Figure 5.3	Integrated WAXD radial scans of single-component fibers. (a) before annealing, (b) after continuous annealing at 210 °C for 30-minutes, (c) after Joule heating for 30 minutes, (d) after Joule heating for 60 minutes. WAXD radial scans (e, f, g, h) after stabilization in the oven at 250 °C for varying times are given for comparison. Stabilization times in oven are: (e) 30 minutes, (f) 60 minutes, (g) 120 minutes, and (h) 150 minutes.	75
Figure 5.4	Integrated WAXD radial scans of bi-component fibers. (a) before annealing, (b) after continuous annealing at 210 °C for 10 minutes, (c) after Joule heating of 6000 filaments tow for 2 hours, (d) after Joule heating of 1000 filaments tow for 4 hours. WAXD radial scans (e, f, g, h) of 1000 filaments tow after stabilization in the oven at 250 °C for varying times are given for comparison. Stabilization times in the oven are (e) 2 hours, (f) 4 hours, (g) 8 hours, and (h) 12 hours.	77
Figure 5.5	FTIR spectra of bi-component fibers. (a) before Joule heating, (b) after 2-hour Joule heating using 6000 filaments tow, (c) after 4 hours Joule heating using 1000 filaments tow, and (d) after 4-hour stabilization in a 250 °C convection oven in the air using 1000 filaments tow.	78
Figure 5.6	Distribution of energy consumed during Joule heating according to equation 5-1 of (left) single-component fibers for 1 hour Joule heating with 200 filaments tow, and (right) bi-component fibers during for 4 hours Joule heating with 1000 filaments tow.	80
Figure 5.7	Energy consumption for convective heating[166,171], and for Joule heating from equation 5-1. Joule heating values are for bi-component fibers for 4 hours for 1000 filament tow. The optimized value is calculated assuming that heat loss can be eliminated by insulation but that heat loss due to airflow inside the tube still occurs. The minimum value only includes the energy required to heat up the fibers to 250 °C for stabilization during Joule heating.	81
Figure A1	Complex viscosity (η^*) versus frequency (ω) at various temperatures. (a) PAN/DMF, (b) PAN/DMF/Water (with 4 vol % water); (c) PAN/DMF/Water (with 7 vol % water); (d) PAN/DMF/toluene (with 7 vol % toluene). The slopes of the η^* curves are shown in the figure.	94
Figure A2	$\tan \delta$ as a function of temperature at various frequencies of PAN solution in DMF with water or toluene. (a) only DMF, with no water or toluene, (b) 4 vol % water, (c) 7 vol % water, (d) 7 vol % toluene.	95
Figure A3	$\log G'$ versus $\log G''$ curves for PAN solution from 50 °C to gelation temperature in DMF with water or toluene. . (a) only DMF, with no water or toluene, (b) 4 vol % water, (c) 7 vol % water, (d) 7 vol % toluene. The slopes of the curves are shown in the figure.	96

Figure A4	Correlation between gelation temperature (T_{gel}) and Hansen's solubility parameter δ . Red square showed the T_{gel} from ref [14], Blue rectangle showed the T_{gel} from ref [18]. Solid line is used to visualize the trend.	99
Figure A5	WAXD integrated scans of fully drawn PAN fibers spun from DMF and from sulfolane/PC (50/50) solvent mixture.	108
Figure B1	G' , G'' plots with respective to ω of (a) PAN, (b) PAN/CNT-4, (c) PAN/CNT-10, and (d) PAN/CNT-15 tested at 20 °C at the beginning and at the end of temperature sweep in order to check reversibility of temperature effects	111
Figure B2	Log-log plot of G' versus G'' for (a) diluted PAN/CNT-10 (at 4.5 g/dL of solids), and (b) PAN/CNT-10-2 dispersion at various temperatures; frequency range from 0.63 to 242 rad/s.	112
Figure C1	2-D WAXD patterns of A2 samples with various annealing times at 180°C. (a) before annealing, (b) 3 minutes, (c) 30 minutes, and d) 60 minutes of annealing.	114
Figure D1	DSC curves of PAN powder under (a) air and (b) N2 environment at 10 °C. The insets showed the areas used to calculate the $\Delta H_{reaction}$.	115
Figure D2	DSC curves at various heating rates with (a) PAN fiber in N2; (b) PAN fiber rerun in the air after runs in N2; (c) PAN/CNT-1 fiber in N2; (d) PAN/CNT-1 fiber rerun in the air after runs in N2.	116
Figure D3	Plots for the activation energy of (a) cyclization; and (b) oxidation, according to Kissinger's equation [161].	116
Figure D4	Kinetic constants versus temperature of (a) PAN, (b) PAN/CNT-1, (c) PAN/CNT-2, and (d) PAN/CNT-3 fibers.	117
Figure D5	Integrated scans of WAXD patterns of PAN and PAN/CNT fibers before stabilization.	118
Figure D6	Left: Integrated scan of WAXD patterns of (a) PAN, (b) PAN/CNT-1, (c) PAN/CNT-2, and PAN/CNT-3 after 2-hours stabilization; Right: Integrated scan of WAXD patterns of PAN fibers after (e) 3-hours, (f) 4-hours, (g) 5-hours, and (h) 6-hours stabilization at 250 °C under air environment.	118
Figure D7	Normalized O2 concentration profile calculated by Equation (D-2) of (a) PAN/CNT-2 fiber of 23 μm diameter and $3 * D_{O_2}$ after 2-hours stabilization, (b) PAN fiber of 21 μm diameter and D_{O_2} after 6-hours stabilization (c) PAN/CNT-2 fiber of 23 μm diameter and $4 * D_{O_2}$ after 2-hours stabilization. $D_{O_2} \sim 3 \times 10^{-12}$ cm ² /s at 250 °C was used for calculation for PAN fiber	121

Figure E1	Photographs of stabilized bi-component fiber tow via joule heating; (A) and (B) 6000 filaments.	122
Figure E2	WAXD integrated scan of bi-component fibers. (a) without spin finish, (b) fiber immersed into the spin finish bath for 6-hours followed by drying at 80 °C in a vacuum oven, (c) after rinsing and washing fiber (b) in water and followed by drying This figure confirms that 12 degree peak is due to spin finish (MATSUMOTO YUSHI-SEIYAKU Co., Ltd. Osaka, Japan)	124
Figure E3	DSC scan of single-component and bi-component fibers at 10 °C/min in air. The area (inlet) under the DSC curve and above the baseline between 200 and 400 °C were used to calculate the heat released from the stabilization reaction. The enthalpy of reaction is 2980 and 1194 J/g for single and bi-component fibers, respectively.	126
Figure E4	Schematic of an external macroscopic system.	127

SUMMARY

Carbon fibers are widely used in aerospace, sporting goods, and wind turbine blades for reinforcing composite materials due to their high tensile strength, modulus, and low density. However, due to the relatively high cost of production compared to some common metals such as steel or aluminum, carbon fibers have not been widely used in many other applications, such as in the automobile industry. The reduction of carbon fibers' cost is useful for a wide range of applications. Currently, polyacrylonitrile (PAN)-based carbon fiber dominates over 90% of the carbon fiber market. PAN-based carbon fibers typically are made from PAN precursor fibers after stabilization and carbonization processes. Stabilization is regarded as the rate-limiting step and requires a long residence time of about 2 hours. Stabilization generally takes place in a convective heating oven between 200 to 300 °C. In this thesis, the Joule heating process was used to replace convective heating for PAN stabilization by incorporating carbon nanotubes (CNTs) in the fiber to produce the required fiber conductivity for resistive heating. The processing, structure, properties, and Joule heating were shown for PAN/CNT fibers in this thesis. Stabilization through Joule heating was demonstrated for bi-component core-sheath PAN-PAN/CNT fibers with less than 5 wt% CNT, in both a batch and continuous process.

Chapter 1 gives an overview of the literature on the PAN fiber, and CNT based polymer composites, and Joule heating. Chapter 2 shows a rheological study of PAN/CNT dispersion with up to 15 wt% of CNT. The presence of CNTs increased the elastic-like and shear thinning behavior of the dispersions. Rheological behavior provides a good indicator of fiber spinnability of PAN/CNT. Chapter 3 presents the fabrication, mechanical and

electrical conductivities, and Joule heating of bi-component core-sheath PAN-PAN/CNT fibers in a batch process. Fibers with relatively thin sheath allowed overall CNT loading as low as 3.7 wt% to be made with good electrical conductivity, and such fibers were used to demonstrate that Joule heating was able to stabilize PAN at a relative low CNT content. Chapter 4 focuses on the stabilization of PAN/CNT fibers in a convective heating oven, including both single-component and bi-component core-sheath PAN-PAN/CNT fibers. CNT increased the reaction rate and reduced the time of PAN stabilization in these fibers. When comparing to PAN fiber with comparable diameter, the heat of stabilization of PAN/CNT fibers increased up to 3 times in the air atmosphere. Porosity was observed in the PAN/CNT precursor and in the stabilized PAN/CNT fiber. This porosity was considered responsible for increased oxygen diffusion rate, and hence for reduced PAN stabilization time. Chapter 5 presents a continuous Joule heating process, which was used for the first time to stabilize polyacrylonitrile (PAN) fibers containing carbon nanotube (CNT) fillers. Single-component PAN/CNT fibers with 7 wt% CNT and bi-component fibers with core-sheath geometry and less than 5 wt% CNT were fabricated. Joule heating was conducted continuously on a 200 filament bundle for single-component fibers and on bundles with up to 6000 filaments for the bi-component fibers. A model of heat transfer and thermodynamics occurring during Joule heating is developed and utilized to understand the reductions in stabilization time and energy consumed when compared to convective heating. The minimum energy needed for stabilization through Joule heating is estimated to be less than 1 % of the energy used through convective heating. Conclusions and recommendations for future work are presented in Chapter 6.

CHAPTER 1. INTRODUCTION

1.1 PAN and PAN fiber

PAN fibers are used to make blankets, outdoor awnings, and clothing [1]. For example, acrylic made from PAN copolymers is often used in knitted clothing such as sweaters and socks. Moreover, PAN is the current dominant precursor for carbon fiber. Figure 1.1 shows the chemical structure of the PAN polymer. PAN-based precursor is made from petroleum products: the single unit of polyacrylonitrile, acrylonitrile (AN) can be made through ammoxidation process with ammonia and propylene, then precursor PAN can be produced through the polymerization of AN [2,3].

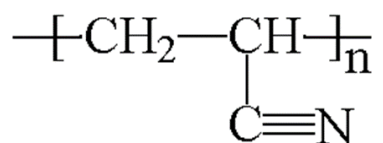


Figure 1.1. Chemical structure of monomer repeat unit of PAN.

PAN degrades before melting under normal conditions. The melting behavior was only observed at a very rapid heating rate (i.e. >50 °C/min) [4,5]. Due to the special behavior, PAN is commonly solution processed. PAN fibers were first mass produced using solution spinning by DuPont in the 1950s [3]. PAN precursor can be made by a variety of spinning techniques, including melt spinning [6,7], dry spinning (e.g., DuPont OrlonTM and Bayer DralonTM) [3], wet spinning, dry-jet-wet spinning [8]. Wet spinning and dry-jet-wet spinning are widely used in industry or for research to produce precursor fibers. In both processes, PAN polymer or its copolymer is dissolved into highly polar

solvents such as dimethyl sulfoxide (DMSO), N, N-dimethyl formamide (DMF), and N, N-dimethyl acetamide (DMAc) [3,8]. A pump or a piston pushes the PAN polymer solution into a jet through a spinneret. Then, the jet coming from the spinneret immerses into different coagulation baths. In the wet spinning process, the jet goes into a non-solvent for PAN, such as water or methanol; while in the dry-jet-wet spinning process, the jet first passes through a small air gap where evaporation takes place, followed by a non-solvent bath.

Gel spinning has also been used to produce PAN and PAN copolymer fibers. High molecular weight PAN-co-MAA has been recently used to produce precursor, composite fiber, and carbon fiber [9–12]. Firstly, the polymer solution is made with high molecular weight, low solid content PAN or PAN co-polymer in DMF or DMAc; then the jet is quenched into a cold methanol bath to form a gel-like state with fiber shape (as-spun fiber); lastly, the as-spun fiber can be further drawn into a highly oriented fiber.

Co-solvent systems have been studied for PAN [13–21]. The motivations of these studies on co-solvents can be summarized as follows: 1) to understand the rheological behavior and gelation of PAN solution in DMSO with added non-solvent such as water or ethanol; 2) to correlate the interaction between solvents (or solvent mixtures) and polymer (i.e., solubility parameters) to the gelation behavior and the homogeneity of polymer solution; 3) to understand the effect of non-solvent in the spinning solution on the coagulation process and fiber morphology (e.g., voids formation).

Co-solvent system involves PAN dissolved in solvent mixtures with water and dimethyl sulfoxide (DMSO) has been studied intensively [19–21]. Other co-solvent systems include methanol/DMSO, ethanol/DMSO, and toluene/DMAc, or a mixture of good

solvents such as DMF/DMSO [13–18]. One interesting finding for those complex systems is that non-solvents, including water and ethanol, can induce elevated gelation temperatures in PAN/DMSO solutions [19–21]. Fiber spinning has also been carried out using PAN/DMSO/water and PAN/DMSO/ethanol. Chen et al. [20] and Zhang et al. [21] believed that the non-solvent added into polymer solution for fiber spinning influenced the dual diffusion of solvent and non-solvent during the coagulation process and led to a homogenous microstructure of PAN fiber. However, in both studies, the properties and microstructure of fiber spun from PAN/DMSO/water were not compared to the fibers spun from PAN/DMSO. And the effect of non-solvent on resulting fiber properties remained unclear. To answer the question, a case study was conducted in the current work to show the effect of water on the tensile properties of the resulting PAN fiber. Besides, the gelation behavior of PAN/DMF with water and toluene co-solvent is studied.

In addition, Hansen's solubility parameters are used in the current study to guide the selection of solvent and solvent mixtures for PAN fiber spinning. A number of solvent and co-solvent systems are selected from the prediction of Hansen's solubility parameters, including DMF/water, DMF/toluene, sulfolane, and sulfolane/propylene carbonate (PC). Multiple solvent mixtures are shown to be potential alternative solvents for producing PAN fiber, including DMF/PC and Sulfolane/PC from the current study. Nevertheless, the tensile properties of PAN fibers made using such solvent mixtures did not show a significant increase when compared to the tensile properties of fibers spun from the PAN solution dissolved in DMF. The results of the work are documented in Appendix A.

1.2 Carbon nanotubes (CNT) and polymer/CNT composites

Carbon nanotubes were successfully synthesized by Iijima in 1991 [22]. Various types of carbon nanotubes have been developed, which are commonly classified by the number of walls of the tube, including single-wall carbon nanotube (SWNT) and multi-wall carbon nanotube (MWNT). Carbon nanotubes have been made through various processes such as chemical vapor deposition, laser ablation, or arc discharge [23]. Some of the most important properties, including the size (diameter, length, or aspect ratio), number of walls, or purity of carbon, depending on the manufacturing techniques.

CNTs show high mechanical properties. The theoretical calculation shows up to 150 GPa ultimate strength and up to 1 TPa modulus for a single carbon nanotube [24]. Besides exceptional mechanical properties, CNT can also have high electrical and thermal conductivity up to 10^7 S/m and 6000 W/m-K, respectively [25].

Incorporation of CNT into polymers can make conductive composites and enable various applications, including electrostatic dissipation, electrostatic painting, electromagnetic interference (EMI) shielding, printable circuit wiring, and transparent conductive coating [24]. For example, composition > 0.3 wt% SWNT loading into polycarbonate (PC) enables electrostatic painting with electrical conductivity in the range of 0.01-10 S/m [26]. One of the most important concepts is the percolation threshold involving conductive composites with CNT filler. The percolation threshold is defined as a sharp order of magnitude jump in electrical conductivity, which indicates a three-dimension network in the polymer nanocomposite [27]. Percolation network can be determined by fitting with a power-law function [26]:

$$\sigma_c \propto (\phi - \phi_c)^\beta \quad (1)$$

where σ_c is the electrical conductivity of composite, ϕ is CNT volume fraction, ϕ_c is the CNT volume fraction at the percolation threshold, and β is the critical exponent.

Many factors contribute to the percolation threshold, including the CNT length, aspect ratio, dispersion, and alignment. Bai and Allaoui [28] found that by increasing MWNT length from 1 to 50 μm , the threshold decreases 8 times with MWNT/epoxy composites. Through both experiments and 2D Monte Carlo simulation, Du et al. [29] confirmed that intermediate alignment contributed to higher conductivity than fully isotropic condition at small SWNT loading. When CNTs align themselves, then fewer contacts appear between tubes, and the conductivity decreases [29]. Dispersion and aggregates lead to a controversial argument involving percolation: Generally, better dispersion leads to a lower threshold since well-dispersed CNT has a higher aspect ratio than aggregate. However, Kovacs et al. [30] showed that high contact resistance would arise when the CNT were well-dispersed and wrapped by polymer structure. Bryning et al. [31] also found that slight aggregation could result in a lower percolation threshold with solvent processing of SWNT into epoxy.

1.3 Bi-component fiber

Bi-component fibers were first found in nature. In the 1950s, by employing differential staining experiments, natural wool fibers were found with an inherent bilateral structure, which was believed to be related to the fiber's self-crimping effect [32]. A synthetic side-by-side bi-component fiber named CantreseTM, made from two different nylon polymers, was introduced commercially by DuPont in the 1960s [33]. The idea to make fiber with two components has become one of the important concepts in fiber research and industry. Bi-component fibers with various cross-section geometries have

been made, including sheath-core, island-in-the-sea, and side-by-side [34,35]. With bi-component geometry, certain properties can be achieved with two polymer components of different properties. Multi-functionality can also be achieved by the introduction of extra fillers using bi-component geometry [36,37]. Mechanical, electrical, thermal, or aesthetic properties can be enhanced. Filler such as nano metallic particles, cellulose nanocrystals, or CNTs can be incorporated for imparting different properties in the fibers [38]. CNTs have been used in the bi-component fibers for enhancing electrical properties (Table 1.1) [34,39–45]. One example is the core-sheath polyethylene/CNT (10 wt%) – polyamide fiber fabricated by Strååt et al. [42]. By using the core-sheath structure, the electrical conductivity was improved at relatively low overall CNT content by only putting CNT in the sheath component. The bi-component fibers possessed electrical conductivity of up to 10 S/m at 3 wt% CNT. The maximum electrical conductivity of such bi-component fiber is higher than most of the reported experimental data from the literature (<10 S/m) of polymer/CNT at CNT content <3 wt% summarized by Bauhofer and Kovacs [46].

Another study [34] on PAN core and PAN-CNT sheath fibers processed gel spinning showed good mechanical properties (400 MPa tensile strength and 15 GPa modulus) but relatively low electrical conductivity (10^{-4} S/m), or good electrical conductivity (0.366 S/m) with relatively low tensile properties (183 MPa tensile strength and 9.6 GPa tensile modulus). The overall CNT wt% in these fibers was as high as 7.4 wt% calculated based on various parameters reported in that study [34]. The current study is motivated to further reduce the overall CNT concentration and to make PAN/CNT composite fibers that exhibit both good mechanical properties and electrical conductivity.

Table 1.1. Summary of properties of core-sheath fibers incorporating with CNT.

Core	Sheath	Overall wt. % CNT	Spinning method	Draw ratio	Fiber diameter ⁺	Tensile strength (MPa)	Tensile modulus	Electrical conductivity (S/m)	Ref
Poly(ethylene oxide) (PEO)	PEO/CNT (3 wt%)	0.05 - 0.5	Electro-spinning	-	200 - 300 nm	3 - 8	50 - 200 MPa	10^{-13} - 10^{-2}	[40]
CNT	Cellulose	20 - 45		-	$\sim 7 \mu\text{m}$	2 - 5	-	10^{-1} - 10	[41]
CNT	Poly(methyl methacrylate)	-		-	1.4 - 2.8 μm	-	-	1 - 100	[43]
Polyethylene/CNT (10 wt%)	Polyamide	3	Melt spinning	65 - 195	$\sim 40 - 60 \mu\text{m}+$	$\sim 200 - 500$	-	10^{-1} - 10	[42]
PP/CNT (20 wt%)	Poly(vinylidene fluoride)	10		1 - 4.1	50 - 100+ μm	-	-	1 - 10	[44]
PAN	PAN/CNT (10 wt%)	5.7 - 7.4	Gel spinning	1.6; 11	44.1; 18.6 μm	155; 419	9.2; 16.1 GPa	$0.366; 10^{-4}$	[34]
PAN/CNT (10wt%)	PAN	0.6 - 1.5		2-22	14 - 25 μm	100 -800	5 - 20 GPa	-	[34]
Silicon elastomer/CNT(1 - 3.5 wt%)	Silicon elastomer	-	Wet spinning	-	0.3 - 1.2 mm	-	~ 0.49 MPa	$10^{-7} - 5$	[45]

+The fiber diameters were estimated with the reported linear density and density of polymer composites.

1.4 Rheological behavior of polymer nanocomposites

Rheology, defined as the science of deformation and flow, is widely used to study the behavior of polymeric liquids [47]. Over the past decades, rheology has also been widely used to study polymer nanocomposites. Among all the nanocomposites, polymer/CNT composites have attracted a lot of attention, and numerous studies have been performed to explore the effect of CNT on polymer rheology. The effect of CNT on the rheological behavior of polymer/CNT composites can be complicated, depending on the polymer matrix, content, properties, and treatment of CNT, the processing step, and dispersion conditions of CNT into the matrix.

CNT can affect shear-thinning behavior, especially at high CNT loading [48–51]. For example, CNT addition into polycarbonate with up to 1 wt% did not change the complex viscosity (η^*) dependence on frequency significantly. However, at carbon nanotube concentrations of 2 wt% and above, the Newtonian plateau at low frequency disappeared, and a complete steep power-law shear thinning was observed in the measured frequency range. The change in shear-thinning behavior can be due to the network formed with CNT, which restrain the motion of the polymer chain at low frequency. The concentration at the change of shear-thinning behavior (i.e., the step increase of complex viscosity at low frequency) are often called rheological percolation threshold [48].

The change in η^* or shear-thinning can be mostly due to the change in elastic component (G') with CNT. The CNT can form an entangled network, restrain the mobility of the polymer chain, and increase the elastic-like behavior. CNT was shown to reduce the terminal slope ($\omega \rightarrow 0$) of the G' versus ω [48,51]. At low frequencies, a scaling relationship of $G' \sim \omega^2$ and $G'' \sim \omega$ indicates a typical homopolymer with no polydispersity.

However, at elevated CNT loading, G' can become weakly dependent on the ω and become almost independent of frequency at high CNT loading [51].

Table 1.2 summarizes the rheological behavior of CNT and multiple other nanofillers in multiple polymer matrices. Besides CNT filler, other fillers including cellulose nanocrystal (CNC) [52–54], carbon black (CB) [55–57], graphene oxide [58,59], and nano clays [60] are also shown to change the rheological behavior of the polymer. Cellulose nanocrystals (CNC) are another promising rod-like nanofiller for reinforcing polymers, and PAN/CNC dispersions have been studied previously [52,53]. The rod-shaped CNC has a diameter of 3–20 nm and a length of 50–500 nm [61]. CNC also increase η^* and change the shear-thinning of PAN/CNC suspension. At 30 wt% CNC content, η^* no longer showed a Newtonian plateau but a steep shear thinning at all measured frequencies [54]. CB, on the other hand, is an isotropic filler compared to the rod-like CNT or CNC filler. CB increased the η^* of polymer matrix at a much higher concentration than CNT in the same polymer matrix at comparable processing conditions [55].

Table 1.2. Rheological behavior of multiple polymer nanocomposites.

Type of Filler	Filler wt%	Type of Polymer matrix	Processing method	Rheological behavior highlights	Ref
CNT	0.5 -15	PC	Melt mixing	η^* show disappearance of plateau and step increase at low frequencies at 2 wt% CNT; G' shows weaker dependence on ω at elevated CNT content	[48]
CNT	1-10	LDPE	Melt mixing	η^* show disappearance of Newtonian plateau regime and step increase at low frequencies at 3 wt% CNT; Cox-Merz rule is no longer valid.	[61]
CNT	0.1-10	HDPE	Solvent mixing	η^* show a decrease at 0.2 wt% since the PE chain absorbed on the CNT surface and the entanglement density in bulk decreased.	[62]
CNT	0.1 -5	PP	Melt mixing and ball milling	η^* shows the disappearance of Newtonian plateau regime and step increase at low frequencies at 3 wt% CNT.	[63]
CNT	1- 15	PAN	Solvent mixing, SWNT non-covalently wrapped with PMMA	η^* show step increase at low frequencies at 15 wt%; Suspension with worse CNT dispersion showed lower η^* than those of suspension with better dispersion at 5 wt%.	[64]

Table 1.2. Continued

CNC	5-40	PAN	Solvent mixing	η^* show disappearance of the plateau and step increase at low frequencies (<10 rad/s) at 30 wt%.	[54]
CB	5-30	PS	Dry blended (powder)	Carbon black increases the shear viscosity (η) significantly.	[56]
CB & CNT	1-6 (CB); 0.2-0.6 (CNT)	Epoxy (before UV cure)	Ultrasonication	Both CB and CNT increase η ; η^* and G' of the suspension with 4 wt% CB are similar to those of suspension with 0.4 wt% CNT at all frequencies.	[55]
CB	8	PP/PA6	Melt mixing	G' increased one order of magnitude at low frequencies than G' of pure matrix	[57]
Graphene oxide	0.048-2.33 (vol%)	ABS	Solvent mixing	Graphene oxide increases the η^* and G' .	[58]
Graphene oxide	0.3-6	HDPE	Solvent mixing	G' increased with graphene oxide wt% at low frequencies	[59]
Nano clay (organoclay)	2-8	HIPS	Dry blended	G' and η^* of polymer nano clay are higher than pure polymer when frequency <1 rad/s but as compared with those of pure polymer above 1 rad/s.	[60]

HDPE – high density polyethylene; LDPE – low density polyethylene; PP- Polypropylene; PA- polyamide; PS – polystyrene; ABS - Acrylonitrile-butadiene-styrene; HIPS – high impact polystyrene

1.5 Stabilization of PAN

The stabilization process is one important step to manufacture polyacrylonitrile (PAN)-based carbon fiber. This process is highly energy-intensive and time-consuming and is generally regarded as the rate-limiting step for making PAN-based carbon fiber. During stabilization, PAN fibers undergo simultaneous reactions, including cyclization, oxidation, cross-linking, and dehydrogenation [65–68]. Moreover, cyclization does not need oxygen, while oxidation requires oxygen or other oxidizing agents [68]. The stabilization thermally converts PAN into a ladder structure and increases the thermal stability of PAN for carbonization.

Acid groups have been typically incorporated into the PAN molecules to lower the stabilization reaction initiation temperature, broaden the exotherm, and moderate the released heat [69]. Cyclization reaction, one of the main reactions in the stabilization process, is initiated by free radicals for homo-PAN molecules. For PAN copolymer with the acid group, ions from the acid group can reduce the activation energy and accelerate the initiation of cyclization reaction [10,70]. Besides acid group, lignin [71], cellulose nanocrystal (CNC) [72], potassium permanganate [73], and dibutyltin dimethoxide [74], Co and Ce cations [75] have been shown to reduce the activation of cyclization and accelerate the stabilization.

The oxygen mass transfer and heat transfer play important roles during stabilization. The oxidation during stabilization requires a long residence time due to the oxygen diffusion limitation. The oxygen diffusion limitation generally results from the low O_2 diffusivity (D_{O_2}) within PAN fibers during stabilization. Warner et al.[76] estimated the D_{O_2} to be about $2 \times 10^{-12} \text{ cm}^2\text{s}^{-1}$ at 220 °C for commercial acrylic fibers. In the same

work, the author showed that oxidized skin layer on fiber surface limited the flux of oxygen into the fiber. The skin layer was estimated about 1 μm and was in reasonable agreement with the observed oxidized skin layer after etching with aqueous sulfuric acid ($\sim 0.4 \mu\text{m}$) [76]. One of the developments is from UT-Battelle, where plasma is used for stabilization in place of convective heating [69,77,78]. Plasma is thought to enhance oxygen diffusion [69]. In addition, polymeric materials generally have low thermal conductivity, in the range of 0.1 – 0.5 W/m-K [79,80]. The low thermal conductivity makes it difficult to transfer heat from within the fiber to the environment when exothermic reactions take place [81].

1.6 Joule heating applications

Joule heating was established by James P. Joule in the 1940s: heat can be generated by the passing electric current through an electrical resistor [82]. Joule heating of film, fiber, and textile has been used in warming the human body and in wearable electronics [83]. To increase the electrical conductivity, conductive fillers are commonly introduced into a polymer matrix to enable Joule heating, including silver nanowire [84,85], copper nanowire [86], liquid metal-based on gallium and indium [87], CNT [88,89], and reduced graphene oxide[90]. For example, silver nanowires [84], liquid metal [87] have been incorporated into polydimethylsiloxane (PDMS) film to make stretchable heaters for wearable electronics applications.

Joule heating can also be used for de-icing coatings [91,92], self-repair and self-post-curing of thermoset materials [93,94], and healing the defects in graphene oxide and induced sp^2 restoration at 2000 $^\circ\text{C}$ [95]. Joule heating has also been applied to PAN/CNT fibers [96]. PAN/CNT composites fibers with high filler loading (15- 20 wt%) show exhibit sufficient electrical conductivity for effective Joule heating. Applied current generates heat

and thermally converts precursor PAN/CNT fiber into the stabilized fiber. The traditional stabilization process requires heating at 200-300°C. This process can be potentially energy efficient as the current stabilization process is carried out in high temperature ovens. In addition, these composite fibers can be used for other heating purposes, such as electrically heated fabric. However, the previous literature study only demonstrated joule heating at 15 -20 wt% CNT into fibers [96]. The high CNT content increases the cost of the final fiber. To reduce cost, alternative approach is needed, preferably to reduce CNT content, while successfully achieving Joule heating.

1.7 Thesis objectives

The broad objectives of this thesis are to study the processing, structure, and properties of PAN/CNT composite fibers. and to achieve Joule heating-based stabilization with those fibers at reduced CNT loading. The following studies are carried out to achieve the objectives:

- In Chapter 2, the rheological behaviors of PAN/CNT dispersions are measured and used to guide the fiber spinning of PAN/CNT.
- In Chapter 3, PAN-PAN/CNT core-sheath bi-component fibers are fabricated at a CNT content below 5 wt%, the mechanical and electrical properties are investigated, and the Joule heating is validated in a batch process with those fibers.
- In Chapter 4, the effect of CNT on the stabilization of PAN/CNT fibers is studied in a convective heating oven.
- In Chapter 5, Joule heating is demonstrated as a method to stabilize PAN/CNT fibers in a continuous manner, and the process is analyzed.

CHAPTER 2. RHEOLOGICAL BEHAVIOR AND FIBER SPINNING OF POLYACRYLONITRILE (PAN)/CARBON NANOTUBE (CNT) DISPERSIONS AT HIGH CNT LOADING

2.1 Introduction

Spinnability of the PAN solution is critical for continuous fiber manufacturing [97]. A number of studies have been conducted on fiber spinnability. For example, Ziabicki and Krozer [98,99] investigated the solvent viscosity, surface tension, relaxation time, and resilience of liquid on jet-breakage during fiber spinning. Han [100] proposed to use the critical tensile stress of a given solution to characterize spinnability. Ide and White [101] discussed three failure mechanisms, including capillary and ductile failure, and fracture of low and high molecular weight polymers for describing spinnability. Wang et al. showed the importance of pressure drop through the spinneret as one criterion for spinnability assessment using dynamic simulation study [102]. However, none of those studies can address the complex system of PAN solutions during fiber spinning. Practically, rheological measurements of spinning solutions (also called dopes) are often applied to guide polymer fiber spinning. For example, complex viscosity was measured and monitored by Liu et al. [103] for guiding wet spinning of PAN. Morris et al. [104] identified the desired shear viscosity range from previously measured data of spinnable solutions and used that information to make solutions of newly synthesized PAN polymer for successful gel spinning.

CNT addition increases the complexity of the polymer solution and changes the flow behavior of the dispersion significantly [105]. Moreover, depending on the CNT

characteristics (e.g., length, aspect ratio, number of walls), polymer type, polymer molecular weight, nature of the solvent, the range of suitable processing conditions can vary. Identification of appropriate conditions for continuous processing such as fiber spinning can be challenging and may require extensive trial-and-error experimentation. This work is an attempt to provide guidance to the fiber spinning of nanocomposites based on their rheological behavior.

In the current study, we analyze rheological data to guide fiber spinning of PAN/CNT dispersions at relatively high CNT loadings. After establishing the fiber spinning window for PAN/CNT dispersions, we also assess the generality of the proposed behavior. Cellulose nanocrystals (CNC) are another promising rod-like nanofiller for reinforcing polymers, and PAN/CNC dispersions have been studied previously [52,53]. Rheological behavior and fiber spinning results of PAN/CNC dispersions containing 20 to 60 wt% of CNC with respect to total solids show similarities to PAN/CNT studies reported in this study.

2.2 Experimental procedures

2.2.1 Materials

Polyacrylonitrile-co-methacrylic acid (PAN) with three different viscosity average molecular weights (M_v) of 247,000; 500,000; and 964,000 g/mol, containing 4 wt% methacrylic acid copolymer were obtained from Japan Exlan Co., Japan. The polymers were vacuum dried at 75 °C overnight prior to making solutions. Multi-wall carbon nanotubes, SMW200, were purchased from SouthWest NanoTechnologies, Inc. (SWeNT), Oklahoma. The CNT length was reported to be in the 3 to 6 μm range, and the average

number of walls was 9 to 10, and the average diameter was 12 ± 3 nm. The average number of walls was determined by X-ray diffraction, and the average diameter was determined by SEM [106]. Cellulose nanocrystal (CNC) was purchased from the Process Development Center at the University of Maine (freeze-dried powder, lot# 2012-FPL-CNC-48/051). Dimethylformamide (DMF) was obtained from Sigma-Aldrich. Methanol (ACS grade) was purchased from VWR Chemicals.

2.2.2 Solution and dispersion preparation

For PAN solution, PAN powder was dissolved into dimethylformamide (DMF) at 75 °C. For PAN/CNT dispersion, CNT powder was first homogenized in DMF at a concentration of 35 mg per 300 ml using a homogenizer (T25 ULTRA-TURRAX, IKA) at 10,000 rpm for 30 minutes. The slurry was then bath sonicated for 48 hours (Bransonic, 3510-MT, 8510). CNT/DMF dispersion was added into the reactor containing PAN solution at the desired PAN solid content while stirring at 70 °C. Excess DMF was evaporated using a vacuum distillation process at 70 to 80 °C. Control PAN solutions and PAN/CNT dispersions with 4, 10, 15 wt% CNT with respect to the total solids loading are labeled as PAN, PAN/CNT-4, PAN/CNT-10, and PAN/CNT-15, respectively. All of these samples were made using a PAN powder blend of 75% with M_v of 500,000 g/mol and 25% with M_v of 964,000 g/mol. Another PAN/CNT dispersion with 10 wt% CNT and 90 wt% PAN of M_v of 247,000 g/mol is labeled as PAN/CNT-10-2. PAN/CNC dispersion with 60 wt% CNC and 40 wt% PAN as solids was prepared following the previously reported protocol [53]. All solution and dispersion preparations are summarized in Table B1.

2.2.3 Solution and dispersion characterization

Control PAN solution and PAN/CNT dispersions were characterized by a rheometer (Anton Paar MCR-302) using cone-and-plate geometry, with a 50-mm truncated cone on top, and a 50-mm bottom plate with Peltier temperature control. The cone angle was 1.0° , and the minimum gap size at the center of the truncated cone was $53\ \mu\text{m}$. An evaporation blocker was used to prevent solvent evaporation and to reduce air disturbance during measurements [107]. The linear viscoelastic regime was determined initially by performing a dynamic strain sweep (0.01 – 10 %). 1 % strain, which was in the linear viscoelastic regime for all solution and dispersions, was chosen for dynamic frequency sweeps that were performed from 0.63 to 242 rad/s. To study the effect of temperature on the rheological behavior of the solution and dispersions, the frequency sweep was first conducted at $20\ ^\circ\text{C}$, then at lower temperatures (10 and $0\ ^\circ\text{C}$), and finally in the elevated temperature range (30, 40, 50, $60\ ^\circ\text{C}$). Before each test, the solution or dispersion was kept for at least 3 minutes at the desired temperature to ensure thermal equilibrium and to eliminate thermal history effects. At the end of each sequence, the thermal stability of the sample was tested again at $20\ ^\circ\text{C}$. It was found that the storage modulus G' and loss modulus G'' did not change after tests at higher and lower temperatures (Figure B1). Flow curves were determined by performing three steady shear intervals at shear rates from 0.01 to $100\ \text{s}^{-1}$, 100 to $0.01\ \text{s}^{-1}$, and 0.01 to $100\ \text{s}^{-1}$, respectively, and the average shear viscosity for these three subsequent segments was reported at each shear rate. This protocol for measuring flow curves provides an inherent check for thixotropy, which was not found to be a significant factor in the various solution and dispersions studied and reported here. Rheological properties of the PAN/CNC-60 dispersion were also measured following the previous study by Chang et al. [53].

2.2.4 Fiber spinning

PAN/CNT fibers were spun using a single-filament fiber spinning unit (Hills Inc. FL). The spin pack is equipped with a single hole spinneret with either a 200 or 500 μm diameter capillary. The extrudate passed through a 50 mm air gap followed by immersion in a methanol bath during gel spinning. Figure 2.1 shows the schematic of the gel spinning set up. For fiber spinning, the PAN/CNT dispersions undergo jetting, coagulation in methanol, and fiber collection at the take-up roller.

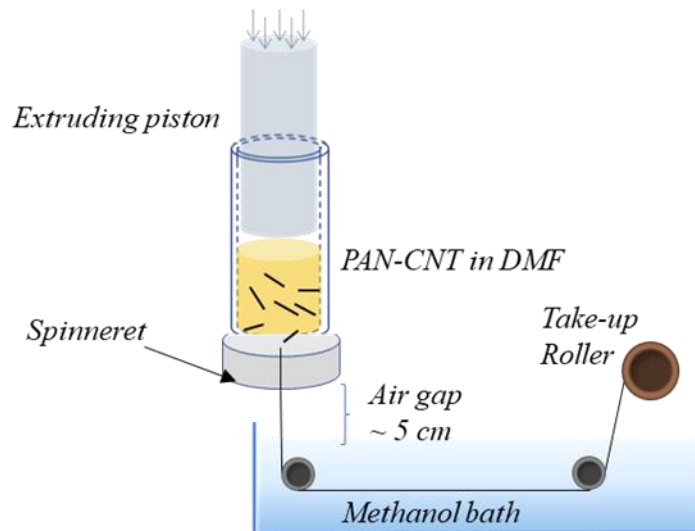


Figure 2.1. The scheme of the fiber gel spinning apparatus.

2.3 Results and discussion

Figure 2.2 shows the shear (η) and complex viscosity (η^*) of the pure PAN solution and PAN/CNT dispersions. For PAN and PAN/CNT-4, both shear-viscosity and complex viscosity showed a transition from viscosity plateau at a low shear rate or low frequency region to a shear-thinning region at a high shear rate or frequency. In contrast, 10 and 15 wt% CNT samples showed shear thinning behavior across the entire shear rate range. The

transition of shear or complex viscosity to a single shear-thinning behavior has been observed before for polymer/CNT systems, and the CNT concentration at which the transition occurs is typically reported as the rheological percolation for the CNT network in the polymer matrix [108–111]. Also, all the solutions and dispersions showed good overlap between shear and complex viscosity except for PAN/CNT-15. The overlap between steady state shear viscosity (η) and complex viscosity is often described by an empirical relationship, the Cox-Merz rule, which was validated to be applicable for PAN solutions previously [112]. The Cox-Merz rule holds at low CNT loading but failed at high CNT loading of 15 wt%. This suggests that the interconnected CNT network influenced the shear-thinning behavior significantly for PAN/CNT blends.

Moreover, the PAN/CNT-15 dispersion showed a lower absolute value of η in compared with η^* at comparable values of $\dot{\gamma}$ and ω , and a weaker power-law scaling factor of η with $\dot{\gamma}$ ($\eta \sim \dot{\gamma}^{-0.67}$) in compared with η^* with ω ($\eta^* \sim \omega^{-0.75}$). These trends were also consistent with the results reported for PEO/CNT melts when the CNT concentration is above 3 times the rheological percolation threshold [113].

Figure 2.2 (a) shows the storage modulus (G') versus loss modulus (G'') behavior. The terminal slope (when $\omega \rightarrow 0$) of $\log G'$ versus $\log G''$ curve, also known as Han's plot or modified Cole-Cole plot, can be used quantitatively to illustrate the solution homogeneity [108]. The slope decreased with increasing CNT concentration from 1.38 for the PAN solution without CNT to 0.46 for the PAN/CNT-15 dispersion (Table B2), which suggests the interconnected network significantly reduced the solution homogeneity. In addition, the $\log G'$ versus $\log G''$ curve went across and above the line denoting $G' = G''$

with increasing amounts of CNT, which indicates a transition from a liquid-like state to a solid-like gel state. The control PAN solution and PAN/CNT-4 sample showed cross-over of curves of $\log G'$ versus $\log G''$ with the $G' = G''$ line. For PAN/CNT-10 dispersion, the curve of $\log G'$ versus $\log G''$ was entirely above the $G' = G''$ line. At 15 wt% CNT, the curve of $\log G'$ versus $\log G''$ lay far above the $G' = G''$ line at all frequencies in comparison to the PAN/CNT-10 dispersion.

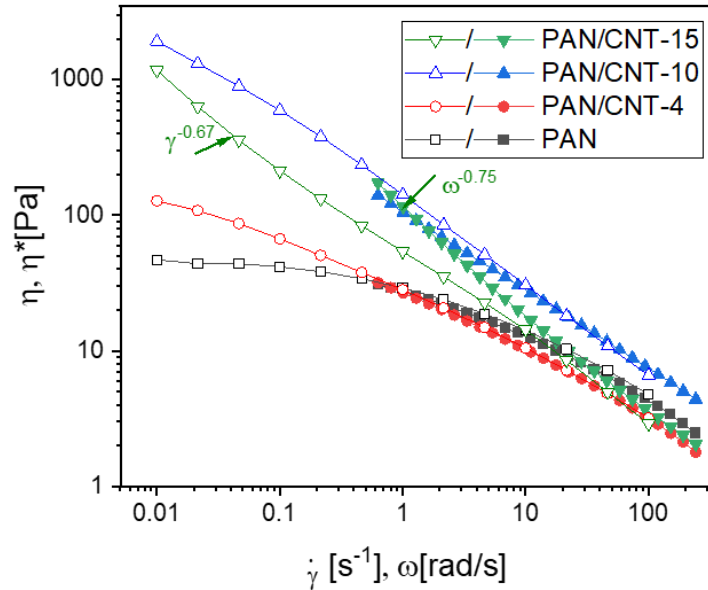


Figure 2.2. Shear viscosity (η , open symbols), and complex viscosity (η^* , solid symbols) of PAN/DMF and PAN/CNT/DMF samples at ~ 7 g/dL solid content, as measured at 20 °C.

The $\tan \delta$ (G''/G') as a function of frequencies shown in Figure 2.3 (b). With increasing amounts of CNT, the value of $\tan \delta$ decreased, which is consistent with the transition from liquid-like to solid-like behavior. When CNT content is higher than 10 wt%, $\tan \delta$ remained < 1 across the entire frequency range probed in these measurements. And instead of decreasing $\tan \delta$ values with elevated frequency, which was observed for control

PAN and PAN/CNT-4, $\tan \delta$ for PAN/CNT-10 showed an increase in the low frequency range (0.63 – 20 rad/s), and a modest decrease at higher frequencies. For PAN/CNT-15, $\tan \delta$ constantly increased with increasing frequency. CNTs made the PAN/CNT dispersion more elastic and changed the $\tan \delta$ – frequency response significantly.

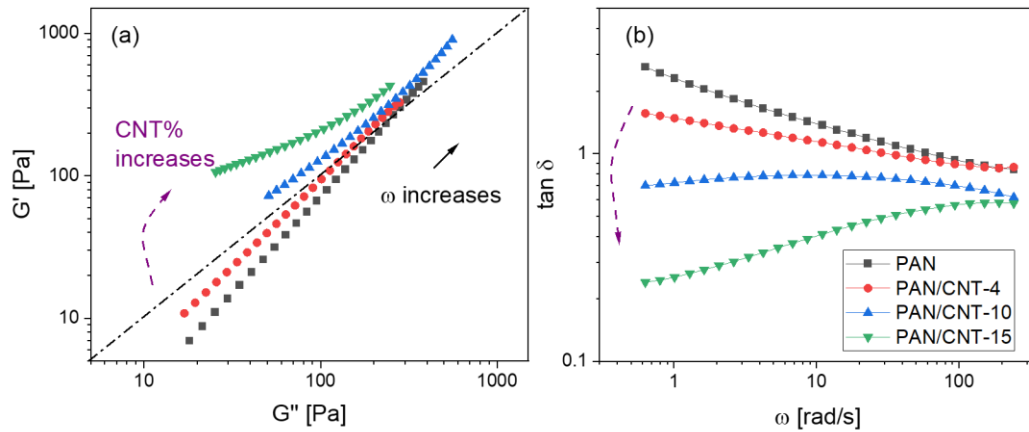


Figure 2.3. (a) Log-log plot of G' versus G'' , and (b) loss factor ($\tan \delta$) as a function of frequency ω for PAN/DMF and PAN/CNT/DMF systems at ~ 7 g/dL solid content, as measured at 20 °C.

During the fiber spinning, the solution or dispersion is extruded from the high temperature (60 to 100°C) into room temperature air gap, and then into the coagulation bath, which may be at -50 °C. Thus, understanding of temperature effect on the rheological behavior is also useful. In the current study, temperatures ranging from 0 to 60 °C were chosen.

Figure 2.4 shows the master curves of $\log G'$ versus $\log G''$ at different temperatures. All PAN and PAN/CNT samples show comparable terminal slopes for $\log G'$ versus $\log G''$ curves between 0 and 60 °C, and these slope values are: 1.39 (± 0.02), 1.2 (± 0.02), 0.88 (± 0.05), 0.46 (± 0.02) for PAN, PAN/CNT-4, PAN/CNT-10, and PAN/CNT-

15, respectively (Table B2). This indicates that the structure of the PAN solution and PAN/CNT dispersions did not change fundamentally with temperature, but it did change with a change in CNT content. It has been shown that the $\log G'$ versus $\log G''$ at different temperatures exhibit the same terminal slope when the microstructure of the polymer composites does not change with temperature [114,115]. The comparable slopes at different temperatures for all these four samples suggest that the microstructure of the polymer network, or the polymer-CNT network, did not change with the temperature between 0 and 60 °C.

Besides the master curves of the $\log G'$ versus $\log G''$, $\tan \delta$ curves at different temperatures can be used to illustrate the change in viscoelastic behavior with temperature. The change in $\tan \delta$ with temperature is plotted in Figure 2.5 at low frequency (1 rad/s) and at relatively high frequency (93.5 rad/s). At low frequency, PAN showed a decrease in $\tan \delta$ from 3.5 to 2 with decreasing temperature. Incorporation of CNT filler reduced the $\tan \delta$ significantly at low frequency. Also, $\tan \delta$ of all the PAN/CNT-10 and PAN/CNT-15 dispersions remained almost constant between 0 and 60 °C. The elastic behavior of the network formed by CNT showed no sensitivity to temperature change for the PAN/CNT-10 and PAN/CNT-15 samples at low frequency. At high frequency (93.5 rad/s), $\tan \delta$ of PAN, PAN/CNT-4, and PAN/CNT-10 decreased with decreasing temperature. On the other hand, $\tan \delta$ of PAN/CNT-15 remained the same (~ 0.5) and was not sensitive to temperature change. Overall, the $\tan \delta$ of the PAN/CNT dispersion became less sensitive than the PAN solution to temperature change.

The shear viscosity of PAN and PAN/CNT-4 are about 50 and 150 Pa s, respectively when $\dot{\gamma} \rightarrow 0$, which are within the typical range of viscosity used for successful

gel spinning [105,112,116]. PAN/CNT-10 and PAN/CNT-15 dispersions were used to conduct gel spinning in this work. PAN/CNT fiber at 10 wt% was spun at 90 °C through a 200 μm capillarity into an air gap following by a methanol coagulation bath at -50°C. However, the jetting time is relatively short (6 ± 2 minutes, Table B3), and the jet broke around the spinneret in the air gap before immersing in a methanol bath. One hypothesis was that the elastic behavior restricted the continuous flow of PAN/CNT dispersion. This is supported by the $\log G'$ versus $\log G''$ the curve shown in Figure 2.4 (c).

For PAN/CNT-15, continuous jetting was not successfully achieved when varying spinning temperature (40 -115 °C) and flow rate (0.25 -1.5 ml/min). These results can be understood in light of the rheological measurements that showed that the viscoelastic behavior of PAN/CNT-15 is only weakly sensitive to temperature and frequency changes (Figure 2.4 (d) and Figure 2.5). Single-component fibers at this high concentration were achieved only when reducing the shear rate by using a 500 μm capillary at a low flow rate of about 0.5 mL/min. In the current study, PAN/CNT-15 could not be gel spun continuously with a small diameter capillary at sufficiently high shear rates to allow for competitive production rates.

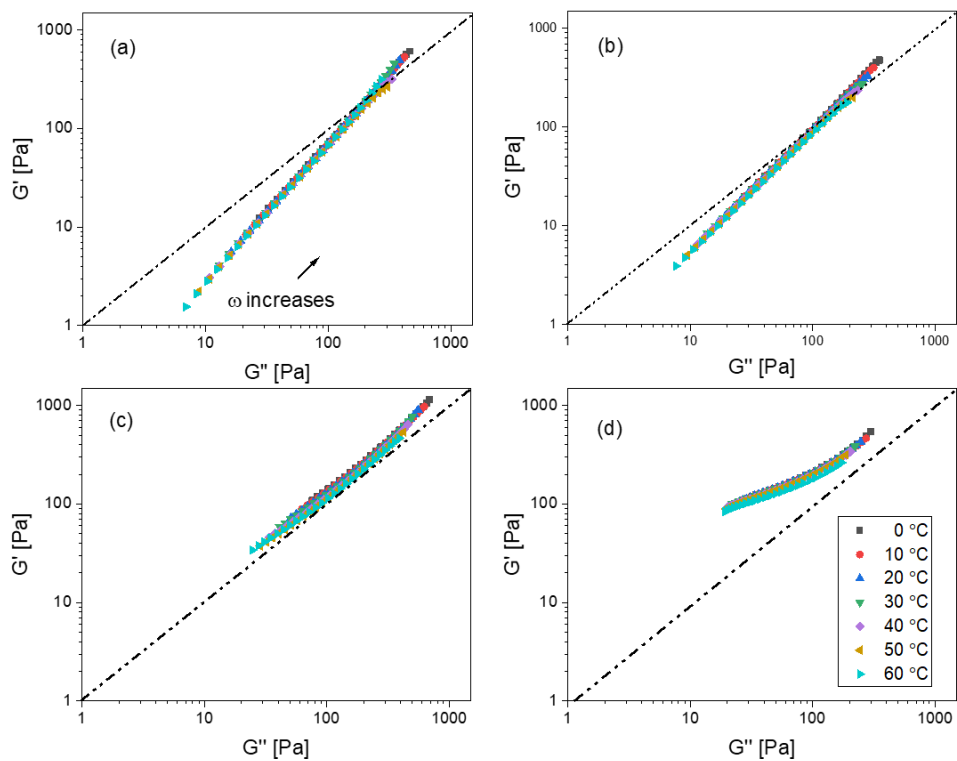


Figure 2.4. Log-log plot of G' versus G'' of (a) PAN, (b) PAN/CNT-4, (c) PAN/CNT-10, and (d) PAN/CNT-15 at various temperatures in the frequency range 0.63 – 242 rad/s.

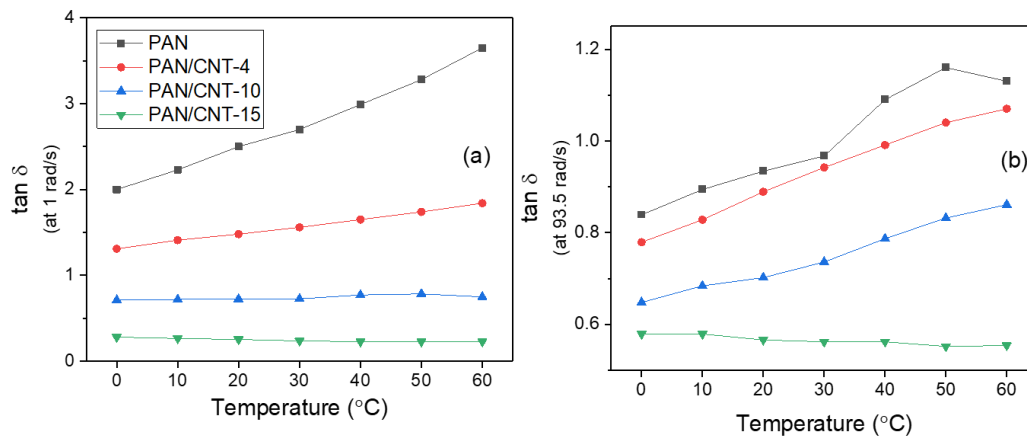


Figure 2.5. Temperature response of $\tan \delta$ for PAN, PAN/CNT-4, PAN/CNT-10, and PAN/CNT-15 from dynamic frequency measurements at oscillatory frequencies of (a) 1 rad/s, and (b) 93.5 rad/s.

Continuous fiber spinning without breakage was not achieved for either PAN/CNT-10 or PAN/CNT-15. In this study, we tried to modify the PAN/CNT-10 dispersion to achieve continuous fiber spinning; in particular, an attempt was made to reduce the elastic behavior of this dispersion. At first, the PAN/CNT-10 was diluted from about 7 g/dL to 4.5 g/dL total solid concentration. This reduced the G' and G'' by one order of magnitude (Figure 2.6 (a)) in compared with PAN/CNT-10 at comparable frequency. Moreover, at low frequencies (< 5 rad/s), the $\log G'$ versus $\log G''$ curve remained above the $G' = G''$ line, but at higher frequencies, it falls below, as is also highlighted in Figure 2.6 (b), which shows that $\tan \delta$ (G'/G'') of the dilute dispersion is above 1 when $\omega > 5$ rad/s; these data show that the dispersion is predominantly viscous-like at these frequencies. Lowering the solid content reduces polymer-polymer, polymer-CNT, and CNT-CNT entanglements in the dispersion. Fibers could not successfully be pulled from the dilute dispersion, and jetting was not successful due to the low entanglements. This experiment shows the challenges in optimizing a spinning dope: reducing the solid content, on the one hand, alleviates the elastic-like behavior at low frequencies that hinders spinning, but at the cost of entanglements that provide needed high frequency elasticity.

In order to avoid the potential issues of the reduced number of entanglements when decreasing solid content, we also made a dispersion (PAN/CNT-10-2) with PAN polymer of lower molecular weight (M_v of 247,000 g/mole) but at higher solid content (11.5 g/dL) versus the 7 g/dL used for PAN/CNT-10 with a PAN molecular weight of 500,000 g/mole. Both PAN/CNT-10 and PAN/CNT-10-2 showed comparable modulus (G' , G'') at comparable frequency. Figure 2.6 (a) shows that the $\log G'$ versus $\log G''$ curve of PAN/CNT-10-2 with low M_v is closer to the $G' = G''$ line, as compared to that of the

PAN/CNT-10 sample with higher molecular weight PAN. The overlap between curves of $\log G'$ versus $\log G''$ and $G' = G''$ was also observed for PAN/CNT-10-2 at elevated temperatures (Figure B2). Moreover, Figure 6 (b) shows higher $\tan \delta$ values of PAN/CNT-10-2 compared to PAN/CNT-10 at all testing frequencies above 2 rad/s. This suggests that PAN/CNT-10-2 is less elastic than PAN/CNT-10.

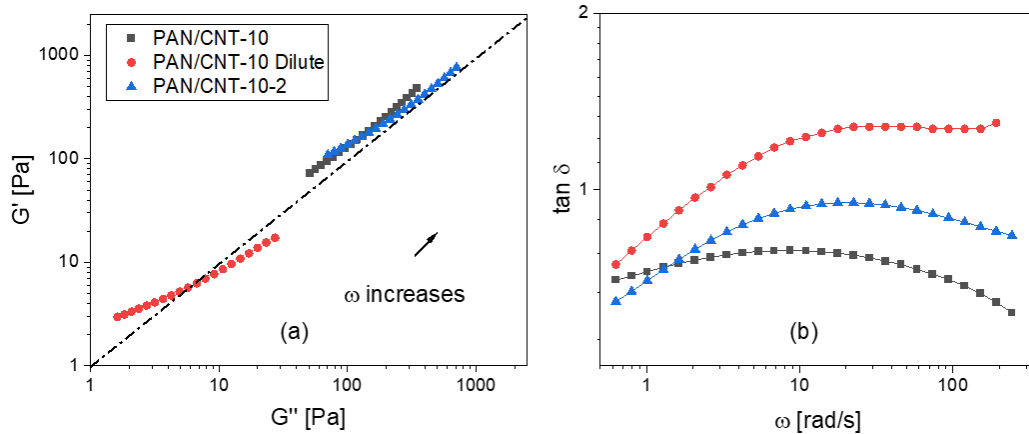


Figure 2.6. (a) Log-log plot of G' versus G'' , and (b) $\tan \delta$ as a function of ω for PAN/CNT dispersions at 7 g/dL (PAN/CNT-10), 4.5 g/dL (PAN/CNT-10 Dilute), and 11.5 g/dL (PAN/CNT-10-2); data measured for all samples at 20°C across the frequency range 0.63 – 242 rad/s

The PAN/CNT-10-2 dispersion was used to conduct fiber spinning. During fiber spinning, jetting was successfully maintained for up to 24 minutes at the same spinning temperature, spinneret, air gap, and comparable flow rate as used for spinning PAN/CNT-10 (7 g/dL) dispersion with higher molecular weight PAN, for which continuous jetting lasted no more than 7 minutes (Table B3). The longer time jetting time suggests that reduction of the overall spinning dope elasticity by using lower molecular weight PAN was beneficial.

Figure 2.7 summarizes the $\log G'$ versus $\log G''$ plots for the pure PAN solution and PAN/CNT dispersions in this study. For the pure PAN solution or PAN/CNT with low CNT concentration (e.g., PAN/CNT-4), $\log G'$ versus $\log G''$ is a straight line that crosses the $G' = G''$ line at the elevated frequency (Figure 2.7 (a)). When the network formed between CNT-CNT or CNT-polymer at a high filler amount, the blend dispersion showed an elastic-like behavior ($G' > G''$) at all measured frequencies (Figure 2.7 (b)). The entangled system with CNT also results in a curved shape $\log G' - \log G''$ plot due to the different response of rheology behavior to frequency when comparing with PAN solution. When $\log G'$ versus $\log G''$ curve is far above the $G' = G''$ line, failure to maintain continuous jetting tends to happen at high shear rates, and a relatively low shear rate (large diameter of capillary and/or low flow rates) may be required for fiber spinning. For example, fiber spinning with PAN/CNT-15 dispersion was achieved only with a 500 μm capillary hole at 0.5 ml/min flow rate (with a shear rate of about 84 s^{-1} , Table B3).

Figure 2.7(c) represents PAN/CNT dispersion at high CNT concentration relative to polymer but at low overall solid content. Cross-over of curves of $\log G'$ versus $\log G''$ and the $G' = G''$ line occurs with increasing frequency. Dispersion becomes predominantly viscous-like ($G' < G''$) at higher frequencies, which suggests a low degree of entanglement in the dispersion. Low entanglements may lead to jetting failure during spinning. Reducing the elasticity but ensuring adequate entanglements can help with continuous jetting for successful fiber spinning. Figure 2.7 (d) shows a more desirable condition for fiber spinning than Figure 2.7 (b) when $\log G'$ versus $\log G''$ and $G' = G''$ curve are close to each other across the frequency range. For instance, a lower M_v PAN was used to reduce the elasticity of the PAN/CNT dispersion at 10 wt% CNT. The resulting

$\log G'$ versus $\log G''$ is closer to the $G' = G''$ curve when compared to the dispersion with high M_v PAN (Figure 2.6 (a)) and exhibited longer sustained continuous jetting.

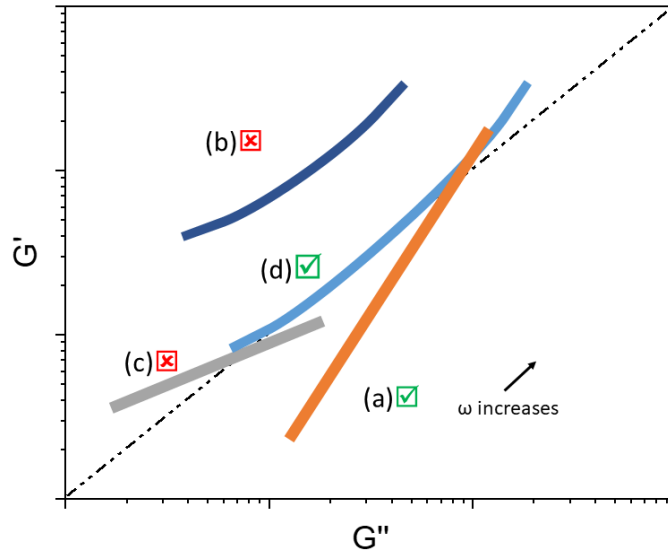


Figure 2.7. Schematic log-log plot of G' versus G'' of (a) PAN solution, or PAN/CNT at low CNT loading (0 or 4 wt% CNT); (b) highly elastic-like PAN/CNT dispersion at high CNT loading (15 wt% CNT), (c) relatively dilute PAN/CNT dispersion at high CNT loading (10 wt% CNT), and (d) PAN/CNT at high CNT loading (10 wt% CNT) with reduced elasticity relative to (b). Arrows indicate the direction of increasing frequency (ω). indicates that the solution/dispersion is desirable for continuous fiber spinning, indicates that the dispersion is not desirable for continuous fiber spinning; the formulation may lead to failure to jetting, frequent breakage of fiber spinning, or require spinning with low shear.

To check whether the above rheological behavior finding of PAN/CNT has some generality to other polymers/filler composites at relatively high filler loading, we looked at PAN/cellulose nanocrystal (CNC) system. CNCs generally have a lower aspect ratio (~30 to 40) than the CNTs used in this study (~250 to 500). Figure 2.8 (a) shows $\log G'$ versus $\log G''$ plots for PAN/CNC dispersions. For PAN/CNC-20 (80 wt % PAN + 20 wt % CNC), clear crossover with the $G' = G''$ line is observed. For PAN/CNC-40 (60 wt %

PAN + 40 wt % CNC), the $\log G'$ versus $\log G''$ curve was close to but slightly above the $G' = G''$ line, Both G' and G'' of PAN/CNC-60 were lower than those of PAN/CNC-40, which is likely due to the lower PAN concentration in PAN/CNC-40. Figure 2.8 (b) also shows that $\tan \delta$ decreases with an increased amount of CNC filler, which also indicates that the PAN solution became more elastic-like with increasing CNC. The shapes of the $\log G'$ versus $\log G''$ and $\tan \delta$ curves are also similar to those of the PAN/CNT-10 and PAN/CNT-15 shown in Figure 2.3 (a), and (b): the $\log G'$ versus $\log G''$ curves of PAN/CNC are at least partially above the $G' = G''$ line between 20 – 60 wt% CNC solid; while the $\tan \delta$ curves for the PAN/CNC dispersions either showed an increase in the low frequency range (0.63 – 10 rad/s), and a modest decrease at higher frequencies, or showed a constantly increase with increasing frequency.

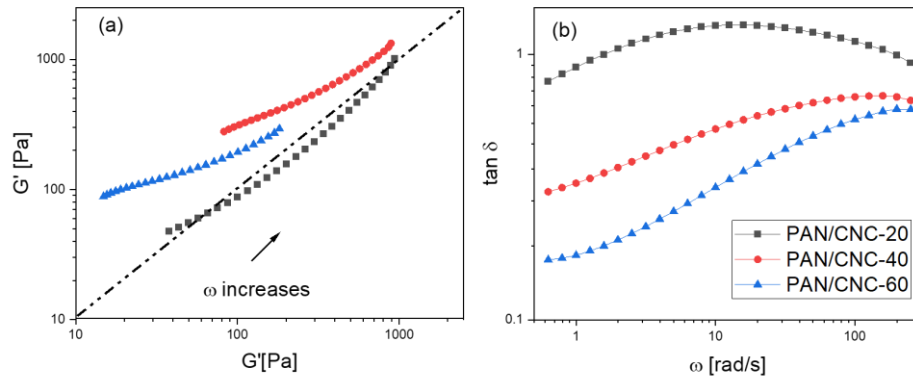


Figure 2.8. (a) Log-log plot of G' versus G'' , and (b) $\tan \delta$ as a function of ω for PAN/CNC dispersions measured at room temperature. Rheology data of PAN/CNC-20 and PAN/CNC-40 are from a study by Chang et al. [53]. PAN/CNC-60 was made in this work following the previous protocol.

Fiber spinning for PAN/CNC-20 and PAN/CNC-40 was achieved continuously without significant fiber breakage, at a high shear rate (with a shear rate of about 2600 s^{-1} , Table B3) with a $200 \mu\text{m}$ spinneret and 1 mL/min flow rate as reported previously[53].

PAN/CNC-60 did not result in continuous jetting with the 200 μm spinneret. More elastic-like behavior (lower $\tan \delta$) of PAN/CNC-60 dispersion as compared to PAN/CNC-20 and PAN/CNC-40 prevents continuous jetting. These studies show that elasticity is an important indicator of the spinnability of composite dispersions, which can be seen on the $\log G'$ versus $\log G''$ and $\tan \delta$ vs. frequency plots.

2.4 Conclusions

To summarize, the effect of CNT on the rheological behavior of PAN/CNT dispersions (0 – 15 wt% of CNT relative to total solids) was studied in the framework of fiber spinning. PAN/CNT dispersions become more elastic-like with increasing CNT amount. The empirical relationship between shear viscosity and complex viscosity, the Cox-Merz rule, held for the pure PAN solutions and PAN/CNT dispersions at most concentrations, except for the most concentrated PAN/CNT-15. PAN/CNT-15 shows lower values for η than η^* , and weaker power-law scaling factor of η with $\dot{\gamma}$ ($\eta \sim \dot{\gamma}^{-0.67}$) as compared to the scaling of η^* with ω ($\eta^* \sim \omega^{-0.75}$). The homogeneity of the solution or dispersion, indicated by the terminal slope of the $\log G'$ versus $\log G''$ curve, depended on the concentration of CNT but not on temperature between 0 and 60 °C. For PAN/CNT dispersions, $\tan \delta$ was less sensitive to temperature than for the pure PAN solution. Decreasing the dispersion elasticity by using lower molecular weight polymer assisted a longer continuous jetting during fiber spinning, as compared to the PAN/CNT dispersion with higher molecular weight polymer. The shape of $\log G'$ versus $\log G''$, as well as the $\tan \delta$ curves of PAN/CNC at CNC loadings of 20 – 60 wt%, were similar to those of PAN/CNT dispersions at 10 – 15 wt% CNT solids. Also, the highly elastic PAN/CNC-60

dispersion with low $\tan \delta$ showed a failure to jetting during fiber spinning, which was similar to PAN/CNT-15 under the same spinning conditions. For both PAN/CNT and PAN/CNC dispersions, rheological behavior provides a good indicator of fiber spinnability. The $\log G'$ versus $\log G''$ and $\tan \delta$ curves are recommended to guide fiber spinning with a simple oscillation measurement.

CHAPTER 3. STRUCTURE, PROPERTIES, AND APPLICATIONS OF POLYACRYLONITRILE (PAN)/CARBON NANOTUBE (CNT) FIBERS AT LOW CNT LOADING

3.1 Introduction

CNTs are being used as reinforcement material due to their good mechanical, electrical, and thermal properties [24,117,118]. High CNT loading of 20 wt% results in high conductivity of the polymer/CNT fibers, reaching up to 240 S/m [119]. However, high CNT loading also contributes to high raw material cost, as well as high energy cost for filler dispersion, and results in low mechanical strength of the fibers. The core-sheath geometry provides an alternative pathway for optimizing electrical conductivity and maintaining good mechanical properties while also reducing the amount of filler because the filler is only present in part of the fiber (either in the sheath or in the core). In the current study, core-sheath geometry was utilized to make PAN/CNT composite fibers via gel spinning. 10 wt % CNT was incorporated in the sheath, while the core was neat PAN copolymer. These core-sheath fibers have a combination of high electrical conductivity and good tensile properties. Joule heating was also demonstrated on these CNT containing fibers at overall CNT loading < 5 wt%.

3.2 Experimental procedures

Polyacrylonitrile-co-methacrylic acid (PAN) with viscosity average molecular weight (M_v) of 247,000, g/mol, and 4 wt% copolymer was obtained from Japan Exlan Co., Japan, and dried at 75 °C in a vacuum oven overnight. Multi-wall carbon nanotubes

(SMW200) were purchased from SouthWest NanoTechnologies, Inc. (SWeNT), Norman, OK., with a length of 3-6 μm . For these MWNTs, an average number of 9-10 walls and an average diameter of 12 ± 3 nm were determined by X-ray diffraction and SEM, respectively, in a previous study [120,121]. Dimethylformamide (DMF) was obtained from Sigma Aldrich (HPLC grade, >99.9% purity). Methanol (ACS grade) and glycerol were purchased from VWR Chemicals.

Two separate solution preparations were carried out, one for the sheath and another for the core. PAN/CNT solution was used as a sheath, and PAN (with no CNT) was used as core. CNT powder was homogenized in DMF at a concentration of 35mg/300 ml using a homogenizer (T25 ULTRA-TURRAX, IKA) at 10,000 rpm for 30 minutes. The slurry was then bath sonicated for 48-72 hours (Bransonic, 3510-MT, 8510) until reaching a dispersion state without macroscopic aggregates. Sonication breaks CNT bundles and clusters and is also known to reduce CNT length [122–124]. CNT/DMF dispersion was added into the reactor containing PAN solution with desired PAN solid content while stirring at 70 °C. Excess DMF solvent was evaporated using a vacuum distillation process at 70 – 80 °C. The addition process was continued until the desired concentration of CNT (10 wt% with respect to the weight of the polymer) was achieved. The final solid content (PAN and CNT) was 11.5 g/dL (90 wt% PAN + 10 wt% CNT) confirmed by thermogravimetric analysis test (TGA: Q-500 TA instrument). 14 grams PAN polymer was dissolved into 100 mL DMF solvent at 75 °C, and the solution was used for core component.

Fibers were spun using a single filament bi-component fiber spinning unit manufactured by Hills Inc. PAN, and PAN/CNT solutions were poured in respective

reservoirs to supply solutions to the core and the sheath geometries in the spin pack. Both solution reservoirs were maintained at 90 °C. The spin pack consisted of distribution plates to result in sheath-core geometry and single hole spinneret with a 200 µm spinneret diameter capillary. The extrudate was passed through a 50 mm air gap followed by a methanol bath at -50 °C. The sheath/core area ratio was controlled by changing the flow rates of core and sheath solutions. The one-stage hot drawing was conducted in a glycerol bath heated to 150 °C.

Tensile properties were measured using Favimat+ at 25.4 mm gauge length and at 1 %/s strain rate using at least 40 measurements per sample. Wide-angle X-ray diffraction (WAXD) was conducted using Rigaku Micromax-002 (operating voltage and current 45 kV and 0.50 mA) using CuK α ($\lambda = 0.1542$ nm). Diffraction patterns were analyzed by Area Max (Version 2) and MDI Jade (Version 9). Crystal size was calculated from data from the equatorial scan using Scherrer equation ($K=0.9$). Herman's orientation factor was calculated from the azimuthal scan of PAN crystalline planes ((200) and (010) at $2\theta = 17^\circ$) following the previously described method. [125,126] Fiber cross-sections were observed using an optical microscope (Leica DM2500 P). For this purpose, the fiber bundle was embedded into epoxy resin and microtomed (Leica, RM2255) in 7-10 µm thick sections before imaging under the optical microscope. The areas of both core and sheath of the fibers from the optical microscope images were measured using Image-J software with at least 20 measurements per sample.

The electrical conductivity of a fiber bundle (30 filaments) was measured using Keithley 2400 source meter using a two-point probe geometry with a distance of 10 mm between the two probes. The silver paste was applied at the test points on fibers to ensure

low contact resistance between the probes and fibers. Electrical conductivity was calculated from the measured electrical resistance and geometry of fibers. Electrical conductivities lower than 10^{-4} S/m could not be measured due to the limit of the source meter. Electrical conductivities of single-filament of three samples were also measured along the fiber axis using the standard four-point probe method (Signatone probe) with at least 15 measurements and compared with the results from 2-probe measurements (Table C1). The two probe methods and four-probe methods gave comparable results.

A scanning electron microscope (SEM, Hitachi SU8010) was used to obtain high-resolution cross-sectional images of the core-sheath fiber. Raman spectra were collected on a single fiber with a 785 nm laser on a Raman microscope system from HORIBA Scientific. The orientation of the CNTs in the composite fibers was determined using a rotation stage with the fiber axis rotated in 10° increments from 0 to 90° under parallel (VV, vertical/vertical) polarizers. The Herman's orientation factor of CNTs was determined following the previously reported procedure [11,127,128]. For each sample, 3 to 5 single fibers were measured under a Raman microscope, and the average value and standard deviation of orientation factor of CNTs are reported.

Joule heating was conducted following the protocol reported previously [96]. Voltage was applied using a DC power supply (Glassman) on a 1 m long fiber bundle containing 100 filaments. An IR temperature sensor was placed near the center of the fibers bundle to monitor the change in temperature. The details of the processing parameters are summarized in Table C2 in the supporting information.

3.3 Results and discussion

A number of bi-component fibers manufactured are listed in Table 3.1. A2 samples were further drawn to a draw ratio of 3 (sample A2-1) and 10 (sample A2-2). The draw ratio of fully drawn fiber A2-2 is comparable to the draw ratio of single component PAN/CNT fibers at 5 wt% CNT [129] and is higher than that for the single component PAN/CNT fibers at 10 wt% CNT [130]. Figure 3.1. Optical micrographs of PAN core and PAN-CNT sheath (with 10 wt% CNT in the sheath) bi-component fibers. shows the optical images of the cross-sections with different core-sheath area ratios. Figure 3.2 (a) and (b) show SEM of the core-sheath morphology and the core-sheath interface. In this case, the sheath is about 5 μm thick and uniformly surrounds the PAN core. The fibrillar entities, which are polymer-coated carbon nanotubes, are seen in Figure 3.2 (c)

Electrical conductivity as a function of the overall CNT wt% in the fibers is plotted in Figure 3.3 (a), and the values are listed in Table C3. The increased CNT concentration can result in an increased amount of formed CNT network, which is responsible for an increased probability of electron transfer within the PAN/CNT fibers [131–133]. Besides, multiple previous studies reported that the CNT orientation affects the percolation threshold as well as the maximum conductivity in polymer/CNT composite fibers. In general, the percolation threshold increases with increasing anisotropy of the conducting high aspect ratio rods [134]. However, Munson-MaGee et al. [135] and Du et al. [29] showed that slight alignment along the fiber axis, rather than isotropic CNTs contribute to the highest conductivity. In this work, the measured orientation factors of fibers A1-A4 are within the range of 0.1 – 0.25 (Table 3.2), which is relatively low but higher than isotropic.

Table 3.1. Summary of processing parameters of bi-component PAN core and PAN-CNT sheath fibers.

Sample	$A_{\text{core}}/A_{\text{fiber}}^*$	r_1/r_2^*	Draw ratio	Diameter (μm)	CNT wt%
A1	0.64	0.8	1	71 ± 2	3.7 ± 0.6
A2	0.58	0.76	1	71 ± 3	4.4 ± 0.3
A3	0.45	0.67	1	66 ± 3	5.6 ± 0.4
A4	0.34	0.58	1	64 ± 3	6.6 ± 0.5
A2-1	0.58	0.76	3	35 ± 2	4.4 ± 0.3
A2-2	0.58	0.76	10	20 ± 1	4.4 ± 0.3

* A_{core} -cross-sectional area of the core; A_{fiber} -cross-sectional area of fiber; r_1 - equivalent radius of core based on core area; r_2 - equivalent fiber radius based on the overall fiber cross-sectional area. Diameter - equivalent fiber diameter based on the overall fiber cross-sectional area.

The annealing process was shown to increase the electrical conductivity of as-spun fibers. Annealing at 180 and 210 °C for 30 minutes leads to comparable electrical conductivity for A2 samples (Figure 3.3 (b)). Annealing at 150 °C leads to lower conductivity than at 180 and 210 °C. Annealing for 3 min at 180°C enhanced the electrical conductivity of fibers (A1-A4) up to 2 orders of magnitudes (Figure 3.3 (c)). The conductivities of all four samples (A1-A4) were in the range of 1-10 S/m. Annealing above the glass transition temperature of the polymer has been reported to improve the electrical conductivity of polymer/CNT composites [34,133,136–138]. Increased mobility of the polymer chain at elevated temperature enables carbon nanotubes to rearrange themselves in the polymer matrix. Electrical conductivity can be enhanced with shortened tube-tube distance and an increased number of nanotube contacts. All A1-A4 samples annealed for 3 minutes at 180 °C show an increased orientation factor and crystal size of PAN than samples before annealing (shown in Tables 2 and 3). However, the measured CNT orientation factors were comparable before and after annealing considering the

experimental error. PAN crystal size increased from about 3 nm to 9 nm, which is consistent with the previous results [139]. PAN crystallinity of all as-spun samples increased moderately after annealing for 3 minutes at 180 °C. For as-spun fibers, the annealing process not only increases the crystal size and crystallinity of PAN but increases the chain mobility of the polymer chain for CNT re-arrangement as well. Also, unlike the previously reported methods of long-time annealing (~ 2-hours) used for enhancing electrical conductivity of PAN/CNT fibers [34,96], this work suggested short-time (~ 3 min) annealing could be sufficient for improving the electrical conductivity of such composite fibers.

Conductivity increased moderately with an increase in annealing time beyond 3 minutes (Figure 3.3 (c)). This increase after 3 minutes can be explained by the minor change in structure with longer annealing time. The structural change during annealing was monitored using WAXD (Table 3.3 and Figure C1). PAN orientation increased with annealing time, while crystallinity remained the same, and crystal size increased moderately. The crystal size increase is attributed to the rearrangement of crystals: the smaller crystals merge into larger crystals in PAN with no net significant change in crystallinity [139].

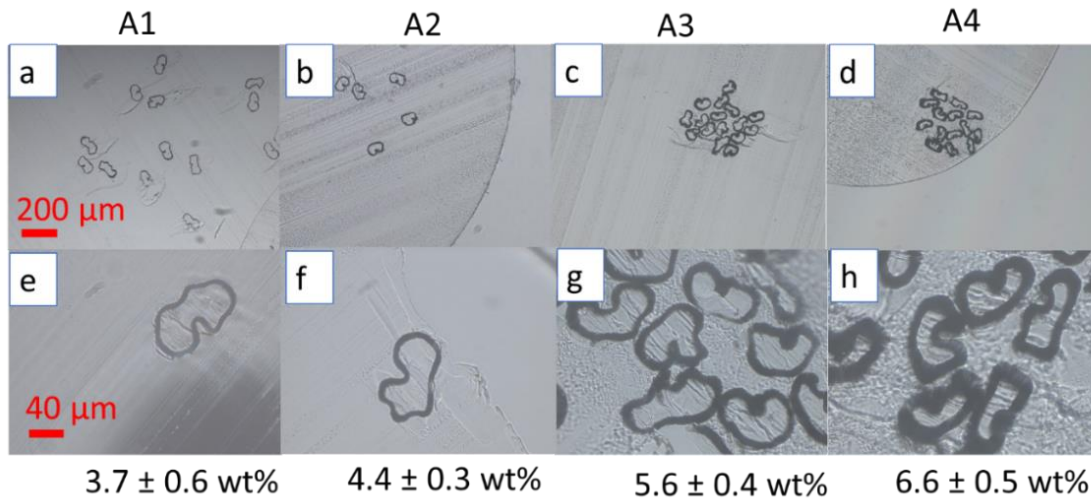


Figure 3.1. Optical micrographs of PAN core and PAN-CNT sheath (with 10 wt% CNT in the sheath) bi-component fibers.

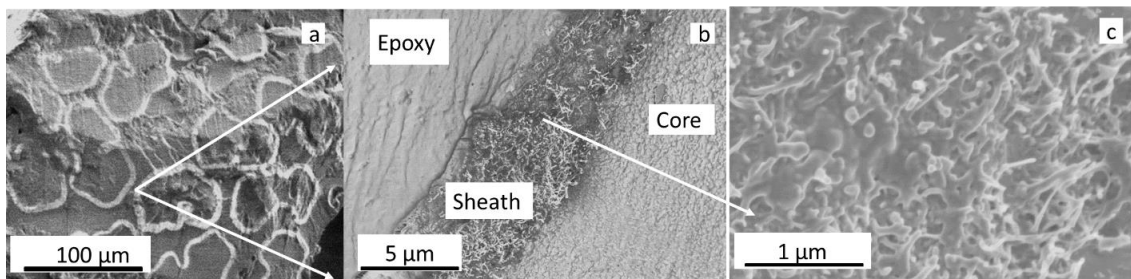


Figure 3.2. Scanning electron micrographs of A1 fibers embedded in epoxy. (a) low magnification image. (b) higher magnification image showing core-sheath interface morphology. (c) High magnification image showing CNTs embedded in PAN in the fiber sheath.

Figure 3.3 (d) shows the effect of drawing on electrical conductivity. Drawing to a draw ratio of 3 increased conductivity by about one order of magnitude from 0.05 S/m (A2) to 0.38 S/m (A2-1), while fully drawn fibers (A2-2, draw ratio 10) show significantly lower conductivity of less than 10^{-4} S/m. Drawing at a low draw ratio resulted in a similar effect as annealing: polymer chains gained increased mobility during a hot drawing at 150°C, and CNTs gained a chance to rearrange themselves to form CNT-CNT contacts [131–133]. To

an extent, this is confirmed by the increased orientation of both PAN ($f_{\text{PAN}} = 0.76$) and CNT ($f_{\text{CNT}} = 0.23$) for A2-1 sample, while A2 sample has much lower PAN and CNT orientation values ($f_{\text{PAN}} = 0.11$, $f_{\text{CNT}} = 0.13$). Fully drawn fibers (A2-2) possess much lower electrical conductivity than as-spun and low draw ratio fibers, and results in further increase in both PAN and CNT orientation as expected (Table 3.2, $f_{\text{PAN}} = 0.83$, $f_{\text{CNT}} = 0.35$). Increased anisotropy of filler along the fiber axis after drawing at high draw ratio of 10 can break the contacts between CNTs and disrupt the percolation, which was previously shown by Du et al. [29].

Annealing for 30 minutes increased electrical conductivity by one order of magnitude of low draw ratio sample (A2-1), while it increased by more than 2 orders of magnitude for fully drawn fiber (Figure 3.3 (d)). The rearrangement of CNT during the annealing process for the fully drawn fiber can be ascribed to the entropic relaxation of polymer chains [139]. After 30 minutes annealing, PAN orientation decreased from 0.83 to 0.76, while the PAN crystallinity and crystal size, as well as CNT orientation, remained the same. The entropic relaxation during annealing can result in the increased mobility of the PAN polymer chain and enabled the rearrangement of CNT. Rearrangement of tubes can lead to a high density of CNT contacts and an increase of electrical conductivity [34,137,138]

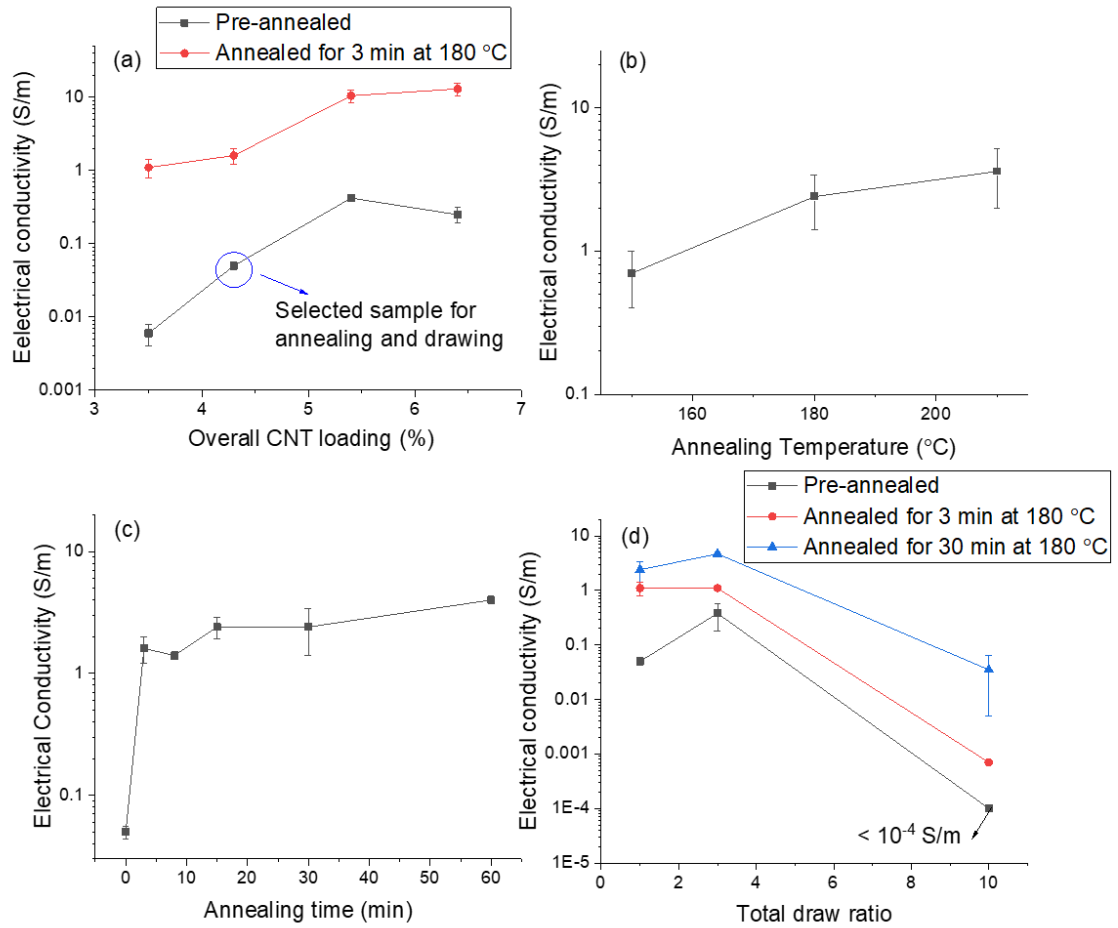


Figure 3.3. Electrical conductivity of (a) PAN core PAN-CNT sheath as-spun fibers with different CNT wt%. (b) A2 fibers after annealing for 30 minutes at different temperatures. (c) A2 fibers with various annealing times at 180°C. (d) A2 drawn fibers at 3 and 30 minutes of annealing at 180 °C. A2-2 pre-annealed fiber conductivity could not be measured and is less than 10^{-4} S/m.

Table 3.2. Structural parameters of PAN core and PAN-CNT sheath (90/10) fibers before annealing.

Sample		A1	A2	A3	A4	A2-1	A2-2
TDR		1	1	1	1	3	10
	Xc %	41	34	39	33	57	58
Structural parameters	Lc nm	2.9	3	2.7	2.8	10.3	11.8
	f _{PAN}	0.08	0.11	0.14	0.11	0.76	0.83
	f _{CNT}	0.18	0.13	0.11	0.23	0.23	0.35
	std*	0.08	0.03	0.04	0.06	0.08	0.07

*std – standard deviation of measured Herman’s orientation factor of CNT in fiber.

Xc- crystallinity of PAN, Lc, the crystal size of PAN, f_{PAN}, f_{CNT} – Herman’s orientation factor of PAN and CNT respectively.

Table 3.3. Structural parameters of PAN core and PAN-CNT sheath fibers after annealing.

Sample		A1	A2	A3	A4	A2	A2	A2-1	A2-2
TDR		1	1	1	1	1	1	3	10
Annealing time	min	3	3	3	3	30	60	30	30
	Xc %	46	46	42	44	49	49	59	59
Structural parameters	Lc nm	9.5	8.6	8.6	8.6	10.3	9.6	12.3	12.4
	f _{PAN}	0.21	0.21	0.37	0.22	0.45	0.43	0.73	0.76
	f _{CNT}	0.31	0.27	0.34	0.3	0.17	0.12	0.31	0.35
	Std	0.17	0.15	0.14	0.17	0.09	0.1	0.02	0.02

Tensile properties are listed in Table 3.4. Various as-spun fibers with different core-sheath ratios and CNT concentrations show comparable tensile strength, while tensile modulus slightly increased, and elongation to break decreased with increasing CNT wt%. Elongation at break of the A1 sample is approximately 3.4 times that of the A4 sample. Tensile strength, modulus, and toughness increased after drawing (Table 3.4). Both tensile strength and modulus increased by more than a factor of 2, at a draw ratio of 3. The increase

in crystallinity and orientation is responsible for the increased tensile properties. The A2-2 sample showed comparable crystallinity and crystal size to the A2-1 sample but moderately increased the PAN orientation factor from 0.76 to 0.83. The higher orientation in the A2-2 sample led to a higher modulus (18.8 GPa) than that for the A2-1 sample (12.7 GPa) with a lower draw ratio.

Table 3.4. Mechanical properties of the core-sheath fibers.

Sample	A1	A2	A3	A4	A2-1	A2-2
CNT wt%	3.7	4.4	5.6	6.6	4.4	4.4
TDR	1	1	1	1	3	10
Diameter (μm)	71 ± 2	71 ± 3	66 ± 3	64 ± 3	35 ± 2	20 ± 1
Tensile Strength (MPa)	112 ± 5	112 ± 6	125 ± 13	117 ± 26	299 ± 25	570 ± 102
Tensile Modulus (GPa)	5.7 ± 0.3	5.8 ± 0.3	7.0 ± 0.3	7.0 ± 0.3	12.7 ± 1.0	18.8 ± 1.2
Elongation at break (%)	14.3 ± 4.5	10.7 ± 3.3	4.6 ± 2.0	4.2 ± 2.5	9.7 ± 1.1	6.0 ± 1.4
Toughness (MPa)	2.8 ± 0.2	2.8 ± 0.3	2.7 ± 0.8	2.5 ± 1.2	20.7 ± 3.0	19.8 ± 7.2

Table 3.5 summarizes the structural, mechanical, and electrical data of A2 fibers (with 4.4 wt% CNT) at different draw ratios. The drawing process changed the structure and morphology of fibers, then further resulted in the enhancement of tensile properties and change of electrical conductivities. Among fibers with 3 different draw ratios, A2-1 samples showed good electrical conductivity enhancement (10^{-1} S/m before and 1-10 S/m after annealing) and relatively good tensile strength and modulus (299 MPa and 12.7 GPa). These fibers can be used for strain sensors and electromagnetic interface (EMI) shielding [26,45,140–148]. The electrical conductivity of the as spun and low draw ratio sheath-core fibers with overall 4.4 wt% CNT is comparable to the conductivity of PAN/CNT single component fibers with 15 wt% CNTs [96], and thus represents a significant development

in the processing of multifunctional fibers. These fibers can also be used for Joule heating of fabrics and to stabilize PAN polymer for making carbon fibers also via Joule heating process.

Table 3.5. Structural parameters, morphology, electrical conductivity, and mechanical properties of various A2 core-sheath fibers containing 4.4 wt% CNTs and different draw ratios.

		A2	A2-1	A2-2
Draw ratio		1	3	10
Structural properties	X _c (%)	34	57	59
	L _c (nm)	3	10.3	11.8
	f _{PAN}	0.11	0.76	0.83
	f _{CNT}	0.13	0.23	0.35
Electrical conductivity (S/m)	Before annealing	0.05	0.38	<10 ⁻⁴
	After annealing	1- 10	1- 10	10 ⁻⁴ -10 ⁻¹
Mechanical properties	Tensile strength (MPa)	112	299	570
	Tensile modulus (GPa)	5.8	12.7	18.8

We demonstrate Joule heating on sample A1. A1 fibers, of overall 3.7 (\pm 0.6) wt% CNT wt%, possessed 0.006 ± 0.002 S/m before and 3.0 ± 2.6 S/m electrical conductivity after annealing for 30 minutes at 210 °C (Table C3). During Joule heating, temperature up to 250 °C was recorded near the center of the fiber bundles by an IR sensor (Table C2) with the applied voltage between 1.2 and 1.5 kV. Figure 3.4 shows the integrated scan from WAXD of various fibers. The annealing process increased the PAN crystal size of the A1 sample from 3 nm to 8 nm at $2\theta \sim 17^\circ$ (200,110 plane), which was observed for other as-spun fibers as well (Table 3.2 and Table 3.3). PAN crystal peak at $2\theta \sim 17^\circ$ became broader after 1-hour Joule heating, and its intensity decreased after longer Joule heating time. The

peak at $2\theta \sim 26^\circ$, which indicates the stabilized PAN structure appeared after Joule heating [96,149–152]. After 3-hours of Joule heating, the WAXD PAN peak at $2\theta \sim 17^\circ$ almost fully disappeared. Thus the stabilization via Joule heating has been successfully demonstrated at an overall CNT loading of 3.7 wt-%, as compared to the 15-20 wt% CNT demonstrated previously [96].

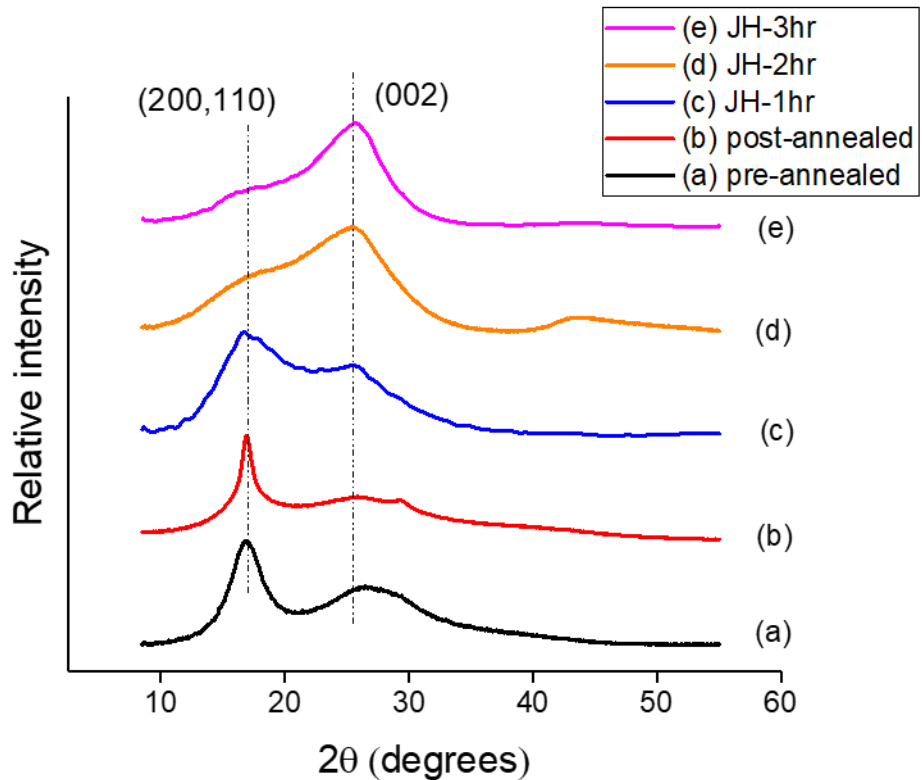


Figure 3.4 (a) before annealing, (b) after annealing at 210 °C for 30 minutes at constant length, (c, d, e) Joule heating (JH) between 1.2 – 1.5 kV for 1, 2, and 3 hours. (a) before annealing, (b) after annealing at 210 °C for 30 minutes at constant length, (c, d, e) Joule heating (JH) between 1.2 – 1.5 kV for 1, 2, and 3 hours.

3.4 Conclusions

PAN core and PAN-CNT sheath fibers were successfully manufactured with different core-sheath area ratios. The conductivity of as-spun fibers, with relatively small

PAN crystal size and crystallinity, can be increased with few minutes of annealing or at a low draw ratio, when CNTs can rearrange themselves to form CNT-CNT contacts. The conductivity of drawn fibers can be increased by annealing, and the polymer chains relaxed after annealing. At a low draw ratio of 3, sheath-core fiber with an overall CNT concentration of 4.4 wt% exhibited axial electrical conductivity of 0.38 S/m before annealing and up to 5 S/m after annealing. The tensile strength and modulus of this fiber were 299 MPa and 12.7 GPa, respectively. Therefore, we now have a fiber with tensile properties typical of textile fibers, but also exhibiting good electrical conductivity, at a relatively low CNT concentration. Lastly, such core-sheath fibers with overall CNT loading as low as 3.7 wt% were used to demonstrate stabilization of PAN by Joule heating.

CHAPTER 4. STABILIZATION OF POLYACRYLONITRILE (PAN) FIBERS WITH CARBON NANOTUBES (CNT)

4.1 Introduction

Among all the carbon fiber manufacturing steps, stabilization is the critical step for the formation of the desired cyclized ladder structure, and to a large extent, this structure determines the properties of the carbon fibers. However, stabilization requires a long residence time due to the oxygen diffusion limitation and is commonly regarded as the rate-limiting step for carbon fiber manufacturing [153,154]. Multiple approaches have been used to accelerate stabilization. For example, acid groups [69], lignin [71], and cellulose nanocrystals (CNC) [72] were incorporated into the PAN molecules to reduce the activation of cyclization and to accelerate the stabilization process.

CNTs have good mechanical, electrical, and thermal properties and have been widely used to reinforce polymer matrices [155]. CNTs have been incorporated into PAN fibers for improving mechanical properties [24,156] and electrical and thermal conductivity [96,130]. In this study, we illustrate a new pathway to increase the rate of reaction and to reduce the time of PAN stabilization with CNT.

4.2 Experimental procedures

4.2.1 Materials

Polyacrylonitrile-co-methacrylic acid (PAN) of average molecular weight M_v about 247,000 and 500,000 g/mol, and 4 wt% methacrylic acid was obtained from Exlan Co.

Japan. PAN powder was dried at 75 °C in a vacuum oven overnight before making solutions. Multi-wall carbon nanotubes (SMW200) were purchased from SouthWest NanoTechnologies, Inc. (SWeNT), Norman, Oklahoma, and had an average length of 3-6 μm . An average number of 9-10 walls and average diameter of $(12 \pm 3 \text{ nm})$ were determined by X-ray diffraction and SEM analysis, respectively, in previous work[106]. Dimethylformamide (DMF) was purchased from Sigma Aldrich (HPLC grade, >99.9% purity). Methanol (ACS grade) and glycerol were obtained from VWR Chemicals.

4.2.2 *Fiber manufacturing*

For manufacturing bi-component core-sheath fibers, two separate solutions were prepared: one for the sheath and the other for the core component. PAN powder ($M_v = 247,000 \text{ g/mol}$) was dissolved in DMF at a solid concentration of 14 g/dL for core component. For the sheath component, PAN/CNT solution/dispersion was prepared at a solid content of 11.5 g/dL (10 wt% CNT + 90 wt% PAN of $M_v = 247,000 \text{ g/mol}$). CNT was first dispersed in DMF at 35 mg/300 mL DMF through bath sonication (Bransonic 8510) for 48 hours, and the resulting dispersion was added into the PAN solution in DMF with the desired PAN solid content. Excess solvent was removed through vacuum evaporation at about 70 °C.

The core-sheath fibers were made using a bi-component fiber spinning unit (Hills Inc.) PAN and PAN/CNT solutions were poured into respective reservoirs to supply solutions to the core and the sheath geometries in the spin pack. Distribution plates in the spin pack of the fiber spinning equipment resulted in a core-sheath geometry through a 200 μm spinneret diameter capillary. The core-sheath ratio was controlled by changing the flow

rates of the core and sheath solutions. The control samples were made using the same fiber spinning unit with only PAN solution at a concentration of 15 g/dL ($M_v = 247,000$ g/mol) dissolved in DMF. 15 g/dL solid content was used to make PAN solution with complex viscosity of ~ 50 Pa s at 1 rad/s which is suitable for continuous single-component fiber spinning with the current experimental setup. Single-component PAN/CNT (90 wt% PAN + 10 wt% CNT) fibers were spun from a different PAN/CNT solution with PAN of $M_v = 500,000$ g/mol at 9 g/dL solid content in DMF. A high molecular weight PAN was used to make dispersion with reduced solid content and produce a fiber with a small fiber diameter. The solution was made following the same process as mentioned before. All fibers were spun through an air gap of 50 mm into a methanol coagulation bath at -50°C . All as-spun fibers were drawn in a glycerol bath maintained at $150\text{-}155^\circ\text{C}$. Stabilization was also carried out in a convection oven (VWR vacuum oven) at constant length with airflow.

4.2.3 *Fiber characterization*

Tensile properties of the as-spun fibers were measured by Favimat+ at 25.4 mm gauge length and 1 %/s strain rate with at least 30 measurements. The area ratio of core and sheath and CNT concentration in core-sheath fibers were determined by imaging of cross-sections of fibers using an optical microscope (Leica DM2500 P) with at least 20 measurements and analyzing with an ImageJ (version 6) software. Wide-angle X-ray diffraction (WAXD) measurements were conducted using Rigaku Micromax-003 (operating voltage and current 50 kV and 0.6 mA respectively) using $\text{CuK}\alpha$ ($\lambda = 0.1542$ nm). Diffraction patterns were analyzed by Area Max (Version 2) and MDI Jade (Version

9). A scanning electron microscope (SEM, Hitachi SU8230) was used to obtain high resolution images of fibers.

Differential scanning calorimetry (TA Instrument Q200) under nitrogen and under air at various heating rates (5, 10, and 15, 20 °C/min) from 30 °C to 400 °C was performed to study and differentiate cyclization and oxidation reactions for PAN and PAN/CNT fibers.

4.3 Results and discussion

Table 4.1 summarizes the area ratios, overall CNT wt%, draw ratio, and tensile properties of fibers used in the study. The area ratio of PAN/CNT over the total cross-section area varied between 0 (PAN) to 100% (PAN/CNT-3). PAN/CNT-1, with 4.4 wt% CNT, showed the same draw ratio as the control PAN fiber, while the draw ratio of PAN/CNT-2 (with 6.6 wt% CNT) was lower. On the other hand, PAN/CNT-3 fiber had a larger diameter than the other three fibers due to a significantly lower draw ratio. All fibers show the comparable tensile modulus (16 -19 GPa) and strain at break (6 -9 %) (data in Table D1).

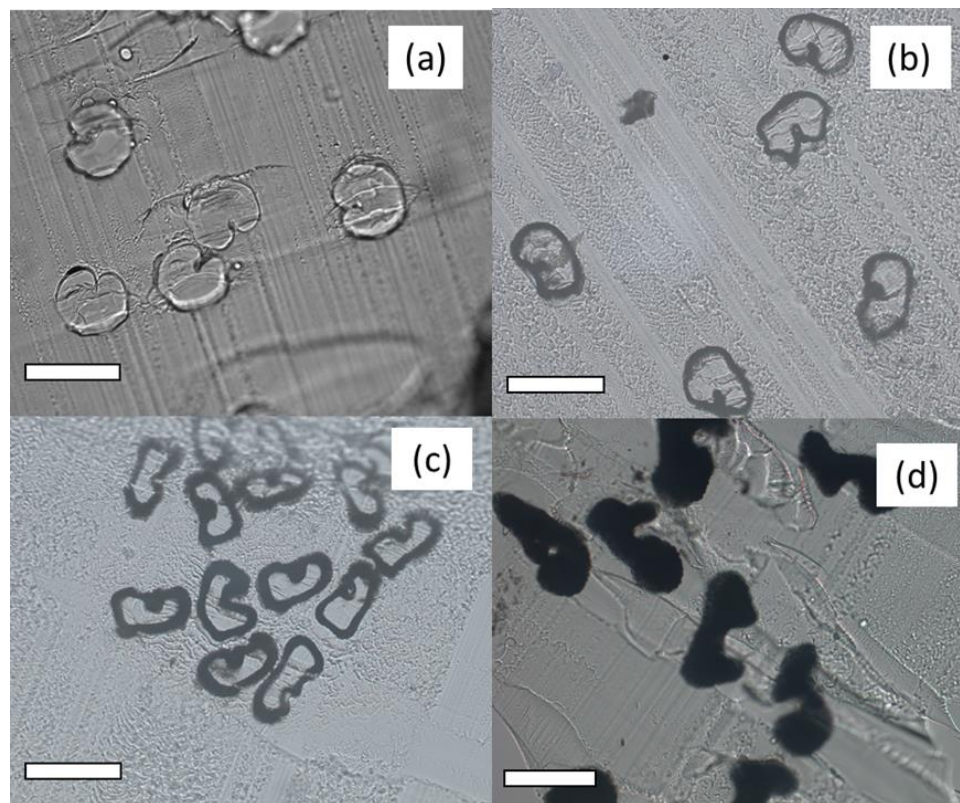


Figure 4.1. Optical image of cross-sections of as-spun fibers of (a) PAN, (b) PAN/CNT-1, (c) PAN/CNT-2, and (d) PAN/CNT-3. The scale bar represents 100 μm . PAN/CNT (10wt%) appears in black color in these optical images.

Table 4.1. Area ratios, CNT wt%, draw ratios, and diameters of various fibers.

Sample	PAN	PAN/CNT-1	PAN/CNT-2	PAN/CNT-3
$A_{\text{PAN-CNT}}/A_{\text{total}} (\%)$	0	43 ± 3	64 ± 5	100
CNT wt%*	-	4.4 ± 0.3	6.6 ± 0.5	10
Draw ratio	10	10	7	4
Diameter (μm)	21 ± 1	20 ± 1	23 ± 1	26 ± 1

Figure 4.2 (a) shows various DSC plots, and for comparison, the DSC for PAN powder is also presented. The $\Delta H_{\text{reaction}}$ for various PAN/CNT samples are corrected for PAN weight percentage (i.e., in J per gram of PAN) and summarized in Figure 4.3.

PAN/CNT fibers exhibited a much higher heat of reaction than control PAN fibers. For core-sheath fibers, $\Delta H_{reaction}$ increased with increasing PAN/CNT. In fact, the $\Delta H_{reaction}$ of PAN/CNT-3 (4517 J/g, corrected based on PAN wt%) was close to that of the PAN powder (4738 J/g). $\Delta H_{reaction}$ of PAN fiber (1561 J/g) was only 32 % of the PAN powder. PAN/CNT-3 fibers showed 20 % lower $\Delta H_{reaction}$ when compared to the PAN/CNT-2 fibers. Fiber diameter also influences the stabilization besides the CNT. The heat of the stabilization reaction is related to the surface area to volume ratio (SA: V), and a smaller SA: V can lead to a lower diffusion rate of oxygen per unit mass [29]. The larger diameter of PAN/CNT-3, compared to PAN/CNT-2 fiber (26 versus 23 μm), led to a smaller surface to area ratio, lower O_2 diffusion rate, and hence lower $\Delta H_{reaction}$.

When running under nitrogen, the $\Delta H_{reaction}$ of all fibers were close to that of the PAN powder (474 J/g, Figure 4.2 (b) and Figure 4.3). The data suggest that CNTs and polymer geometry (fiber vs. powder) did not affect the cyclization reaction, which occurs both in air and in nitrogen. However, the samples containing CNTs and fibrous geometry vs. powder resulted in significant variation in the heat of oxidation. Moreover, the absolute value of $\Delta H_{reaction}$ in air for PAN powder was about 10 times that of the running in N_2 , which showed that the heat released from the cyclization reaction only accounted for a small portion of the heat released from the overall stabilization reaction.

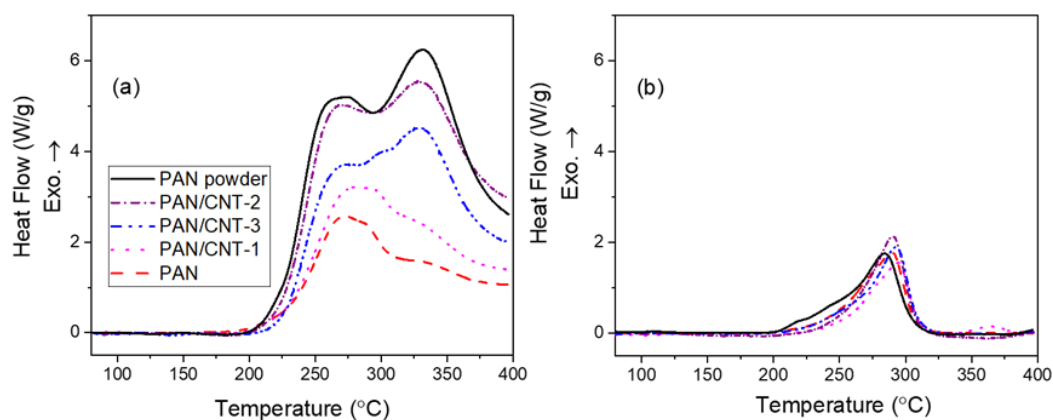


Figure 4.2. DSC curves of PAN, PAN/CNT fibers, and PAN powder under (a) air and (b) N₂ at 10 °C/min. The area under the DSC curves was used to calculate the heat of reaction, as shown in Figure D1.

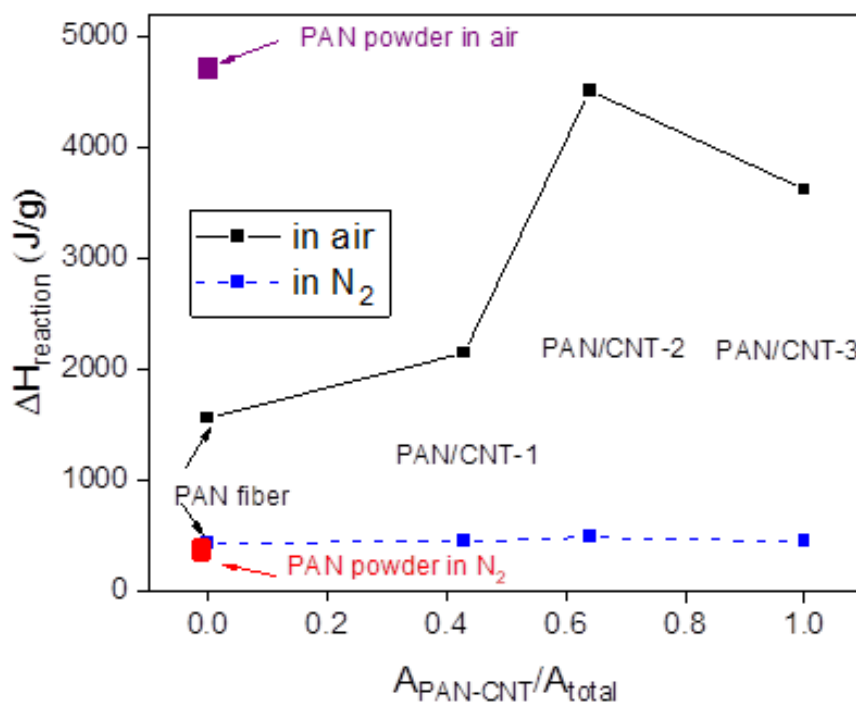


Figure 4.3. The heat of stabilization ($\Delta H_{\text{reaction}}$) of various samples in air and in N₂. $\Delta H_{\text{reaction}}$ of PAN/CNT fibers were corrected for PAN weight percentage.

We also compared the activation energies (E_a) of cyclization and oxidation reactions. During stabilization, PAN fibers undergo simultaneous reactions, including cyclization, oxidation, cross-linking, and dehydrogenation [65]. Fibers were measured under N_2 first followed by air to study the kinetics of the cyclization (exothermic peak in N_2) and oxidation reactions (1st exothermic peak when running in the air after running in N_2) separately [10,71,72,157–160]. Representative DSC scans of PAN and PAN/CNT-1 fibers under N_2 and rerun in the air are shown in Figure D2.

The kinetic parameters of the cyclization and oxidation reactions were fitted by Kissinger's method (equation 4-1) [161]:

$$-\frac{E_a}{R} = \frac{d\left(\frac{\phi}{T_p^2}\right)}{d\left(\frac{1}{T_p}\right)} \quad (4-1)$$

Where ϕ , T_p , E_a , R are heating rate ($^{\circ}C/min$), peak temperature (in Kelvin), activation energy, and universal gas constant ($8.3415 \text{ J/mol}^{-1}\text{K}^{-1}$), respectively. The pre-exponential factor A was calculated by equation (4-2) [162]:

$$A = \frac{\phi E_a}{RT_p^2} e^{\frac{E_a}{RT_p}} \quad (4-2)$$

Four heating rates (5, 10, 15, and 20 $^{\circ}C/min$) were used in this study, and fitting curves are shown in Figure D3. E_a values of oxidation and cyclization are summarized in

Table D2. E_a values of oxidation are apparent values since they account for both the oxygen diffusion and oxidization kinetics.

Figure 4.4 shows that the E_a of cyclization reaction slightly decreases with an increasing area ratio of $A_{\text{PAN-CNT}}/A_{\text{total}}$ or with the increasing amount of CNT. The E_{a_cyc} (cyclization) of PAN/CNT-3 (164 kJ/mol) was about 88% of E_{a_cyc} the control PAN fibers (187 kJ/mol). On the other hand, the E_{a_oxid} (oxidation) showed a significant increase in the presence of CNT. The E_{a_oxid} of PAN/CNT-1 and PAN/CNT-3 are about 1.2 to 1.3 times (81-88 kJ/mol) PAN fiber and E_{a_oxid} of PAN/CNT-2 is about 1.8 times (122 kJ/mol) when compared with the control PAN fiber (66 kJ/mol). A higher energy barrier must be overcome for PAN/CNT fiber than for PAN fiber for the oxidation reaction, which is caused by diminished oxygen diffusion in CNT-containing fiber. CNT has previously been shown to increase the activation energy associated with oxygen diffusion within polystyrene/CNT composite films [163]. Overall, CNT slightly reduced the E_a of PAN cyclization (up to 12%) but significantly increased the E_a for PAN oxidation (up to 80%).

Besides activation energy (E_a), the apparent kinetic constants (k) of both oxidation and cyclization reaction are shown in Figure S4. The k values were calculated by the Arrhenius equation (4-3):

$$k = Ae^{-E_a/RT} \quad (4-3)$$

Where R is the gas constant, and T is the temperature in K.

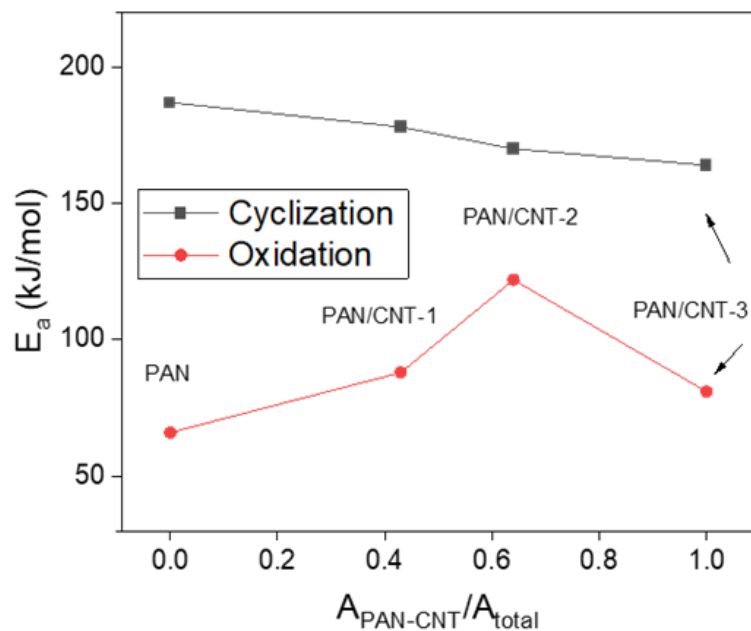


Figure 4.4. Activation energies (E_a) with different $A_{PAN-CNT}/A_{total}$ area ratios.

Kinetic constants for cyclization are comparable for all PAN and PAN/CNT fibers from 200 to 300 °C (Figure D4). For example, at 250 °C, $k_{cyclization}$ was between 0.027 and 0.036 s⁻¹ for all four fibers. At the same temperature, the $k_{oxidation}$ of PAN/CNT-1 and PAN/CNT-3 was twice (1.5 s⁻¹), and PAN/CNT-2 was 5 times (3.6 s⁻¹) that of control PAN fibers (0.7 s⁻¹). The increase of $k_{oxidation}$ and the comparable $k_{cyclization}$ with CNT were also consistent with the results of $\Delta H_{reaction}$ measured in air and N₂ (Figure 4.2 and Figure 4.3): $\Delta H_{reaction}$ increased with CNT under air environment with both oxidation and cyclization, while $\Delta H_{reaction}$ remained the same under N₂ atmosphere with only cyclization reaction. Moreover, the $k_{oxidation}$ of PAN/CNT-3 was lower than PAN/CNT-2, which was also consistent with the $\Delta H_{reaction}$ results shown in Figure 3. The larger fiber diameter of

PAN/CNT-3 compared to PAN/CNT-2 may also influence the kinetic constant, in addition to effects of the CNT.

To further demonstrate the CNT effect on stabilization, we carried out stabilization of a 20-filament bundle of 18 cm length in a convection oven at 250 °C at a constant length. Figure 4.5 shows the WAXD integrated scan of stabilized fibers. PAN/CNT-2 was fully stabilized within 2 hours, as indicated by the disappearance of the characteristic peak of PAN at 17° (200,110 plane, Figure D5) and the appearance of a peak at ~26° (002 plane), which indicated a stabilized structure [150–152]. On the other hand, the control PAN fibers were partially stabilized when the ratio of peak intensities at 17° and 26° was almost 1 from the WAXD integrated scan. Additional experiments were conducted for PAN fibers, and the structure development was shown by using WAXD. The 17° peak gradually disappeared over 2 hours to 6 hours (Figure D6). After 6 hours of stabilization, control PAN fibers fully stabilized when the 17° peak completely disappeared. Moreover, the WAXD patterns of PAN/CNT-1 and PAN/CNT-3 fibers after 2 hours of stabilization were comparable to that of the control PAN fibers after 5-hours of stabilization (Figure D6). CNT reduced the overall stabilization time for PAN/CNT fibers compared with PAN fibers. The results from the stabilization experiments were also consistent with the results by the DSC study that CNT increased the rate of stabilization.

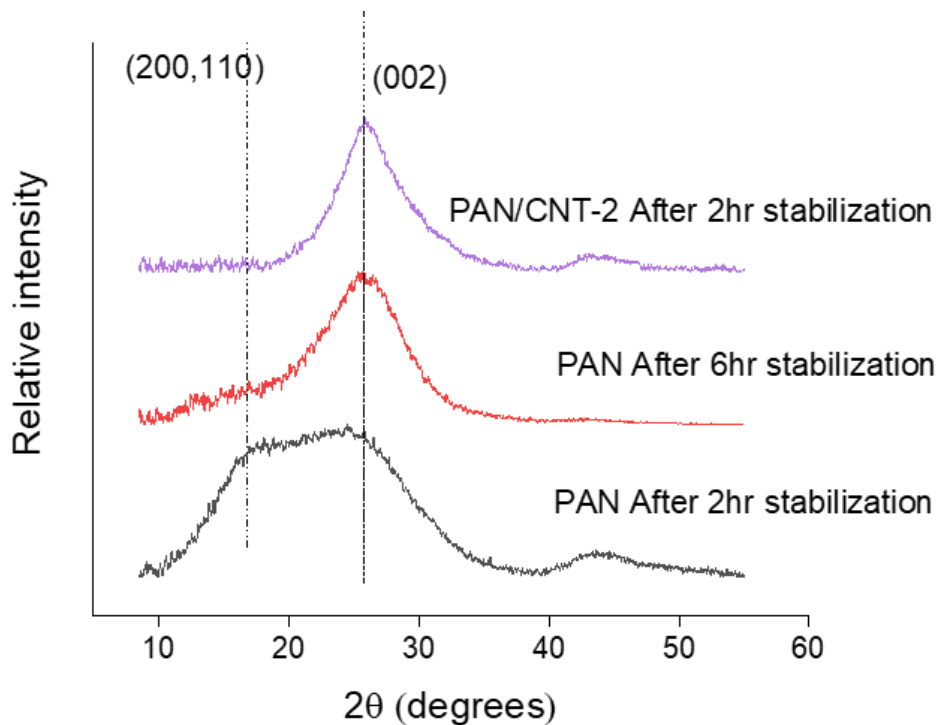


Figure 4.5. Integrated WAXD scans of PAN and PAN/CNT-2 fibers after stabilization in the air for the indicated times.

To understand why CNT increased the rate of stabilization reaction, we checked the morphology of fibers before and after stabilization under SEM. Figure 4.6 shows the SEM images of the precursor fiber surfaces and cross-sections. No porosity was observed in PAN fiber (Figure 4.6 (a) and (d)). On the other hand, porous features were observed in PAN/CNT fibers, and increased porosity was observed with an increasing amount of CNT (Figure 4.6 (e) and (f)). PAN/CNT-3 showed a highly porous structure. (Figure 4.6 (f)). However, CNT did not induce any porous structure on fiber cross-sections for PAN/CNT-2 and PAN/CNT-3 fibers (Figure 4.6 (f)). Porous features on the fiber surface were also observed in previous literatures on PAN fiber with 20 wt% CNT [130] and PAN/iron oxide fibers (10 wt%) [125].

No porous features were observed for PAN fibers, even after stabilization (Figure 4.7 (a), (d), and (g)). Porous structure was observed for stabilized PAN/CNT-2 (Figure 4.7 (h), (b), and (e)). Likewise, pores were shown on the fiber surface (Figure 4.7 (i)), and pores were shown across the whole cross-section for PAN/CNT-3 single-component fibers (Figure 4.7(c) and (f)). Figure 4.6 (b) and (c) suggest that the porous features may exist before stabilization (e.g., the coagulation stage during fiber fabrication). Also, Figure 4.7 (e) and (f) shows that stabilization promotes the formation of a 3-D porous structure. To the best of the authors' knowledge, the effect of stabilization on promoting or causing a formation of the porous structure has not been reported before for PAN/CNT or PAN with other filler. In Figure 4.4, the activation energy of the cyclization reaction was shown to reduce with the adding CNT. The CNT may promote the cyclization reaction in the vicinity of the tubes. The nitrile groups of PAN chains can form a ring by intramolecular addition within one molecule or form an acrylic bond between two macromolecules by intramolecular addition, which will lead to chemical shrinkage [164]. And the different rates of cyclization near and far from the CNTs may lead to the different shrinkage rates and promote the formation of the porous structure. This point needs further investigation.

The core-sheath structure became especially interesting when the fiber had a solid oxidized PAN core and porous sheath. The porous structure can be beneficial to both gas diffusion and heat convection. The 3-D porous network manufactured from a continuous process in a fiber form can also be interesting for applications such as electrodes [165].

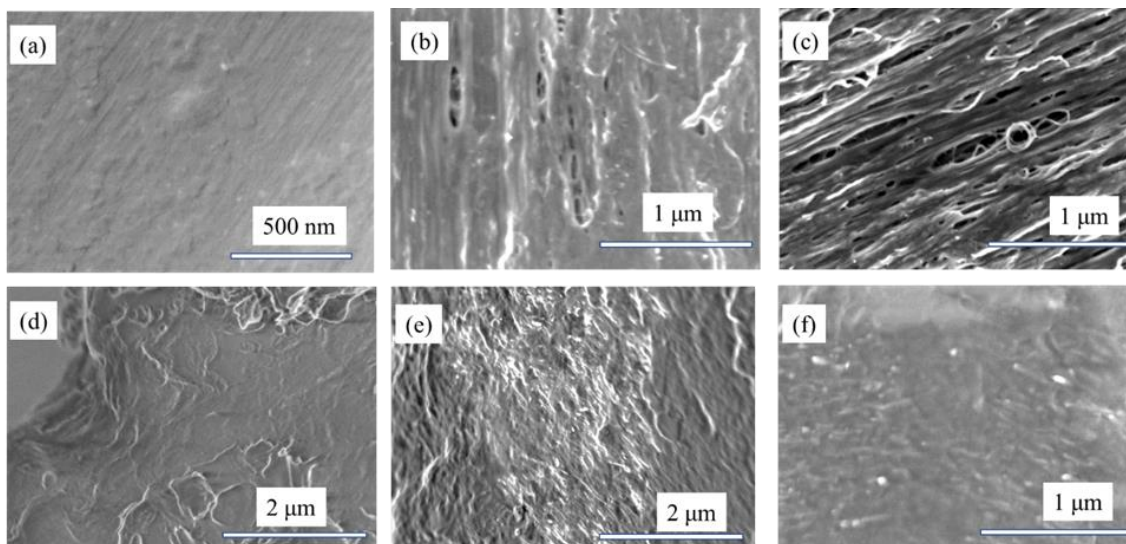


Figure 4.6. Representative surface (upper) and cross-section (lower) of (a)&(d) PAN, (b)&(e) PAN/CNT-2, (c)&(f) PAN/CNT-3 precursor fibers before stabilization.

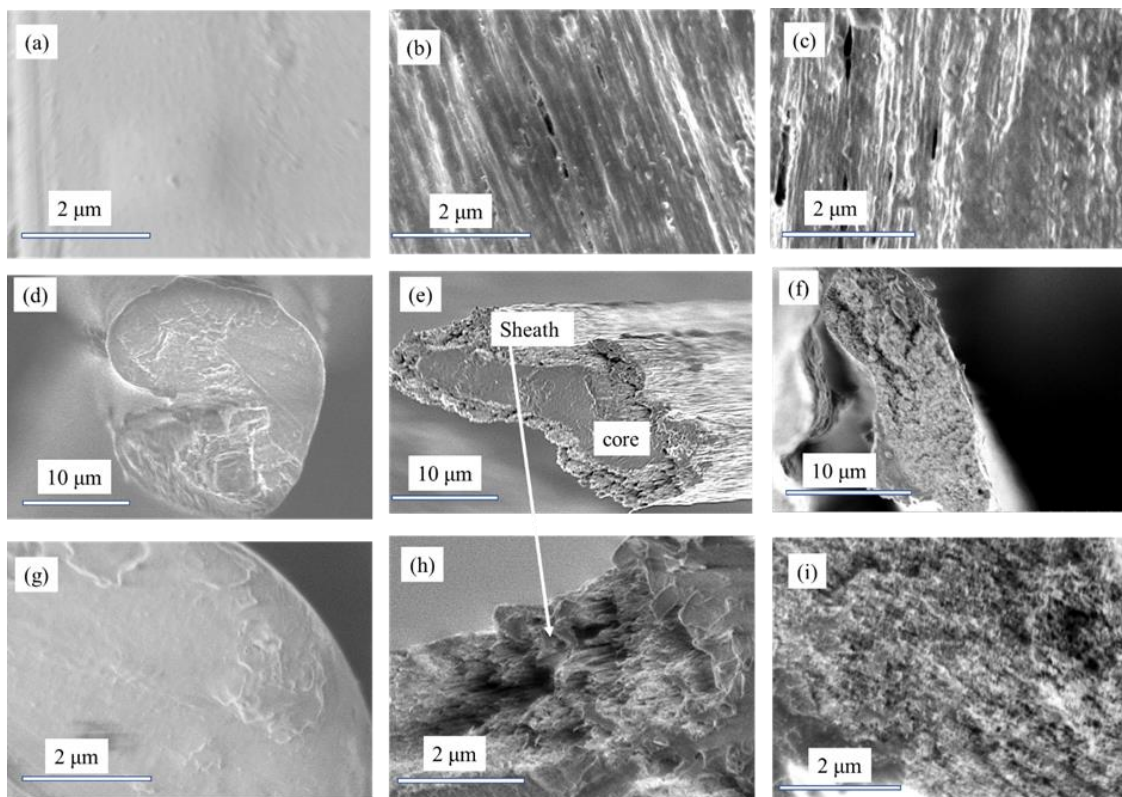


Figure 4.7. Representative surface (upper) and cross-section (middle and lower) of (a), (d)&(g) PAN, (b), (e)&(h) PAN/CNT-2, (c), (f)&(i) PAN/CNT-3 fibers after stabilization.

Figure 4.8 shows the schematic plot core-sheath PAN-PAN/CNT fibers during stabilization. Typically, the oxidized PAN layer would form an interphase (skin layer) near the fiber surface, which limits the further diffusion of oxygen inside the fiber and reduces the rate of oxidation reaction [76]. In the PAN/CNT fiber, the porous structures in PAN/CNT sheath can prevent interphase formation in the sheath component. The interphase formed in the PAN core during stabilization, as shown in Figure 4.8. The porous sheath also promotes O₂ diffusion, which can increase the stabilization rate.

We assessed the effect of porous structure on the O₂ diffusion by estimating the average apparent diffusion coefficient of O₂ (D_{O_2}), which described how fast oxygen could diffuse through the fiber. D_{O_2} was estimated to increase up to 3 times for PAN/CNT-2 fibers when compared to PAN fibers using a transient diffusion equation: $\frac{\partial C}{\partial t} = D_{O_2} \nabla^2 C$ (Figure D7, the calculation was shown in the supporting information).

Single-component PAN/CNT also had a faster stabilization reaction than control PAN fiber due to increased D_{O_2} than PAN fiber. However, in comparison with core-sheath structure fibers, single-component PAN/CNT fibers showed a lower draw ratio and relatively larger diameter, which would result in increased O₂ diffusion time. In addition, the porous structure would potentially reduce the tensile properties of the fiber. However, the solid core in the core-sheath fiber would contribute to tensile properties when compared to a single-component fiber with a complete porous structure.

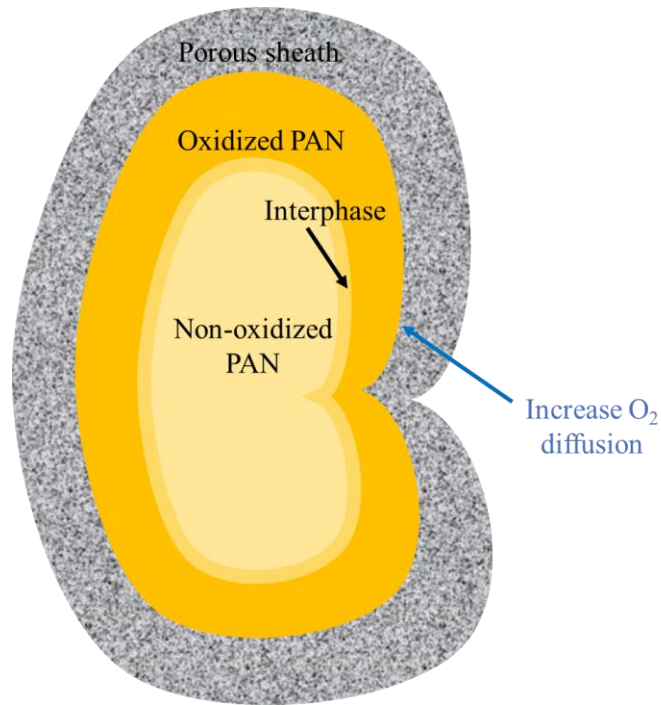


Figure 4.8. Schematic plot of core-sheath fibers with PAN/CNT sheath during stabilization.

4.4 Conclusions

Bi-component core-sheath PAN-PAN/CNT fibers and single-component PAN/CNT fibers were spun by incorporating 10 wt% CNT into the PAN matrix. CNT increased the $\Delta H_{reaction}$ of stabilization by up to 3 times when compared with control PAN fibers under an air environment. While under an N_2 environment $\Delta H_{reaction}$ of stabilization did not change with the addition of CNT. The presence of CNT reduced the E_a of cyclization by up to 18% but increased the E_a of oxidation by up to 80%, as compared to PAN fiber. At 250 °C, core-sheath PAN-PAN/CNT fibers were fully stabilized in less than 2 hours, while the PAN fibers with the comparable fiber diameter required about 6 hours. PAN/CNT

showed porous structures on the fiber surface before stabilization, and a 3-D porous structure was observed after stabilization for PAN/CNT. The porous structure formed during stabilization can increase the O₂ diffusion and hence increase the rate of the stabilization reaction.

CHAPTER 5. CONTINUOUS STABILIZATION OF POLYACRYLONITRILE (PAN) - CARBON NANOTUBE (CNT) FIBERS BY JOULE HEATING

5.1 Introduction

. A Joule heating process has been shown to have the potential to replace convective heating for PAN stabilization by incorporating carbon nanotubes in the fiber to produce the required fiber conductivity for resistive heating. Currently, a convective heating process between 200 and 300 °C is typically used for PAN stabilization. The process is energy intensive with a long stabilization time of 1-2 hours. One way to reduce energy consumption is to optimize the current stabilization setup using (1) a highly efficient furnace, (2) improved heat transfer and process control, and (3) waste heat recovery systems [166]. The Joule heating process, on the other hand, can potentially reduce the energy cost and time of PAN stabilization through directly heating the fibers by electric current and can potentially replace the current convective heating-based stabilization. In this chapter, we demonstrate the effectiveness of continuous stabilization of PAN fibers by Joule heating for the first time, at an overall CNT concentration of 4 to 7 wt%, through a combination of experiment and modeling.

5.2 Experimental procedures

5.2.1 Materials

Polyacrylonitrile-co-methacrylic acid (PAN) with viscosity average molecular weight (M_v) 247,000, 500,000, and 964,000 g/mol, and 4 wt% copolymer methacrylic acid were obtained from Japan Exlan Co. and dried at 75 °C in a vacuum oven overnight before making a solution. Multi-wall carbon nanotubes (MWNT), SMW200 were purchased from SouthWest NanoTechnologies, Inc. (SWeNT), Norman, Oklahoma, with a length of 3-6 μm . For the MWNT, an average number of 9-10 walls and an average diameter of 12 ± 3 nm were determined by X-ray diffraction and SEM analysis, respectively, in the previous study[167]. Dimethylformamide (DMF) was obtained from Sigma Aldrich (HPLC grade, >99.9% purity). Methanol (ACS grade) was purchased from VMR International.

5.2.2 *Solution preparation*

For PAN/CNT solution, CNT powder was first homogenized in DMF at a concentration between 120 – 200 mg/dL using a homogenizer (T25 ULTRA-TURRAX, IKA) at 10,000 rpm for 30 minutes. The slurry was then bath-sonicated for 24 hours (Branson 8510). CNT/DMF dispersion was poured into the reactors containing PAN solution, which dissolved at 75°C while stirring. The excess solvent from the CNT dispersion was evaporated under a vacuum. CNT dispersion addition was continued until the desired quantity of CNTs was achieved (7 or 10 wt % with respect to the weight of polymer + CNT). For bi-component fiber spinning, two separate solution preparations were carried out, one for the sheath and the other for the core. PAN/CNT solution (10 wt% CNT and 90 wt% PAN) was used as the sheath component, and a PAN solution dissolved in DMF at 75°C was used as the core component during bi-component fiber spinning. Details of CNT dispersion and solution preparation are summarized in Table E1.

5.2.3 *Precursor fiber manufacturing*

PAN/CNT composite fibers were spun using a multi-filament fiber spinning unit (Hills Inc., FL), with a 40-hole spinneret, and the capillary diameter was 200 μm [12]. Single-component PAN/CNT composites fibers with 7 wt% CNT, as well as bi-component fibers with sheath-core geometry, were produced. PAN/CNT solution (7 wt% CNT and 93 wt% PAN) was used to produce single-component PAN/CNT fiber. For bi-component fiber spinning, PAN and PAN/CNT (10 wt% CNT and 90 wt% PAN) solutions were poured in respective reservoirs to supply solutions to the core and the sheath geometries in the spin pack, respectively. The spin pack consisted of distribution plates to result in the sheath-core geometry. The sheath/core area ratio was controlled by changing the flow rate ratio of the core and sheath solutions. During both fiber spinning, the extrudate from the spinneret passed through a 19 mm air gap followed by a pure methanol bath at $-50\text{ }^{\circ}\text{C}$. Fiber drawing was carried out on a multi-stage drawing line, using a hot drawing process on heated godet rollers. The spun draw ratio (SDR), as well as the post-spin draw ratio (PDR) from the stretching on the drawing line, are reported in Table 5.1.

5.2.4 *Fiber characterization*

The tensile properties of the fibers were measured using Favimat+ at 25.4 mm gauge length and 1 %/s strain rate on at least 30 fibers. Wide-angle X-ray diffraction (WAXD) measurements were conducted using Rigaku Micromax-002 (operating voltage and current 45 kV and 0.50 mA) using $\text{CuK}\alpha$ ($\lambda = 0.1542\text{ nm}$). Diffraction patterns were analyzed by Area Max (Version 2) and MDI Jade (Version 9). Crystal size was calculated from the equatorial scan using the Scherrer equation ($K=0.9$). Herman's orientation factor

was calculated from the azimuthal scan of PAN crystalline planes ((200) and (010) at $2\theta = 17^\circ$) following the previously described method[125,126]. Fiber cross-sections (bi-component fibers) were observed using an optical microscope (Leica DM2500 P). The fiber bundle was embedded into epoxy resin and microtomed (Leica, RM2255) in 7-10 μm thick sections before imaging under an optical microscope. Raman spectra were collected on a single fiber with a 785 nm laser on a Raman microscope system from HORIBA Scientific (XploRA ONE with a 785 nm laser). The orientation of the CNTs in the composite fibers was determined using a rotation stage with fiber axis rotated in 10° increments from 0 to 90° under parallel (VV, vertical/vertical) polarizers following reported methods elsewhere [11,127,128]. Fiber annealing was conducted at a constant length in an oven before measuring electrical conductivity. The electrical conductivity of a fiber bundle (40-filaments) was measured using Keithley 2400 source meter using a two-point probe geometry with a distance of 10 mm between the two probes. The silver paste was applied at the test points on the fibers to ensure low contact resistance between the probes and fibers. Electrical conductivity was calculated from the measured electrical resistance and geometry of fibers. Fourier transform infrared spectroscopy (FTIR) spectra were collected on a Spectrum One spectrometer (PerkinElmer Inc) from 4000 to 400 cm^{-1} at a resolution of 4 cm^{-1} . The precursor and stabilized fiber samples were ground with KBr and pressed into a pellet for measurements. Differential scanning calorimetry (TA Instrument Q200) was performed under air environments at a heating rate of $10^\circ\text{C}/\text{min}$ from 30°C to 400°C .

5.2.5 *Joule heating and convective heating*

Figure 5.1 shows the continuous resistive stabilizer (CoRe-Stab) for Joule heating. Fiber tow was unwound from a supply spool to the inlet tension servo and conducting roller to apply electric potential (voltage) while maintaining tension. The fiber tow then went through a quartz tube (2 meters long, 25.4 mm outer diameter, 2.54 mm thickness) to another conducting roller and was finally collected on an uptake spool. The tension, applied voltage, and residence time were controlled, and the temperature was monitored with an IR sensor in the middle and another one near the quartz tube end near the uptake spool. The air was supplied by an air fan continuously during Joule heating. Joule heating was conducted on a 200-filament bundle for single-component fibers and on 1000 and 6000-filament bundles for bi-component fibers. The picture of the 6000-filament bundle is shown in Figure E1. For fibers undergoing Joule heating, about 250 °C was measured constantly with the IR sensor located at the center of the quartz tube near the fiber bundle. The Joule heating parameters, including fiber speed, current, and heating time, are summarized in Table E2 and Table E3 in Supporting Information. For comparison, single and bi-component fibers were also stabilized under tension at 250 °C in a convection oven (VWR vacuum oven) for various times while continuously pumping air.

Inset in Figure 5.1 shows the schematic of the Joule heating process. The electric current generates heat upon passing through the resistance elements, CNT, in the PAN/CNT fibers. Continuous airflow supplies oxygen for oxidation reaction while at the same time, removes heat from the quartz tube. Heat loss also takes place through the wall of the quartz tube to the environment.

A generalized macroscopic heat transfer equation has been used to analyze the Joule heating process, including the air and fiber within the quartz tube:

$$-\Delta\dot{H}_{air} + Q_{tube} + Q_{rxn} + Q_{JH} = \frac{dE_{sys}}{dt} \quad (5-2)$$

$$E_{sys} = E_{fiber} + E_{tube} + E_{air}$$

Where $\Delta\dot{H}_{air}$, Q_{tube} , Q_{rxn} , Q_{JH} , $\frac{dE_{sys}}{dt}$ are the enthalpy change of continuous airflow, the heat loss through the quartz tube to the outside environment, the heat generated by stabilization reaction, the heat generated by Joule heating, and heat accumulation rate of the whole system during Joule heating, respectively. The heat accumulation of the whole system (E_{sys}) during Joule heating includes the heat accumulation of fiber (E_{fiber}), tube (E_{tube}), and air inside the tube (E_{air}). The detailed analysis of Joule heating is shown in the supporting information.

The heat generated per unit volume by the Joule heating process is calculated by:

$$Q_{JH} = \frac{i^2}{\sigma} \quad (5-2)$$

where i , σ , I , V , t are the current density, the electrical conductivity of the fibers, measured current value by source meter, applied voltage, and time, respectively. Current density can be further related to the voltage drop V over a length L by $i = \sigma \frac{V}{L}$.

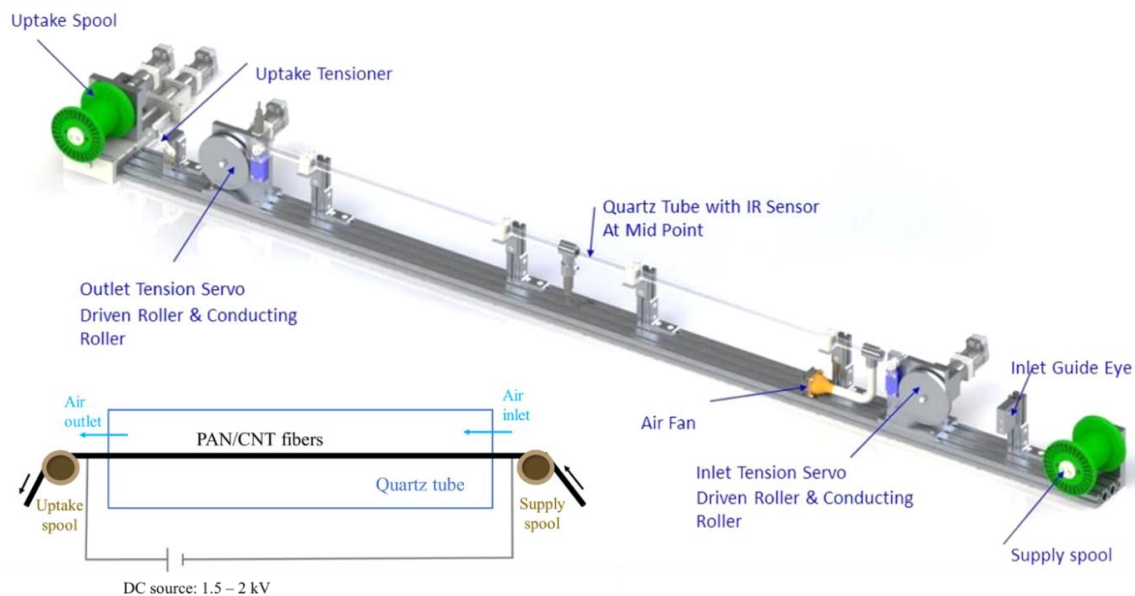


Figure 5.1. Continuous resistive stabilizer (CoRe-Stab) for Joule heating. Inset shows the Joule heating schematic. This equipment was designed and built by Vuronyx Inc.

5.3 Results and discussion

Figure 5.2 shows the cross-sections of single and bi-component fibers fabricated in this work. Core-sheath bi-component cross-section geometry was utilized in fiber design to reduce the overall amount of CNT in the fiber by incorporating 10 wt% CNT only in the sheath. Table 5.1 summarizes the draw ratio, diameters, and electrical conductivity of single and bi-component fibers. Bi-component fibers possessed over 2 orders of magnitudes higher electrical conductivity than single-component fibers before annealing. Bi-component fiber has a higher CNT concentration (10 wt%) in the sheath than single-component fibers (7 wt%), which is responsible for the increased electron transfer. Moreover, single-component fibers show higher anisotropy of CNT ($f_{\text{CNT}} = 0.35$) than bi-component fibers ($f_{\text{CNT}} = 0.06$). Increased anisotropy of CNT can disrupt the CNT percolation and lead to low electrical conductivity [29]. An annealing process has been

used to enhance the electrical conductivity of PAN/CNT fibers previously [34,96]. Annealing above the polymer glass transition temperature enables increased mobility of polymer chains, rearrangement of nanotubes, and thus leads to increased CNT contacts and hence increases electrical conductivity. Fibers were annealed at various conditions to increase electrical conductivity. The electrical conductivity of PAN/CNT fibers with different annealing conditions is summarized in Table E4. Before Joule heating, 30 minutes of annealing was used for single-component fiber, and 10 minutes of annealing was used for the bi-component fiber. Both single and bi-component fibers exhibited good electrical conductivity of 11.5 and 7.1 S/m after annealing, respectively. The electrical conductivity achieved after annealing for both fibers is also higher than that of PAN/CNT fibers with 15 wt% CNT (4.8 S/m), which was used in previous study to demonstrate Joule heating [96]. Tensile properties and structural parameters are summarized in Table E5. Both single-component and bi-component fibers show good tensile modulus values of 9.7 and 7.6 GPa, respectively.

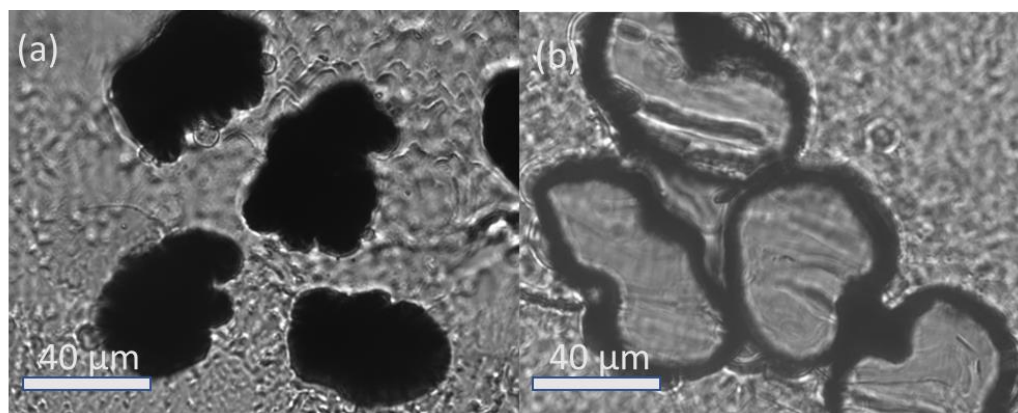


Figure 5.2. Optical micrographs of fiber cross-sections of (a) single-component and (b) bi-component core-sheath geometry fibers.

WAXD was used to study the structural change during the stabilization. Figure 5.3 shows the WAXD results of single-component fibers before and after annealing, after Joule heating, and after convective heating at different times. The disappearance of the PAN crystal peak at $2\theta \sim 17^\circ$ and the appearance of the peak at $2\theta \sim 26^\circ$ indicates the stabilized structure of PAN [96,150–152]. The PAN crystal peak at $2\theta \sim 17^\circ$ completely disappeared after the 1-hour Joule heating, which indicated that the Joule heating completely stabilized the 200-filament, 33 μm diameter fiber tows in less than 1 hour (Figure 5.3 (d)). On the other hand, the tow of the same fiber was not fully stabilized (Figure 5.3 (g)) after 2-hours in a 250 $^\circ\text{C}$ convection oven, as the $2\theta \sim 17^\circ$ peak remained in the WAXD integrated scan. Figure 5.3 (g) and (h) showed that the 33 μm diameter fiber bundle was fully stabilized between 2 hours and 2.5 hours of convective heating, when the WAXD peak at $2\theta \sim 17^\circ$ completely disappeared. A peak at $2\theta \sim 12^\circ$ was also observed in Figure 5.3. This peak was due to the spin finish applied after fiber spinning but before the hot drawing process. This has been further confirmed from the results in Figure E2.

Longer time was used to stabilize bi-component fibers than single-component fibers, by both Joule heating (2 and 4 hours) and by convective heating (2 to 12 hours), as the diameter of bi-component fibers (52 μm) is larger than that of single-component fibers (33 μm). Fibers with large diameters require a long time for oxygen to diffuse from outside to the fiber center, as the stabilization reaction can be limited by oxygen diffusion [168–170]. This is also confirmed by the DSC data (Figure E3). The heat released during stabilization of single-component fibers (2980 J/g, Figure E3) in the air was about 2.5 times that of the bi-component fiber in the air (1194 J/g). The heat of the exothermic reaction is related to the surface area to volume ratio (SA: V) [72]. SA: V ratio is inversely proportional to the fiber diameter, and a higher SA: V ratio with smaller fiber diameter leads to a higher diffusion rate of oxygen per unit mass and hence higher heat of stabilization reaction at the given time.

Table 5.1. Listing of CNT amount, draw ratio, diameter, and electrical conductivity for the fibers used in this study.

Sample	CNT wt%	SDR ⁺	PDR ⁺	Diameter* (μm)	Electrical conductivity (S/m)	
					Before annealing	After annealing**
Single-component	7	1	1.2	33 \pm 2	10 ⁻³	11.5 \pm 3.1
Bi-component	4.6	1	1.1	52 \pm 2	1.1 \pm 0.6	7.1 \pm 0.7

+SDR: Spun draw ratio, PDR: post-draw ratio. *Diameter: Equivalent diameter based on fiber cross-section area. **30 minutes of annealing for single-component fibers and 10 minutes of annealing for bi-component fibers was done at 210°C.

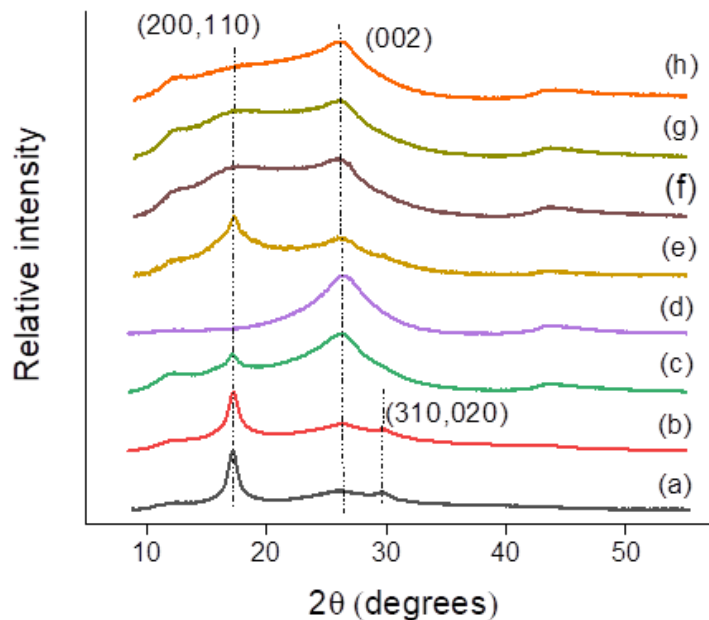


Figure 5.3. Integrated WAXD radial scans of single-component fibers. (a) before annealing, (b) after continuous annealing at 210 °C for 30-minutes, (c) after Joule heating for 30 minutes, (d) after Joule heating for 60 minutes. WAXD radial scans (e, f, g, h) after stabilization in the oven at 250 °C for varying times are given for comparison. Stabilization times in oven are: (e) 30 minutes, (f) 60 minutes, (g) 120 minutes, and (h) 150 minutes.

Figure 5.4 shows the integrated WAXD scans of bi-component fibers before and after annealing, after Joule heating, and after convective heating at different times. The $I_{17^\circ}/I_{26^\circ}$ ratio (ratio of peak intensity) are listed in the same figure to show the structural change of PAN during stabilization. Figure 5.4 (e) – (h) show the structural development of PAN during stabilization with increased time of convective heating. The $I_{17^\circ}/I_{26^\circ}$ ratio was about 1.1 after 2-hours of convective heating, and this ratio decreased to 0.5 after 12-hours of convective heating. Figure 5.4 (c) and (d) showed the integrated scan of PAN after 2 hours and 4 hours Joule heating, respectively, over which the $I_{17^\circ}/I_{26^\circ}$ ratios were 0.7 and 0.5, respectively. Instead of 12 hours for the convective heating process, Joule heating only

needs 4 hours to stabilize the same composites fibers. The required stabilization time through Joule heating can be reduced significantly to 1 hour or less with reduced fiber diameter ($\sim 33 \mu\text{m}$). For the commercial PAN fiber with a diameter of $10 - 15 \mu\text{m}$, the stabilization time via Joule heating is expected to be significantly below 1 hour [81].

FTIR scans on bi-component fibers are given in Figure 5.5. FTIR spectra of bi-component fibers. (a) before Joule heating, (b) after 2-hour Joule heating using 6000 filaments tow, (c) after 4 hours Joule heating using 1000 filaments tow, and (d) after 4-hour stabilization in a $250 \text{ }^\circ\text{C}$ convection oven in the air using 1000 filaments tow.. The $2180 - 2260 \text{ cm}^{-1}$ peak is due to the nitrile group[96,150,151]. Un-reacted nitrile ($\sim 2243 \text{ cm}^{-1}$) is shown for bi-component precursor fiber. Two new peaks at 2239 cm^{-1} and 2219 cm^{-1} were shown for fibers after a 4-hours stabilization process at $250 \text{ }^\circ\text{C}$ in the oven (Figure 5.5. FTIR spectra of bi-component fibers. (a) before Joule heating, (b) after 2-hour Joule heating using 6000 filaments tow, (c) after 4 hours Joule heating using 1000 filaments tow, and (d) after 4-hour stabilization in a $250 \text{ }^\circ\text{C}$ convection oven in the air using 1000 filaments tow. (d)), which indicated the part of the unreacted nitrile group shifted to conjugated nitrile at $\sim 2210 \text{ cm}^{-1}$, and the β -amino nitrile at $\sim 2190 \text{ cm}^{-1}$ during cyclization reaction [152]. On the other hand, the nitrile peak disappeared after the Joule heating for 2 or 4-hours (Figure 5.5. FTIR spectra of bi-component fibers. (a) before Joule heating, (b) after 2-hour Joule heating using 6000 filaments tow, (c) after 4 hours Joule heating using 1000 filaments tow, and (d) after 4-hour stabilization in a $250 \text{ }^\circ\text{C}$ convection oven in the air using 1000 filaments tow. (b) and (c)), indicating that the nitrile group underwent the cyclization reaction completely. Corresponding peaks of C=N and C=C bonds appeared at

$\sim 1600 \text{ cm}^{-1}$ [12,22]. This result confirms that Joule heating requires a shorter time to form cyclized PAN structures as compared to convective heating.

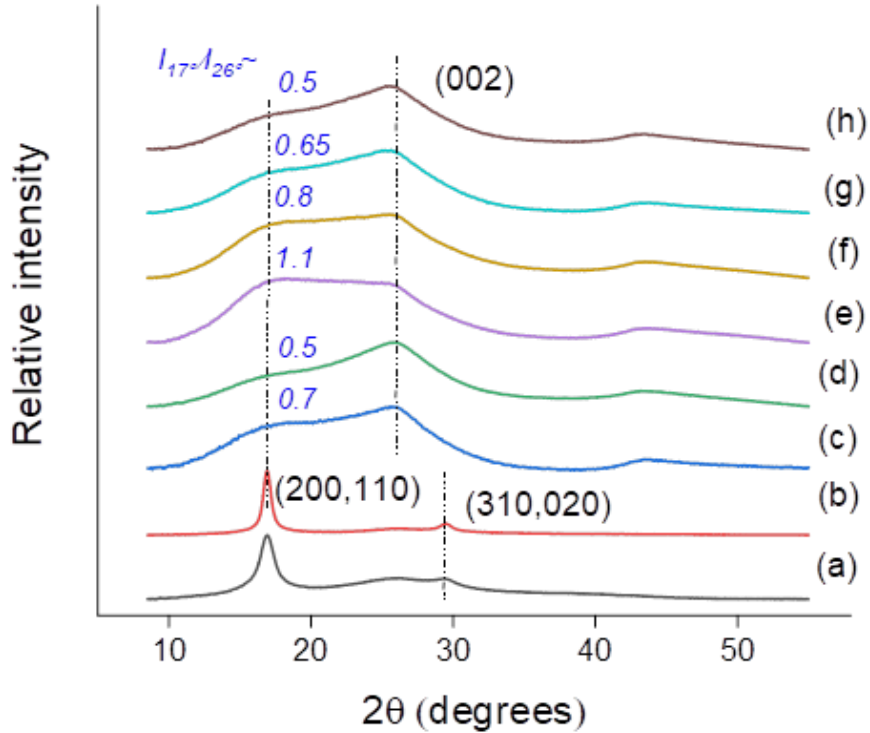


Figure 5.4. Integrated WAXD radial scans of bi-component fibers. (a) before annealing, (b) after continuous annealing at 210 °C for 10 minutes, (c) after Joule heating of 6000 filaments tow for 2 hours, (d) after Joule heating of 1000 filaments tow for 4 hours. WAXD radial scans (e, f, g, h) of 1000 filaments tow after stabilization in the oven at 250 °C for varying times are given for comparison. Stabilization times in the oven are (e) 2 hours, (f) 4 hours, (g) 8 hours, and (h) 12 hours.

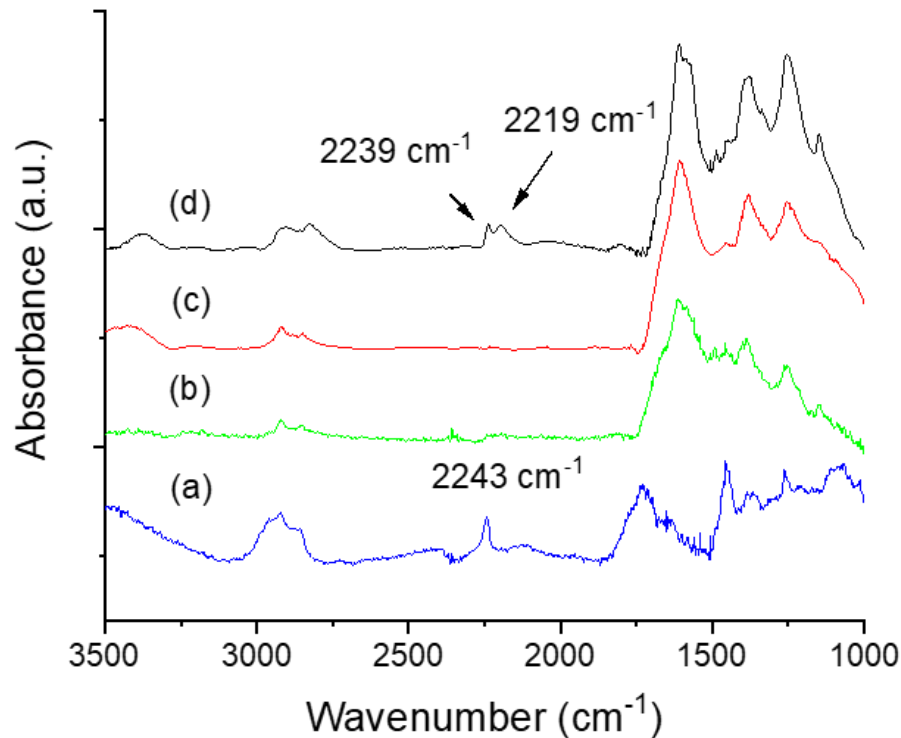


Figure 5.5. FTIR spectra of bi-component fibers. (a) before Joule heating, (b) after 2-hour Joule heating using 6000 filaments tow, (c) after 4 hours Joule heating using 1000 filaments tow, and (d) after 4-hour stabilization in a 250 °C convection oven in the air using 1000 filaments tow.

Figure 5.6 shows the distribution of energy consumed during Joule heating according to equation (5-1). The detailed calculation is shown in the supporting information. Only about 0.1% of the energy generated during Joule heating for the single component fiber and about 0.3% for the bi-component fiber were used to increase the fiber temperature and to increase the kinetic of PAN stabilization reaction. About 16.2 % and 83.7 % of the energy generated by Joule heating and the exothermic reaction were lost through heating the continuously flowing air and through the quartz tube to the outside environment. For bi-component fibers, about 6.9 % and 92.8% of the energy was lost

heating the air and to the environment through the tube during the Joule heating process. The overall energy consumed for 4-hour Joule heating for bi-component fibers was estimated at about 83 kBtu/lb (Figure 5.7, calculation shown in the supporting information). The current typical energy consumption of stabilization and carbonization is about 84 kBtu/lb of carbon fiber, according to a report from the U.S. Department of energy [166], and 65% (55 kBtu/lb) was assumed to be used during the stabilization [171]. The estimated energy consumption (63 kBtu/lb) of the current Joule heating process is about 50% higher than the current energy used in a convective heating process. However, the Joule heating process can be further optimized with the addition of a thermal insulation layer, recovery of the wasted heat, and with reduced voltage. When assuming no energy loss to the environment with the addition of thermal insulation layer and optimized voltage, the energy consumption is expected to be reduced from 83 to 6 kBtu/lb of fiber or lower (Figure 5.6 & Figure 5.7). Furthermore, the minimum energy needed for stabilization through Joule heating only includes the energy to heat up the fiber in order to initiate the stabilization reaction (E_{fiber}). The value is as low as 0.2 kBtu/lb of carbon fiber (Figure 5.7).

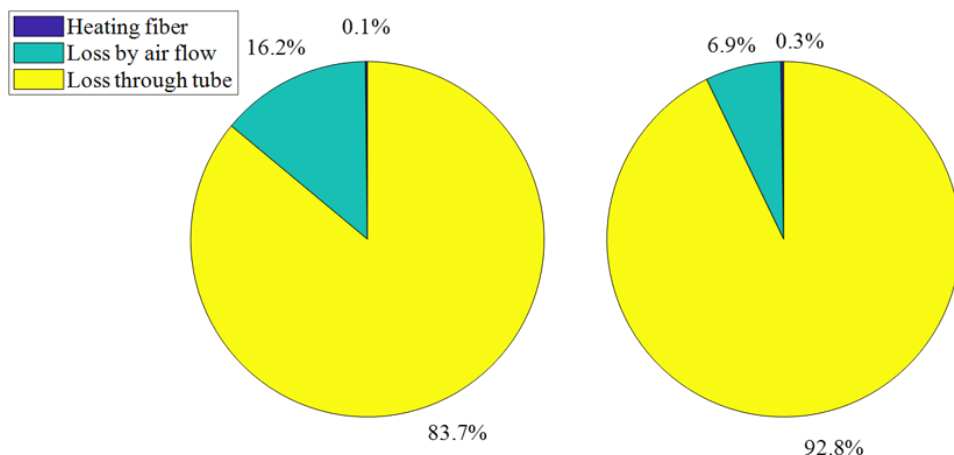


Figure 5.6. Distribution of energy consumed during Joule heating according to equation 5-1 of (left) single-component fibers for 1 hour Joule heating with 200 filaments tow, and (right) bi-component fibers during for 4 hours Joule heating with 1000 filaments tow.

Two challenges remain in order to translate the Joule heating technique to practical industrial manufacturing. One challenge is to design PAN-based precursor fiber that is electrically conductive ($\sigma \sim 1-10$ S/m). The current process utilized PAN filled with 4-7 wt% CNT. The single-component and bi-component core-sheath geometries were used for precursor design. To further reduce the CNT wt% requires further study and optimization of PAN/CNT (or other conductive fillers) blends as well as the design of fiber structure. Secondly, reducing the fiber diameter can reduce the stabilization time. The further research effort is needed to reduce the precursor fiber diameter from 30-50 μm to about 10-15 μm while achieving the necessary electrical conductivity (~ 1 to 10 S/m) of the precursor fibers. Improving energy efficiency during the Joule heating process is another challenge for this technology. Optimization of applied voltage, the flow rate of air, and heat loss through the reactor are the keys to achieve high energy efficiency. Adding a thermal insulation layer and recovering heat loss is useful for optimizing this process

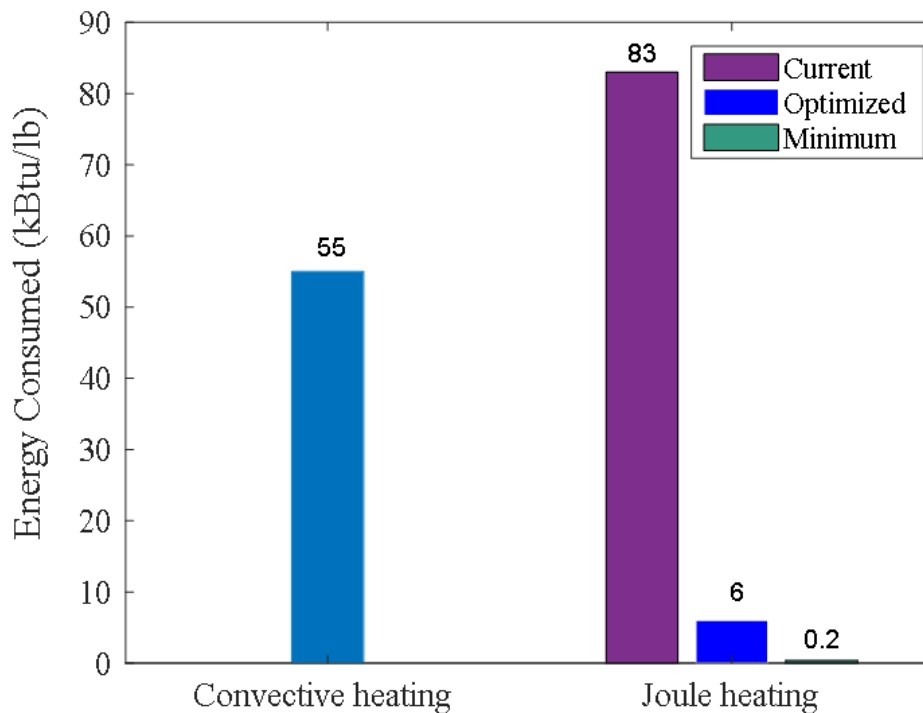


Figure 5.7. Energy consumption for convective heating[166,171], and for Joule heating from equation 5-1. Joule heating values are for bi-component fibers for 4 hours for 1000 filament tow. The optimized value is calculated assuming that heat loss can be eliminated by insulation but that heat loss due to airflow inside the tube still occurs. The minimum value only includes the energy required to heat up the fibers to 250 °C for stabilization during Joule heating.

5.4 Conclusions

To summarize, in this work, we report the first continuous PAN fiber stabilization process based on Joule heating. Single-component PAN/CNT fibers with 7 wt% CNT and bi-component fibers with about 4.6 wt% CNT were manufactured through the gel spinning method. A continuous Joule heating process was used to stabilize single-component fibers with a 33 μm diameter, 200-filament tow, as well as bicomponent fibers with a 52 μm diameter, and tow with up to 6000-filament. Joule heating reduced the stabilization time of single-component fibers from about 2.5 hours through convective heating to less than 1

hour. Also, for bi-component fibers, Joule heating required less time to form a stabilized PAN structure compared with convective heating. The estimated energy consumption of the Joule heating process with the current experimental setup was higher than the energy consumed by the industry-standard convective heating process. However, adding thermal insulation and reducing voltage input while achieving the desired stabilization temperature can eliminate convective loss from the quartz surface and reduce energy consumed during Joule heating to a significantly lower value than convective heating. Furthermore, the minimum value of the energy needed for stabilization through Joule heating is estimated to be as low as 0.2 kBtu/lb of fiber produced, which accounts for less than 1 % of the energy consumed in stabilization during convective heating.

CHAPTER 6. CONCLUSION AND RECOMMENDATIONS

6.1 Conclusions

Here we report the processing, structure, properties, and Joule heating of PAN fibers with CNT filler. Rheological measurements were used to guide fiber spinning of PAN/CNT dispersions. Core-sheath PAN-PAN/CNT fibers were fabricated and used to stabilize PAN through the Joule heating process at 3.7 wt% CNT. The effect of CNT on stabilization of PAN was investigated on fabricated PAN/CNT fibers. A continuous, Joule heating-based stabilization process was also developed as part of the current study. The key results and conclusions of the study are summarized below.

PAN/CNT dispersions behaved more elastic-like with increasing CNT amount, as compared to the control PAN solutions. The Cox-Merz rule held for the pure PAN solutions and PAN/CNT dispersions at most concentrations, except for the most concentrated PAN/CNT-15 dispersions. The homogeneity of the solution or dispersion depended on the concentration of CNT, but not on the temperature between 0 and 60 °C. Decreasing the dispersion elasticity by using lower molecular weight polymer assisted a longer continuous jetting during fiber spinning, as compared to the PAN/CNT dispersion with higher molecular weight polymer. For PAN/CNT dispersions, rheological behavior provides a good indicator of fiber spinnability. The $\log G'$ versus $\log G''$ and $\tan \delta$ curves are useful to guide fiber spinning with a simple oscillation measurement.

A percolated CNT network at 10 wt% CNT in the sheath enhanced electrical conductivity as compared to the neat PAN fiber, while PAN polymer in the core

contributed to the good mechanical properties. Fibers with relatively thin sheath allowed overall CNT loading to be as low as 3.7 wt% to be made with good electrical conductivity. Low draw ratio (DR=3) fibers with 4.4 wt% CNT possessed a tensile strength of 299 MPa, and a tensile modulus of 12.7 GPa, as well as the electrical conductivity of up to 5 S/m. PAN stabilization by Joule heating was demonstrated in a batch process at an overall CNT concentration of 3.7 wt%.

The heat of stabilization of PAN/CNT fibers increased up to 3 times when compared to PAN fiber with a comparable diameter under an air atmosphere, while the heat of stabilization did not change with adding CNT under N₂ atmosphere. The addition of CNTs reduced the activation energy of PAN cyclization by up to 12% but increased it for the oxidation reaction by up to 80%, as compared to PAN fibers. CNTs did not increase the kinetic constant of the cyclization reaction but increased the kinetic constant of the oxidation reaction by up to 5 times when comparing to PAN fiber at 250 °C. At the same temperature, the bi-component PAN/CNT fiber bundle was fully stabilized in less than 2 hours, while the PAN fibers with comparable diameter took 6 hours to stabilize. Porosity was observed in the PAN/CNT precursor and the stabilized PAN/CNT fiber. This porosity was considered responsible for increased oxygen diffusion, and hence for reduced PAN stabilization time.

A continuous Joule heating process has been used for the first time to stabilize polyacrylonitrile (PAN) fibers containing carbon nanotubes (CNT). Single-component PAN/CNT fibers with 7 wt% CNT and bi-component fibers with about 4.6 wt% CNT were manufactured through the gel spinning method. The Joule heating was used to stabilize single-component fibers with a 33 μm diameter, 200-filament tow as well as bicomponent

fibers with a 52 μm diameter, and a tow containing up to 6000-filaments. Joule heating reduced the stabilization time of single-component fibers from about 2.5 hours through convective heating to less than 1 hour. Also, for bi-component fibers, Joule heating required less time to form a stabilized PAN structure compared with convective heating. A model of heat transfer and thermodynamics occurring during Joule heating was developed to understand the reduction in energy consumed in stabilization when compared to convective heating. The minimum energy needed for stabilization through Joule heating is estimated to be less than 1 % of the energy used through convective heating.

6.2 Recommendations

The current study demonstrated the stabilization of PAN through Joule heating at a low CNT filler content of 3.7 wt%. However, further optimization is recommended to further reduce energy consumption and material cost. This can be achieved through modifying the Joule heating setup and by optimizing filler content in the PAN fibers. Moreover, the studies on the rheological behavior of PAN/CNT dispersion and stabilization of PAN/CNT fibers also raised several interesting questions which require further investigation. The recommendations for each study are summarized below.

In Chapter 2, the $\log G'$ versus $\log G''$ and $\tan \delta$ curves are shown to be useful to guide fiber spinning of PAN/CNT with a simple oscillation measurement. Also, the $\log G'$ versus $\log G''$ and $\tan \delta$ curves of PAN/CNC showed similarities with those of PAN/CNT at high filler loading. However, this study does not answer the question, if the empirical findings presented here can be useful for other polymer/nanofiller composites (e.g., composites with cellulose nanomaterial, carbon black, and graphene oxide), especially at

high filler loading? A further systematic study is recommended to explore the generality of the empirical finding of using the $\log G'$ versus $\log G''$ and $\tan \delta$ curves to guide processing of polymer/nanofiller composites with different polymers and fillers.

In Chapter 3, it was demonstrated that PAN/CNT fibers with the core-sheath structure could possess combined good electrical and tensile properties at a low CNT loading. And the Joule heating was demonstrated to stabilize core-sheath fibers at a 3.7 wt% overall CNT. The overall CNT wt% may be further reduced by optimizing the core-sheath area ratio during fiber fabrication. Moreover, a further optimization process is recommended to find the optimum draw ratio to achieve the desired electrical conductivity. Lastly, a cheaper conductive filler such as carbon black and graphite can be used along with CNT to make the core-sheath fibers more cost effective.

In Chapter 4, the porous PAN/CNT structure was believed to increase the O₂ diffusion and the stabilization rates of PAN significantly. The pores were shown on the surface of the fiber, and the stabilization promoted the formation of porous structure for PAN/CNT. The mechanism of formation of the porous structure of PAN/CNT needs further investigation. Also, can the porous structure arise with other cheap filler to increase the O₂ diffusion and stabilization rate of PAN? The mechanical properties of PAN/CNT fiber due to the porous structure can be another concern. A core-sheath structure may be useful since the solid core can contribute to good mechanical properties, and the porous sheath can lead to a reduced processing time and cost. Further optimization of core-sheath may be possible to achieve fibers with relatively good properties and reduced cost at the same time. Moreover, the stabilized PAN/CNT fibers with a porous structure can be further

carbonized to make carbon fiber with a high surface area, which may be useful in energy storage applications.

In Chapter 5, a continuous Joule heating process was demonstrated. However, during the Joule heating, most of the heat generated by the electric current was lost to the outside environment. The process needs further optimization, including reducing the voltage and current, adding an insulating layer to prevent heat loss to the outside environment, and recovery of the heat loss through the flowing air. Moreover, the heat transfer can be complicated during Joule heating. The current process used one IR sensor to monitor the temperature in the middle and one sensor at the end of the reactor. Measurement of the temperature profile of the fiber bundle and the reactor using an IR microscope or other advanced techniques is recommended. The detailed temperature profile may be useful to monitor the Joule heating for optimization.

APPENDIX A. A COMPREHENSIVE STUDY OF POLYACRYLONITRILE (PAN) IN VARIOUS SOLVENTS AND SOLVENT MIXTURES: GELATION BEHAVIOR, GEL SPINNING, AND HANSEN'S SOLUBILITY PARAMETER PREDICTIONS

A.1 Introduction

The gel spinning method was invented in the late 1970s in the Netherlands [5]. Ultra-high-molecular weight polyethylene (UHMWPE) ($M_w \sim 10^6$ g/mol) has been used to produce a polymer solution with a solvent such as decalin. The low solid content solution of UHMWPE contains few chain entanglements, and low entanglement density contributes to highly drawable fibers [5]. One significant work done in gel spinning is to successfully evaluate the solvent effect on gel spinning and fiber properties of UHMWPE [172]. It has been reported that employing “relatively poor (e.g., vegetable oil) -as opposed to-good solvents” (e.g., decalin and mineral oil) can lead to improved PE draw ratio. The author hypothesized that the additional drawability comes from more disentanglement induced by the fast crystallization process in poor solvents such as fatty oil, natural peanut oil, stearic acid, and decalin/dodecanol co-solvents [173]. The hypothesis was supported by the differential scanning calorimetry (DSC) study: poor solvents increased the gelation (crystallization) temperatures of PE than decalin. Besides, through the characterization of melt flow rate (MFR), the solution from poor solvents possessed higher MFR than decalin. In addition, the reduced solution viscosity would help with the gel spinning process.

The current study on PAN in co-solvents systems is inspired by studies on UHMWPE. Co-solvents systems have been studied with PAN dissolved in DMSO and non-solvent water or ethanol [13–21]. However, the non-solvent effect on the tensile properties of resulting fibers remains unclear. In the current study, rheological measurements are used for understanding the gelation behavior of PAN dissolved in DMF, DMF/water, and DMF/toluene. And such solutions with non-solvent water were also used for gel spinning to evaluate the water effect on gel spun fiber tensile properties. Moreover, Hansen’s solubility parameters are introduced to assess the solvent and solvent mixtures: 1) solubility parameter R_a is correlated to the T_{gel} of PAN solutions made with solvent mixtures including DMF, water, and toluene; 2) solubility parameters are used as a guidance to select new solvents and solvent mixtures for fiber spinning of PAN.

A.2 Experimental procedures

Polyacrylonitrile-co-methacrylic acid (4 wt% copolymer) with viscosity average molecular weight (M_v)= 500,000 g/mol was obtained from Japan Exlan Co., Japan. Dimethylformamide (DMF, HPLC grade, >99.9% purity), sulfolane (99% purity), toluene (99.8% purity) were obtained from Sigma-Aldrich. Propylene carbonate (PC, 99.5% purity) was purchased from Thermo Fisher Scientific.

PAN/DMF, PAN/DMF/water (4 and 7 vol% water), and PAN/DMF/toluene solutions were prepared by dissolving PAN powder in the corresponding solvents or solvent mixtures at 75 °C with continuous stirring. PAN/sulfolane, PAN/sulfolane/PC, PAN/sulfolane/toluene, PAN/PC were dissolved between 90 and 100 °C. The dissolved

solutions were deaerated in a vacuum oven at 60 °C before rheology measurement and gel spinning. The details of solution preparation are shown in Table A1.

Gelation behavior was characterized by a Rheometer (Anton Paar) with a cone-and-plate geometry, a 50-mm plate on top, and a Peltier plate on the bottom. An evaporation blocker was used to prevent solvent evaporation and to reduce air disturbance during measurements [107]. The linear regime was determined initially by dynamic strain test (0.01– 10 %). 1% strain, which was in the linear viscoelastic regime for all solutions, was chosen for all solutions. Dynamic frequency sweep was used from 0.5 rad/s to 100 rad/s to determine polymer response to frequency change during the oscillation test. To find the gelation temperature, the frequency sweep was first conducted at 20 °C, then at lower temperatures (down to -28 °C). Before each test at each temperature, all samples were kept for at least 5 min at the desired temperature to ensure the thermal equilibrium and to eliminate the thermal history effect. To study the effect of high temperature on the rheological behavior of PAN solution, a new solution sample was used to conduct the same frequency sweep in the elevated temperature ranges (30, 40, 50 °C).

PAN solutions were spun between 40 - 80 °C using a spinning unit manufactured by Hills, Inc., and a single hole spinneret of 200 μm diameter. The solution was quenched into the coagulation bath of methanol, water, acetone, or their mixtures at the temperature range between -50 and 18 °C, with an air gap of 6 cm, The details of fiber spinning are summarized in Table A1. A two-stage drawing process was utilized. The as-spun fibers were firstly drawn at room temperature, followed by a hot drawing process through a glycerol bath maintained at about 165 °C.

Tensile testing was performed with a gauge length of 25.4 mm at a strain rate of 1%/s using a FAVIMAT⁺ tensile testing instrument. For each fiber sample, at least 30 filaments were tested. Wide-angle X-ray diffraction patterns of PAN fiber (WAXD) were measured by a Rigaku MicroMax 002 X-ray generator using CuK α ($\lambda = 0.1542$ nm). The WAXD curves were fitted with an MDI Jade (Version 9) software. Crystal size was calculated from the equatorial scan data using Scherrer equation ($K=0.9$). Herman's orientation factor was calculated from the azimuthal scan of PAN crystalline planes ((200) and (010) at $2\theta \sim 17^\circ$ following the previously described method [125,126].

Table A1. Solution preparation and fiber spinning conditions of PAN in various solvents and solvent mixtures.

Solvent #1	Solvent #2	Solvent #2 vol%	Solid (g/dL)	Dissolving temperature (°C)	Spinneret temperature (°C)	Coagulation bath	Coagulation bath temperature (°C)
DMF	None	N/A	10.5	75	80	Methanol	-50
DMF	water	4	10.5	75	80	Methanol	-50
DMF	water	7	10.5	75	80	Methanol	-50
DMF	PC	35	10.5	75	80	Methanol	-50
DMF	PC	10	10.5	75	80	Methanol	-50
DMF	Toluene	20	10.5	75	80	Methanol	-50
						Water, acetone,	
Sulfolane	None	N/A	8	95	40-50	methanol and their mixtures*	-50 -18
Sulfolane	PC	25	8	90	40-50	methanol	0 - 10
Sulfolane	PC	50	8-8.5	90	40-50	methanol	-15
PC ⁺	None	N/A	8	90	N/A	N/A	N/A
Sulfolane ⁺	Toluene	10	8	100	N/A	N/A	N/A

*Details are shown in Table A8. No fiber spinning is conducted for PC and Sulfolane/Toluene.

A.3 Results and discussion

Gelation behavior was studied for four solutions with the same solid content (10.5 g/dL) made with different water or toluene volume percentage in the solvent. Figure A1 shows the complex viscosity (η^*) versus frequency (ω) of various PAN solutions dissolved

in DMF with water or toluene. For PAN/DMF, η^* showed a clear transition between -20 and -25°C. η^* increased about 1 order of magnitude at low frequencies (< 1 rad/s) at -25°C, as compared to its value at -20°C. Moreover, η^* showed a power-law shear thinning at all frequencies at -25°C. According to Winter [174], the start-up of the complex viscosity that follows a power law can be used to identify the gelation behavior. Based on these observations, the gelation temperature (T_{gel}) for the PAN/DMF solution was determined to be between -20 and -25°C. For PAN dissolved in DMF with 4 and 7 vol% water, gelation was found between -5 to 0 °C, and 0 and 5 °C, respectively. These results are consistent with the findings of the gelation behavior of the PAN/DMSO/water system [13–18]. An elevated gel temperature up to 15°C was also observed upon the addition of water (0-8 wt%) into DMSO [14,16,17]. The T_{gel} of PAN solution is also highly dependent on the solid of PAN. For example, at 20wt% solid of $M_v = 7.8 \times 10^4$ g/mol, PAN/DMSO solution showed a T_{gel} of 46 °C; at 23 wt% of solid with the same PAN polymer, T_{gel} of PAN/DMSO was about 53°C [17]. Moreover, instead of the rapid jump of η^* for PAN/DMF between -20 and -25°C, η^* of PAN in DMF with water gradually increased at decreasing temperature. To better understand the role of the co-solvent on the gelation behavior of PAN solution, besides the polar solvent water, 7 vol % non-polar solvent toluene was also added into DMF to dissolve PAN. Interestingly, for PAN/DMF/ toluene, η^* showed the gelation between -28 and -25°C, which was slightly lower than that for PAN/DMF. Toluene is a non-solvent with a lower melting point (-95 °C) than DMF (-61 °C) and water (0°C). The results suggest the T_g of the PAN solution can be correlated to solvent properties (i.e., the intermolecular interaction between molecules in the solvent). After T_{gel} , η^* showed a steep shear-thinning, which can be fit by a power-law equation (η^*

$\sim \omega^n$, where n is the power-law scaling factor and shown in Figure A1). A slope (n) = -1 is expected from a solid [174]. PAN/DMF showed a higher n value after T_{gel} than solvent mixtures with water and toluene, which suggested more solid-like behavior after T_{gel} .

Besides finding the T_{gel} using the complex viscosity, some researchers also identified the temperature where $\tan \delta$ starts to be independent of frequency as T_{gel} [14–17]. Figure A2 summarizes the gelation process dependence on both frequency and temperature. Water addition raised the T_{gel} while toluene decreased T_{gel} for PAN solution dissolved in DMF, which were consistent with the T_{gel} results shown in Figure A1.

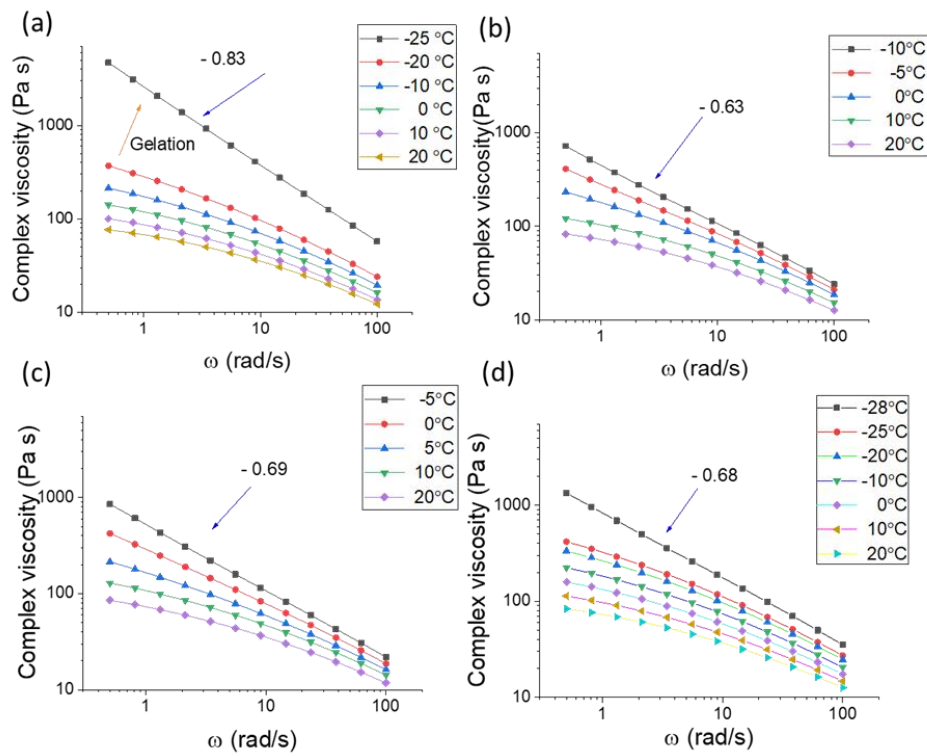


Figure A1. Complex viscosity (η^*) versus frequency (ω) at various temperatures. (a) PAN/DMF, (b) PAN/DMF/Water (with 4 vol % water); (c) PAN/DMF/Water (with 7 vol % water); (d) PAN/DMF/toluene (with 7 vol % toluene). The slopes of the η^* curves are shown in the figure.

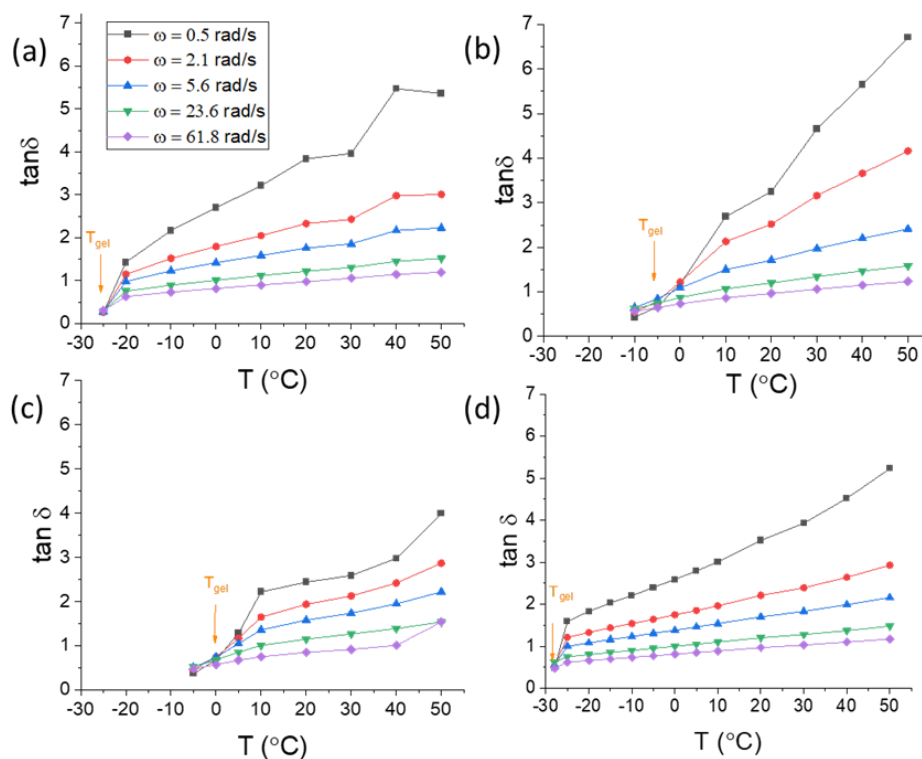


Figure A2. $\tan \delta$ as a function of temperature at various frequencies of PAN solution in DMF with water or toluene. (a) only DMF, with no water or toluene, (b) 4 vol % water, (c) 7 vol % water, (d) 7 vol % toluene.

Solution homogeneity was also studied using rheology tests. Figure A3 shows the $\log G'$ versus $\log G''$ curves at various temperatures. Polymer solution with an ideal homogeneity would give $\log G'$ versus $\log G''$ slope of 2 when ω is close to 0 [114–116]. Slopes of the $\log G'$ versus $\log G''$ plot of PAN/DMF solution remained almost the same from high temperature to the T_{gel} . At T_{gel} , the solution turned into a gel, and the slope decreased significantly from 1.48 to 0.7. While in solution with water, the slope of $\log G'$ versus $\log G''$ curve decreased continuously with decreasing temperature. The change of solution homogeneity for PAN /DMF/water can be different from the PAN/DMF solution due to the liquid-liquid phase separation. At reduced temperature, polymer chains can be

more concentrated into DMF solvent and less concentrated near non-solvent water. An inhomogeneous network can form and induce the gelation at low temperature. On the other hand, solvent mixture with 7 vol % toluene showed a similar behavior as PAN/DMF: the solution homogeneity remained the same until reaching the T_{gel} temperature (Figure A3 (d)).

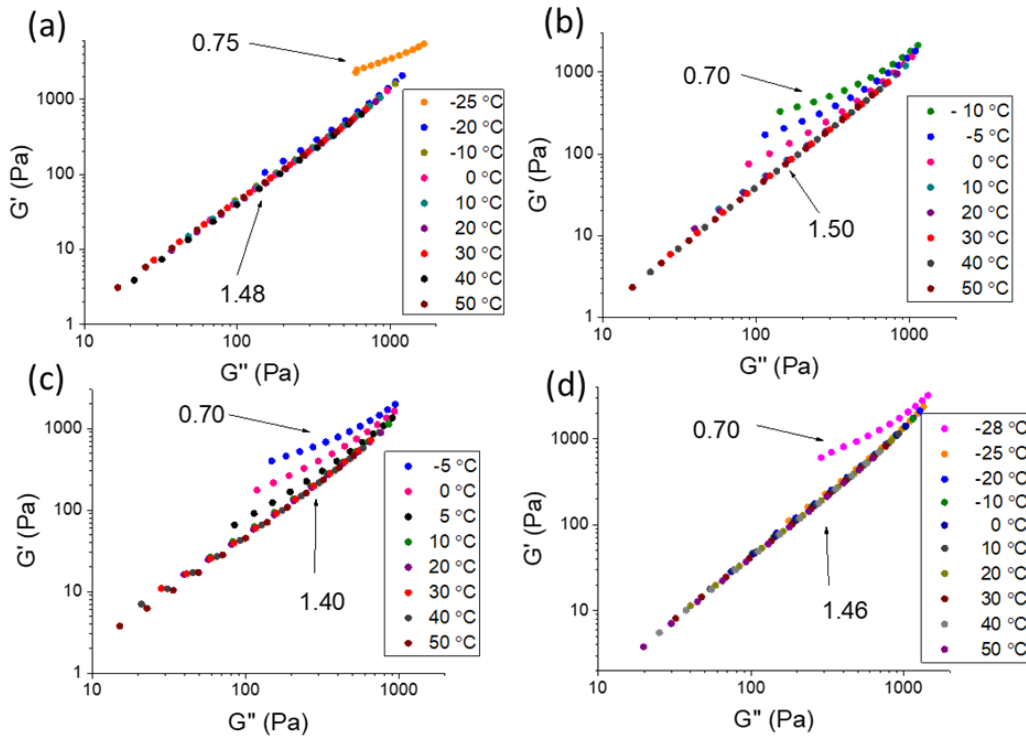


Figure A3. $\log G'$ versus $\log G''$ curves for PAN solution from 50 °C to gelation temperature in DMF with water or toluene. (a) only DMF, with no water or toluene, (b) 4 vol % water, (c) 7 vol % water, (d) 7 vol % toluene. The slopes of the curves are shown in the figure.

Hansen's solubility parameters (HSP) have been used for selecting solvents for polymers[175]. R_a , the Hansen's interaction parameter, is an indication of interaction distance between polymer and solvent and is calculated using *equation (A-2)*.

$$\delta^2 = \delta_d^2 + \delta_p^2 + \delta_h^2 \quad (\text{A-1})$$

$$R_a^2 = a(\delta_{d1} - \delta_{d2})^2 + b(\delta_{p1} - \delta_{p2})^2 + c(\delta_{h1} - \delta_{h2})^2 \quad (\text{A-2})$$

where $\delta, \delta_d, \delta_p, \delta_h$ are HSP for the total, dispersion, polar and hydrogen bonding interactions respectively, 1 and 2 refers to polymer and the solvent. $a = 4, b = c = 1$ from empirical results.

It has been previously reported that T_{gel} of PAN solution was related to Hansen's solubility parameter [18]. However, the author only considered the polarity of the solvent (δ_p). The dispersion parameter (δ_d) or hydrogen bonding (δ_h) were not fully considered. In this work, total interaction parameter δ is used to relate to T_{gel} . Table A2 and Figure A4 summarize the T_{gel} and change of slopes of $\log G'$ versus $\log G''$ curves for different solvent and solvent mixtures. On the one hand, the water content in DMF resulted in high δ value, high gelation temperature, and relatively high inhomogeneity of the solution. On the other hand, 7 vol % toluene in DMF decreased the δ , decreased gelation temperature, and the solution remained homogeneous above the gelation point. The T_{gel} results of PAN/DMSO/water were also included in Table A2 and Figure A4.

Table A2. Results of rheology study of solvent and solvent mixtures and relation to Hansen's solubility parameters.

Solvent	δ	δ_d	δ_p	δ_h	R_a	T_{gel} (°C)	Log G' versus log G'' plot slope from 50°C to gel point
DMF	24.9	17.4	13.7	11.3	8.9	-20	~1.48
DMF/water (96/4)	25.4	17.3	13.8	12.5	9.4	-5	decreased from 1.50 to 0.70
DMF/water (93/7)	25.9	17.3	13.9	13.5	9.9	0	decreased from 1.40 to 0.70
DMF/toluene (93/7)	24.1	17.4	12.8	10.6	8.7	-25	~1.46
DMSO*	26.7	18.4	16.4	10.2	7.1	46	N/A
DMSO/water (2 wt%)*	26.9	18.3	16.4	11.0	7.4	57	N/A
DMSO/water* (4 wt%)	27.2	18.3	16.4	11.8	7.7	62.5	N/A
DMSO/water* (6 wt%)	27.5	18.2	16.4	12.6	8.2	66	N/A
DMSO ⁺	26.7	18.4	16.4	10.2	7.1	7	N/A
DMSO/DMF ⁺ (15 wt%)	26.4	18.2	15.9	10.4	7.3	0	N/A
DMSO/DMF ⁺ (25 wt%)	26.1	18.1	15.6	10.5	7.5	-4.6	N/A

* T_g of PAN dissolved in DMSO and DMSO/water are from ref [14], with 20 wt% PAN copolymers (Acrylonitrile: Itaconic acid = 98:2) with $M_v = 7.8 \times 10^4$ g/mol.
⁺ T_g of PAN dissolved in DMSO and DMSO/DMF are from ref [18], with homo PAN of molecular weight of 150,000 g/mol. $\delta_d, \delta_p, \delta_h$ of solvent mixtures were calculated by rule of mixture of individual solvent based on volume %.

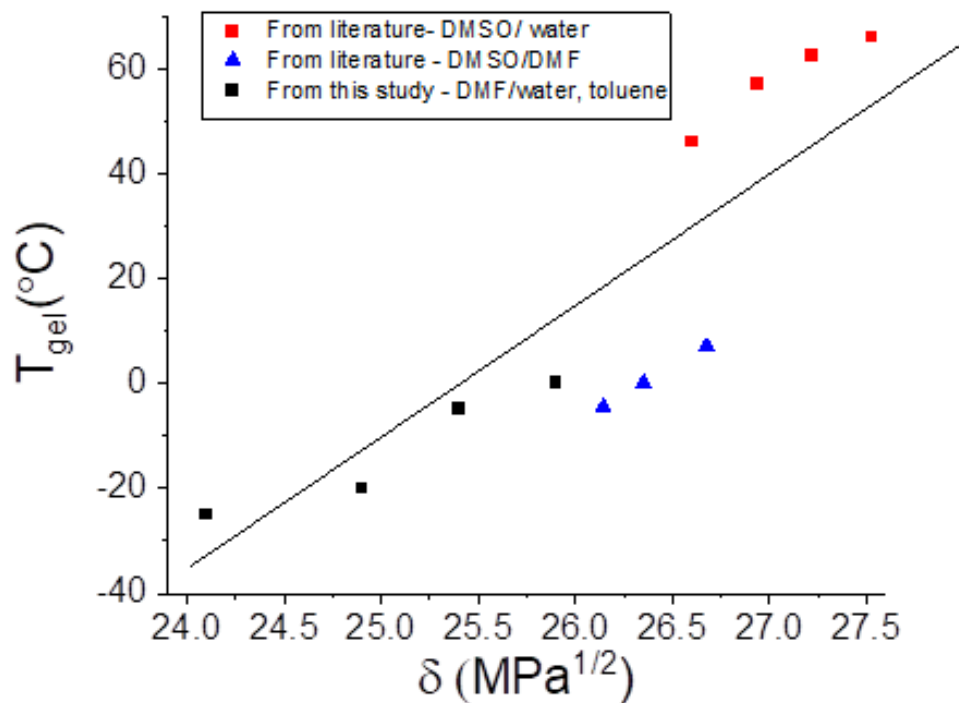


Figure A4. Correlation between gelation temperature (T_{gel}) and Hansen's solubility parameter δ . Red square showed the T_{gel} from ref [14], Blue rectangle showed the T_{gel} from ref [18]. Solid line is used to visualize the trend.

To check the co-solvent effect on gel spinning, a simple step of addition of water into PAN/DMF solution has been done when making PAN solutions, and these solutions were used for the gel spinning process of PAN fibers. Table A3 summarizes the tensile properties of the as-spun fibers from the three spinning trials. Despite the comparable tensile strength and modulus, the elongation to break and toughness significantly decreased with increased water content in the polymer solution. One possible explanation could be that water addition into dope solution introduces more defects during the gel spinning process. This hypothesis is supported by the $\log G'$ versus $\log G''$ curve from Figure A3

from the rheology study. During the oscillation test from high temperature (50 °C) to low T_{gel} , polymer solution became more inhomogeneous with higher water content. Wide-angle X-ray diffraction was used to measure the structural properties of the as-spun fibers. While all these as-spun fibers have similar crystal sizes and orientations, the addition of water decreased the crystallinity of the as-spun fibers.

Table A3. Summary of mechanical and structural properties of as-spun fibers from PAN/DMF and PAN/DMF/water solutions.

	unit	PAN/DMF	PAN/DMF/Water	PAN/DMF/Water
Water content	vol %	0	4	7
TDR		3	3	3
Diameter	μm	33.3 ± 0.5	33.9 ± 0.6	34.9 ± 0.4
Tensile Strength	MPa	202 ± 7	193 ± 8	224 ± 11
Modulus	GPa	7.1 ± 0.1	7.0 ± 0.1	7.4 ± 0.1
Elongation at break	%	79.6 ± 5.8	58.8 ± 4.0	42.1 ± 3.2
Toughness	MPa	132.3 ± 9.4	98.9 ± 7.4	78.3 ± 6.6
Crystallinity (%)	%	46	41	39
Crystal size	nm	3.0	3.0	3.4
f_{PAN}		0.28	0.3	0.29

Table A4 lists both the mechanical properties and structural parameters of the fully drawn fibers made from solutions with different water content. Fibers from solution with a small amount of water (4 vol %) showed comparable drawability, tensile strength, and modulus to fiber made from PAN/DMF. High water (7 vol%) containing PAN solution resulted in a lower draw ratio and reduced tensile strength and modulus. The fiber orientation factor also decreased from 0.85 to 0.79. Fully drawn fiber made from PAN/DMF/water with 7 vol % water also showed smaller crystal size than PAN fibers made from the other two solutions.

Table A4. Summary of mechanical and structural properties of fully drawn fibers from PAN/DMF and PAN/DMF/water solutions.

	unit	PAN/DMF	PAN/DMF/Water	PAN/DMF/Water
Water content	vol %	0	4	7
TDR		24	24	21
Diameter	μm	11.8 ± 0.2	12.0 ± 0.3	12.9 ± 0.9
Tensile Strength	MPa	890 ± 25	828 ± 19	762 ± 23
Modulus	GPa	18.1 ± 0.4	17.6 ± 0.3	15.3 ± 0.4
Elongation at break	%	7.8 ± 0.2	8.2 ± 0.1	8.3 ± 0.1
Toughness	MPa	32.4 ± 1.1	33.4 ± 0.7	29.6 ± 1.1
Crystallinity (%)	%	62	65	65
Crystal size	nm	8.6	9.2	7.2
f_{PAN}		0.87	0.85	0.79

Use of solvent mixture with high R_a values (DMF/water (7 vol%)) decreased tensile strength, modulus, and drawability of PAN fibers. Based on this case study, we hypothesized that the use of solvent, solvent mixtures with low R_a values would improve the tensile strength and modulus of PAN fibers from gel spinning. A variety of solvents were screened for PAN by calculating R_a values. Some of the promising solvents and solvent mixtures are summarized in Table A5. R_a values lower than DMF have been calculated for propylene carbonate (PC), DMSO, ethylene carbonate (EC), sulfolane, and some of their mixtures.

Table A5. Solvents and solvent mixtures for PAN that show low Hansen’s solubility parameter R_a for PAN^[79].

	Volume ratio	δ	δ_d	δ_p	δ_h	R_a
PAN	-	27.4	21.7	14.1	9.1	-
DMF	-	26.3	17.4	13.7	11.3	8.9
DMSO	-	26.6	18.4	16.4	10.2	7.1
PC	-	27.2	20.0	18.0	4.1	7.2
DMF/PC	65/35	25.4	18.3	15.2	8.8	6.9
DMSO/PC	40/60	26.7	19.0	17.0	7.8	6.2
DMF/EC	50/50	26.4	18.4	17.3	7.9	7.4
Sulfolane	-	29.4	20.3	18.2	10.9	5.3
Sulfolane/PC	75/25	28.7	20.2	18.2	9.2	5.0
Sulfolane/PC	50/50	28.1	20.2	18.1	7.5	5.3
Sulfolane/Toluene	90/10	27.9	20.1	16.5	10.0	4.2

We then evaluated multiple solvent mixtures with DMF (Table A6). Good solvent PC with a lower R_a value than DMF was added to DMF for PAN fiber spinning. 10 vol% PC into DMF reduces the R_a from 8.9 to 8.2, and further addition of PC to 35 vol % further reduces the R_a to 6.9. Adding 10 vol% PC increased the tensile modulus of the resulting PAN fiber by about 7 % when compared with PAN fiber made from PAN dissolved in only DMF (Table A6). However, adding 35 vol% PC did not further increase the tensile modulus but reduced the tensile strength by about 20% than fibers made from PAN/DMF. 20 vol% toluene was also added into the DMF to investigate the non-polar solvent effect on gel spinning of PAN. In the previous gelation study, 7 vol% toluene was shown to

reduce the T_{gel} for PAN in DMF. Here, we added 20 vol% toluene to maintain the same R_a value as DMF, but reduced the δ_p from 14.1 to 11.2. Toluene reduced tensile strength and modulus of the resulting PAN fiber by 12 % and 7 %, respectively. The results suggested the polar interaction of solvent would also influence the resulting gel spun fiber properties.

Table A6. DMF and solvent mixtures with DMF used for fiber spinning, and the resulting fiber tensile properties.

	Volume ratio	R_a	δ_p	Max draw ratio	Tensile strength (MPa)	Tensile modulus (GPa)
DMF		8.9	14.1	24	890 ± 25	18.1 ± 0.4
DMF/water	96/4	9.4	15.0	24	828 ± 19	17.6 ± 0.3
DMF/water	93/7	10.1	16.0	21	762 ± 23	15.3 ± 0.4
DMF/PC	90/10	8.2	14.1	23	860 ± 32	19.3 ± 0.3
DMF/PC	65/35	6.9	15.2	15	724 ± 32	17.7 ± 0.4
DMF/Toluene	80/20	8.8	11.2	24	787 ± 21	16.9 ± 0.3

After adding non-solvent water, good solvent PC, and non-polar solvent toluene in DMF, we showed that both the overall interaction parameter between the solvent and the polymer, as well as the polar interaction of solvent, could influence the resulting PAN fiber tensile properties. R_a and δ_p can provide some guidance for selecting solvent and solvent mixtures.

Furthermore, we assessed a completely different solvent system, sulfolane, and sulfolane/cosolvent mixtures, based on the prediction of solubility parameters. Sulfolane is

a highly stable dipolar aprotic solvent which is used as a solvent in the industry for a variety of chemical reactions, including acidic, oxidation, phosphorylation, and condensation reactions [176]. Sulfolane has a boiling point of 287°C, which is much higher than other aprotic solvents such as DMF (153°C) and DMSO (189°C). PC is also a good solvent for PAN. After the screening of solvents, we found that sulfolane and its solvent mixtures with PC and toluene showed the lowest R_a , based on all the available solvent data on solubility parameters[175]. Also, to the best of our knowledge, sulfolane has never been reported for fiber spinning of PAN.

Table A7 shows the η^* of PAN dissolved in sulfolane and its solvent mixtures measured at room temperature and at 1 rad/s. Interestingly, the same PAN powder dissolved in sulfolane possessed significantly higher viscosity than dissolved in DMF. At 8 g/dL, sulfolane, sulfolane/PC, and sulfolane/ toluene all showed even higher η^* than PAN/DMF at 10.5 g/dL. The sulfolane can lead to a PAN fiber spinning at low solid content, which can potentially lead to a low entanglement density of PAN in the solution.

During gel spinning, we observed that the coagulation of PAN/sulfolane solution was difficult. Table A8 summarizes the attempts of coagulation. Methanol and water resulted in fast coagulation of PAN and led to white fiber, which was extremely brittle. Acetone alone was not able to coagulate PAN, and the fiber could not be collected through the acetone bath. An acetone/methanol (33/67) bath was successfully used to coagulate a transparent as-spun fiber. However, the drawing of this fiber was not stable, and fibers were not drawable using a hot glycerol bath. The maximum draw ratio was less than 1.5.

Table A7. Solubility parameters and complex viscosity of PAN in DMF, sulfolane, PC, sulfolane/PC, and sulfolane/toluene mixtures

Solvent #1	Solvent #2	Solvent #2 vol%	Solid content (g/dL)	R_a	δ_p	η^* (Pa.s) at 1 rad/s at 25 °C
DMF	none	N/A	10.5	8.9	13.7	48
Sulfolane	None	N/A	8	5.3	18.2	90
PC	None	N/A	8	7.2	18.0	43
Sulfolane	PC	25	8	5.0	18.15	70
Sulfolane	PC	50	8	5.3	18.1	50
Sulfolane	Toluene	10	8	4.2	16.5	110

Sulfolane, sulfolane/PC (25 and 50 vol%) were used for fiber spinning of PAN.

Sulfolane mixtures with PC were also spun. Sulfolane/PC (75/25) was successfully coagulated in a methanol bath maintained between 0 and 10 °C. However, the drawing process was not stable, and fiber was drawable in the glycerol bath with a maximum draw ratio of ~ 4 with a short period of time (~ 3 minutes). A 50/50 sulfolane/PC mixture was used to dissolve PAN and successfully produced PAN precursor with stable coagulation and fiber drawing. The resulting precursor fiber possessed tensile strength and modulus of 515 MPa, and 15 GPa, respectively (Table A9). Both tensile strength and modulus were lower than those of PAN fibers made with DMF. However, the tensile strength and modulus are comparable to the commercial available PAN fiber reported in the literature [3,81,104,177–179]. The drawn fiber diameter was about 15 μm , which was also comparable to the current commercial precursor PAN used for making carbon fiber. Further optimization of the sulfolane/PC volume ratio, coagulation, and drawing condition

may lead to improved tensile properties of the resulting fibers. This can potentially provide an alternative method for making PAN-based carbon fiber precursors.

Table A8. Coagulation and drawing of PAN fiber processed from a concentration of 8g/dL in sulfolane.

Bath	Coagulation				Drawing	
	T (°C)	Coagulation Speed	Fiber color	Fiber collection	Cold Drawable	Hot Drawable
Methanol	15	Moderate	White	Stable	No	No
Water	15	Fast	White	Stable	Yes	No
Methanol /water (70/30)	15	Fast	Transparent to white	Stable	Yes	No
Methanol	0	Moderate	Transparent to white	Unstable	Yes	No
Methanol*	-30	Jet freeze	Transparent	Unstable	N/A	N/A
Methanol*	-50	Jet freeze	Transparent	Unstable	N/A	N/A
Acetone*	15	Slow	Transparent	Unstable	N/A	N/A
Acetone/methanol (50/50)	15	Moderate	Transparent to white	Stable	No	No
Acetone/methanol (33/67)	15	Moderate	Transparent to white	Stable	Yes	unstable

*Fibers were not collected successfully from spinning, and drawing was not able to be attempted.

The structural parameters of precursor made from PAN dissolved in sulfolane/PC were also measured and compared with PAN made from DMF. PAN fibers made from sulfolane/PC showed larger crystal size, comparable crystallinity, but lower f_{PAN} as compared to PAN fiber made from PAN/DMF. Figure A5 showed that the PAN precursor

made from the new solvents showed the same typical peaks of PAN at $2\theta \sim 17$ and 29° , which indicated a hexagonal packing of the PAN crystal [180].

Table A9. Tensile properties and structural parameters of PAN precursor fibers made from DMF, sulfolane/PC (50/50), and from literature.

	unit	PAN/DMF	PAN/Sulfolane/PC	Commercial PAN precursor [3,81,104,177– 179]
TDR		24	15	-
Diameter	μm	11.8 ± 0.2	15.4 ± 0.5	6 - 14
Tensile Strength	MPa	890 ± 25	515 ± 24	450 - 1000
Modulus	GPa	18.1 ± 0.4	15.0 ± 0.3	12-17
Elongation at break	%	7.8 ± 0.2	7.5 ± 0.3	-
Toughness	MPa	32.4 ± 1.1	23.3 ± 1.5	-
Crystallinity (%)	%	62	62	-
Crystal size	nm	8.6	10.6	-
f_{PAN}		0.87	0.77	-

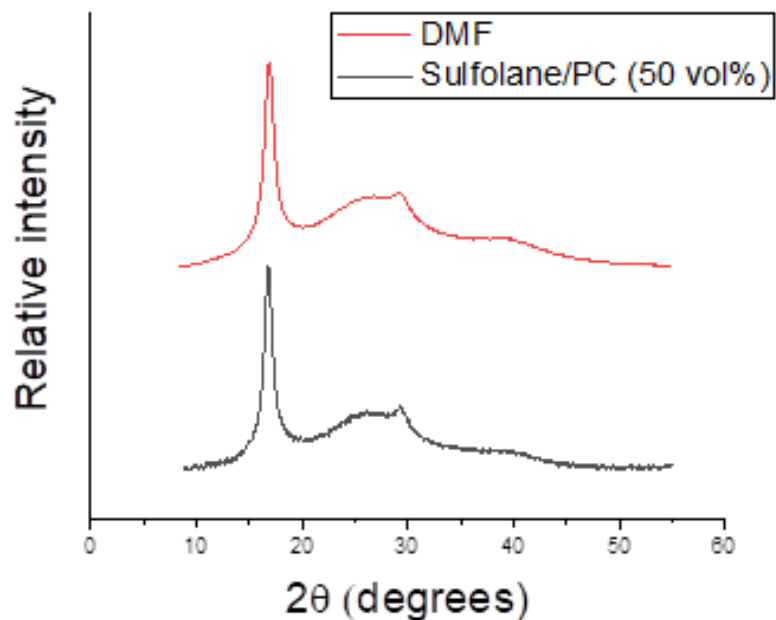


Figure A5. WAXD integrated scans of fully drawn PAN fibers spun from DMF and from sulfolane/PC (50/50) solvent mixture.

A.4 Conclusions

To conclude, the gelation behavior of PAN with water and toluene in DMF was studied. Adding water increased while adding toluene decreased the T_{gel} of PAN/DMF solution. The gelation process of PAN/DMF/water solution is different from the gelation process of PAN/DMF, which can be due to the liquid-liquid phase separation. Increased water content in the PAN/DMF solution decreased the elongation to break of resulting as spun fibers from gel spinning, which can be due to the inhomogeneity of solution during gelation. 7 vol % water addition also reduced the drawability and tensile properties of fully drawn fibers made from PAN/DMF.

Besides non-solvent water, good solvent PC with low R_a and non-polar solvent toluene was added into the DMF to dissolve PAN for gel spinning. PAN fibers made from PAN/DMF/PC solution with 10 vol% PC increased the tensile modulus by about 7 %, as compared to the PAN fibers made from PAN/DMF solution. Adding 20 vol % toluene in DMF, on the other hand, reduced the tensile strength and modulus of the resulting fibers than the fibers made from PAN/DMF. Both, overall interaction between solvent and polymer and polar interaction of solvent can influence the PAN fiber tensile properties through gel spinning.

Hansen's solubility parameter values were used to screen a variety of solvents and solvent mixtures for PAN. Sulfolane and its solvent mixtures with PC and toluene were found to have the lowest R_a for PAN. Sulfolane and sulfolane/PC were gel spun with a reduced PAN solid content at 8 to 8.5 g/dL as compared to PAN/DMF, which was spun at 10.5 g/dL. Coagulation was found to be difficult for gel spun PAN/sulfolane. PAN/sulfolane/PC with 50 vol% of PC, on the other hand, was successfully spun to produce PAN fiber, which possessed comparable tensile strength and modulus as those of commercial PAN precursor used for carbon fiber manufacturing reported in the literature.

APPENDIX B. SUPPORTING INFORMATION FOR CHAPTER 2

Table B1. Composition and processing parameters of pure PAN solution and of PAN/CNT and PAN/CNC dispersions.

Solution/ dispersion	PAN weight (g)	PAN wt%			CNT/CNC weight (g)	Solvent	Dispersion Conc. (mg/100 mL)	Sonication Time hours)
		M_{V1}	M_{V2}	M_{V3}				
PAN	7	-	75	25	0	-	-	-
PAN/CNT-4	6.72	-	75	25	0.28	DMF	11.6	48
PAN/CNT-10	6.66	-	75	25	0.74	DMF	11.6	48
PAN/CNT-15	6.12	-	75	25	1.08	DMF	11.6	48
PAN-2/CNT-10	10.35	100	-	-	1.15	DMF	11.6	48
PAN/CNC-60	4	-	100		6	DMF/H ₂ O (75/25)	3000	48

M_{V1} ; M_{V2} and M_{V3} correspond to viscosity average molecular weight of 247,000; 500,000 and 964,000 g/mol, respectively.

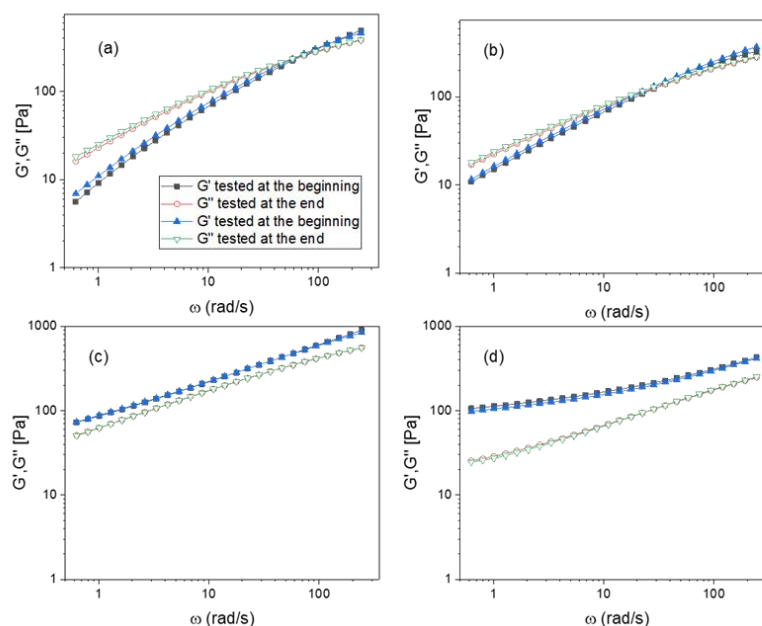


Figure B1. G' , G'' plots with respect to ω of (a) PAN, (b) PAN/CNT-4, (c) PAN/CNT-10, and (d) PAN/CNT-15 tested at 20 °C at the beginning and at the end of temperature sweep in order to check reversibility of temperature effects

Table B2. $\log G' - \log G''$ slope when $\omega \rightarrow 0$ for PAN solution and PAN/CNT dispersions at different temperatures.

Temperature (°C)	PAN	PAN/CNT-4	PAN/CNT-10	PAN/CNT-15
0	1.36	1.22	0.94	0.48
10	1.36	1.22	0.92	0.46
20	1.38	1.21	0.89	0.46
30	1.38	1.21	0.87	0.43
40	1.39	1.21	0.88	0.43
50	1.4	1.21	0.87	0.45
60	1.42	1.2	0.83	0.46

Table B3. Summary of fiber spinning parameters and continuous jetting time for PAN/CNT dispersions.

	PAN/CNT-10	PAN/CNT-15	PAN/CNT-10-2
Temperature (°C)	90	90	90
Spinneret size (μm)	200	500	200
Air gap (cm)	6	6	6
Flow rate of dispersion (ml/min)	0.5-1	0.5	0.5-1
Shear rate (s ⁻¹)*	1300-2600	84	1300-2600
Continuous jetting time (min)	6 ± 2	< 2	24**

*The shear rate can be roughly estimated using a steady-state shear rate equation $\dot{\gamma} = \frac{4Q}{\pi R^3}$, where Q is the flow rate, and R is the radius of the spinneret hole. **No breakage during the full duration of the fiber spinning process.

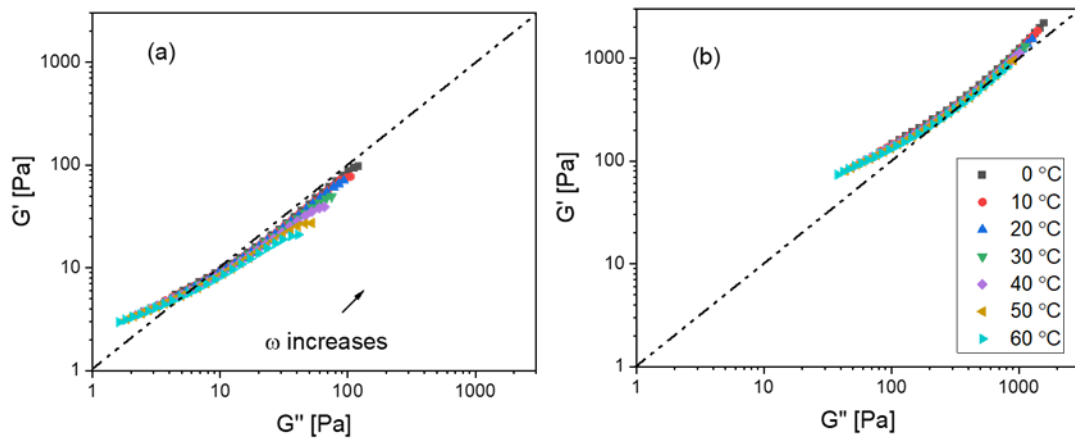


Figure B2. Log-log plot of G' versus G'' for (a) diluted PAN/CNT-10 (at 4.5 g/dL of solids), and (b) PAN/CNT-10-2 dispersion at various temperatures; frequency range from 0.63 to 242 rad/s.

APPENDIX C. SUPPORTING INFORMATION FOR CHAPTER 3

Table C1. Comparison of electrical conductivity measurement results from the 2-probe and 4-probe method for three select samples of 4.4 wt% CNT.

Sample	Draw ratio			Annealing	Electrical conductivity (S/m)	
	CDR	HDR	TDR		2-probe method	4-probe method
A2	1	-	1	-	0.05 ± 0.01	0.06 ± 0.04
A2-1	1	3	3	-	0.38 ± 0.21	0.80 ± 0.60
A2-1	1	3	3	180 °C for 30 minutes	4.7 ± 0.3	2.4 ± 2.0

Table C2. Processing conditions and temperature measured by an IR sensor near the center of fibers bundle during Joule heating experiments.

Trial	Applied voltage (kV)	Number of filaments	Length of tows (m)	Joule heating time (min)	Temperature measured (°C)
1	1.45			30	245
2	1.3			60	255
3	1.2	100	1	120	248
4	1.5			180	252

Table C3. Summary of results from electrical conductivity measurements.

Sample	Draw Ratio	Annealing		CNT wt%	Conductivity (S/m)	std (\pm)
		Time (min)	Temperature ($^{\circ}$ C)			
A1	1	0	-	3.7	0.006	0.002
A2	1	0	-	4.4	0.05	0.006
A3	1	0	-	5.6	0.42	0.04
A4	1	0	-	6.6	0.25	0.06
A1	1	3	180	3.7	1.1	0.3
A1	1	30	210	3.7	3.0	2.6
A2	1	3	180	4.4	1.6	0.4
A2	1	8	180	4.4	1.4	0.1
A2	1	15	180	4.4	2.4	0.5
A2	1	30	180	4.4	2.4	1
A2	1	60	180	4.4	4	0.3
A2	1	30	150	4.4	0.7	0.3
A2	1	30	210	4.4	3.6	1.6
A3	1	3	180	5.6	10.5	2.2
A4	1	3	180	6.6	13	2.7
A2-1	3	0	-	4.4	0.38	0.2
A2-1	3	3	180	4.4	1.1	0.1
A2-1	3	30	180	4.4	4.7	0.3
A2-2	10	0	-	4.4	$< 10^{-4}$	-
A2-2	10	3	180	4.4	0.0007	-
A2-2	10	30	180	4.4	0.035	0.03

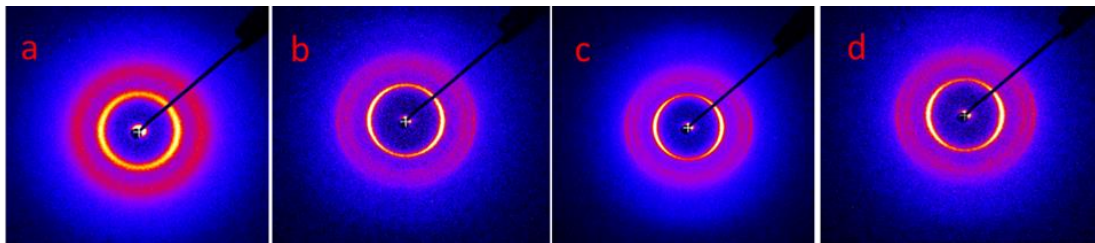


Figure C1. 2-D WAXD patterns of A2 samples with various annealing times at 180 $^{\circ}$ C. (a) before annealing, (b) 3 minutes, (c) 30 minutes, and d) 60 minutes of annealing.

APPENDIX D. SUPPORTING INFORMATION FOR CHAPTER 4

Table D1. Mechanical properties and structural parameters of PAN and PAN/CNT precursor fibers.

Sample	PAN	PAN/CNT-1	PAN/CNT-2	PAN/CNT-3
Tensile strength (MPa)	774 ± 81	570 ± 102	491 ± 45	423 ± 61
Tensile modulus (GPa)	16.8 ± 1.5	18.8 ± 1.2	16.4 ± 0.6	17.4 ± 1.8
Strain at break (%)	8.5 ± 0.8	6.0 ± 1.4	6.7 ± 2.6	9.0 ± 2.0
Fracture toughness (MPa)	31.4 ± 3.6	19.8 ± 7.2	20.7 ± 4.4	27.0 ± 8.7

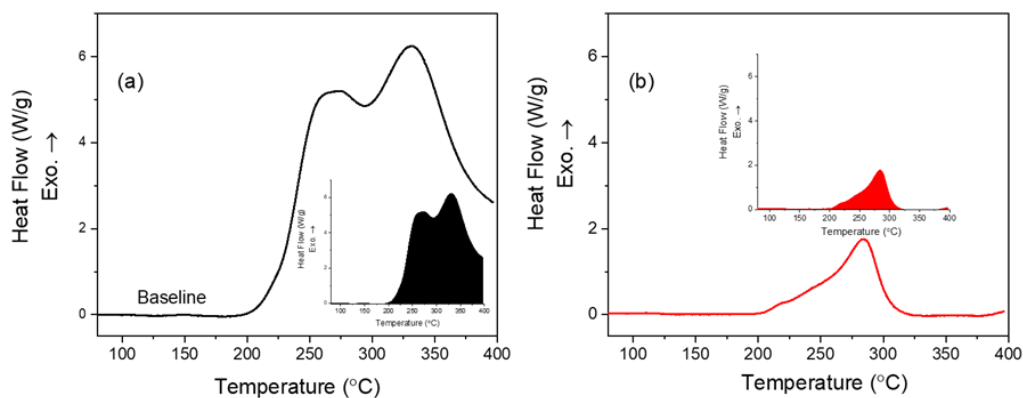


Figure D1 DSC curves of PAN powder under (a) air and (b) N₂ environment at 10 °C. The insets showed the areas used to calculate the $\Delta H_{reaction}$.

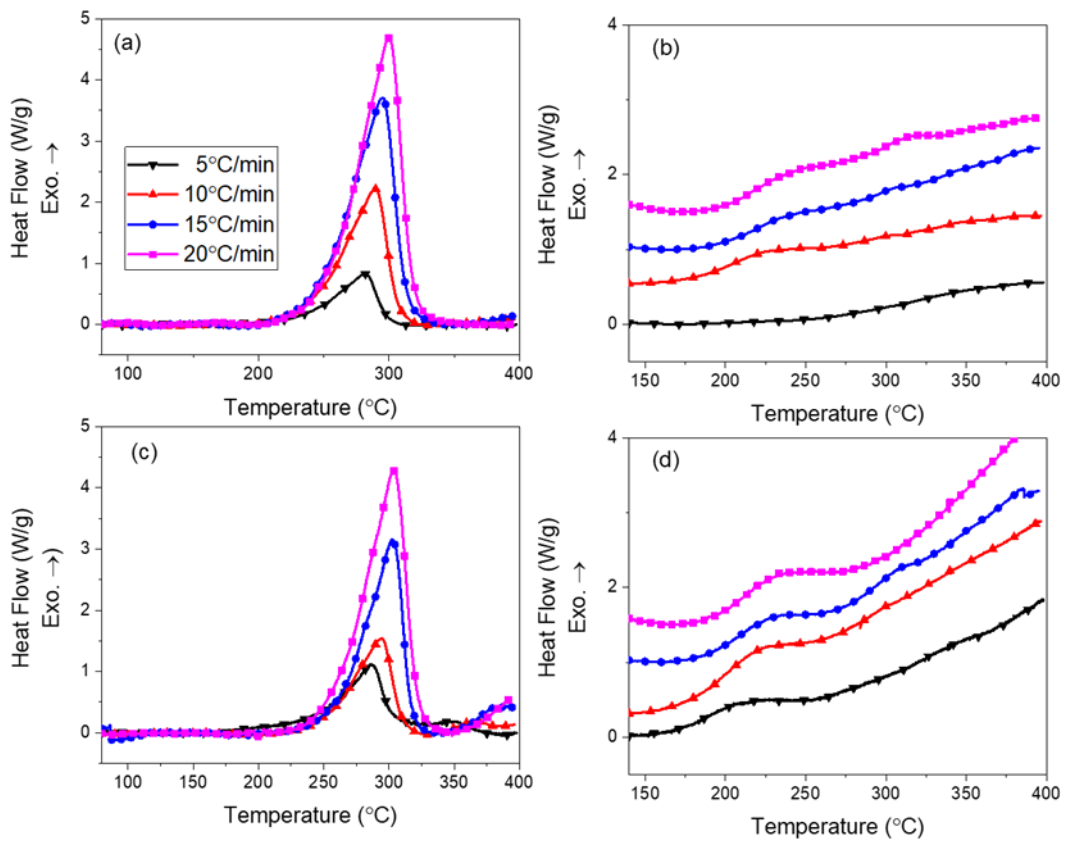


Figure D2. DSC curves at various heating rates with (a) PAN fiber in N₂; (b) PAN fiber rerun in the air after runs in N₂; (c) PAN/CNT-1 fiber in N₂; (d) PAN/CNT-1 fiber rerun in the air after runs in N₂.

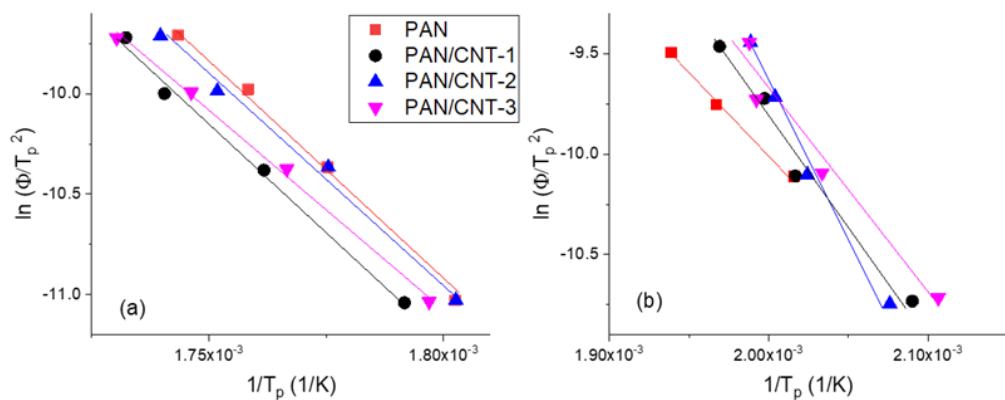


Figure D3. Plots for the activation energy of (a) cyclization; and (b) oxidation, according to Kissinger's equation [161].

Table D2. Calculated kinetic parameters from Kissinger's equation.

	Reaction	E_a (kJ/mol)	A (s^{-1})
PAN	Cyclization	187.5	1.7×10^{17}
	Oxidation	65.7	2.6×10^6
PAN/CNT-1	Cyclization	177.8	1.5×10^{16}
	Oxidation	87.5	8.0×10^8
PAN/CNT-2	Cyclization	169.8	3.3×10^{15}
	Oxidation	122.3	5.6×10^{12}
PAN/CNT-3	Cyclization	164.3	8.6×10^{14}
	Oxidation	81.3	1.9×10^8

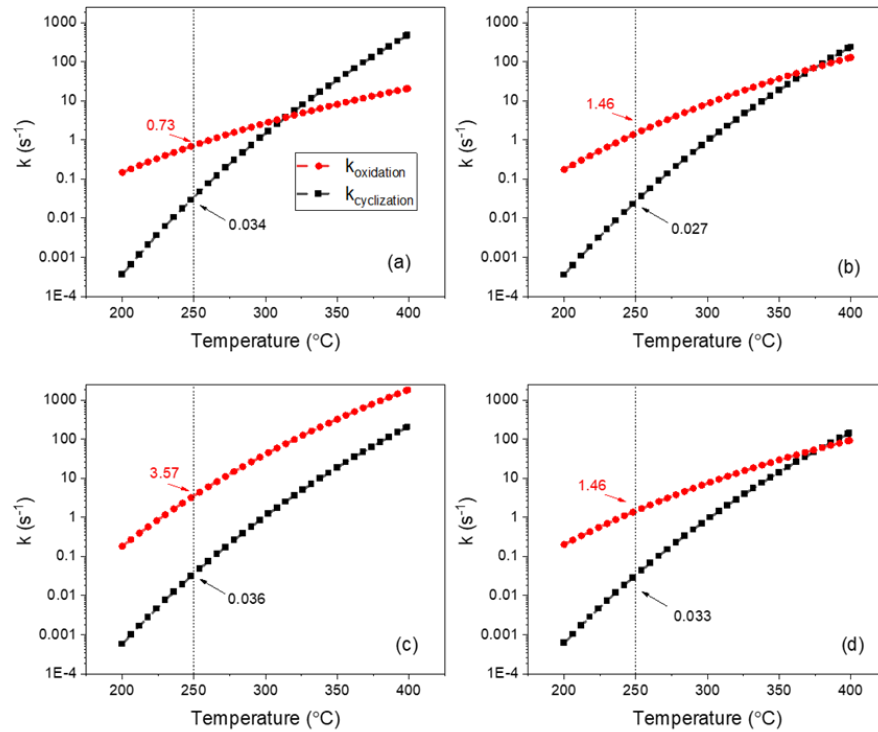


Figure D4. Kinetic constants versus temperature of (a) PAN, (b) PAN/CNT-1, (c) PAN/CNT-2, and (d) PAN/CNT-3 fibers.

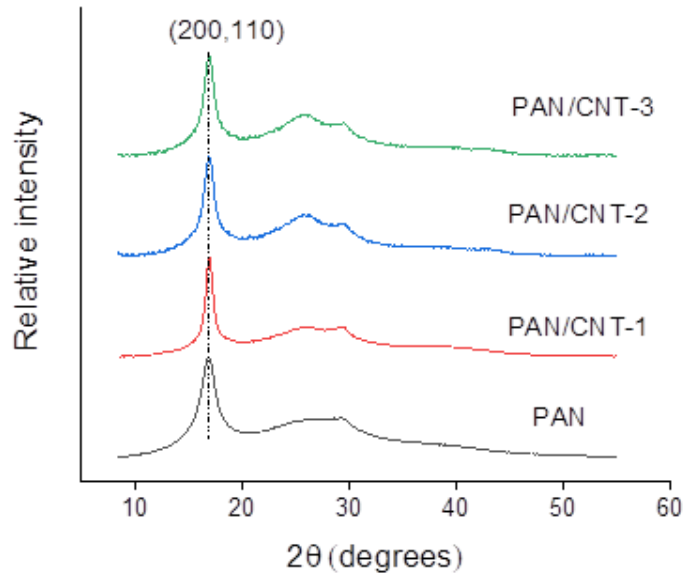


Figure D5. Integrated scans of WAXD patterns of PAN and PAN/CNT fibers before stabilization.

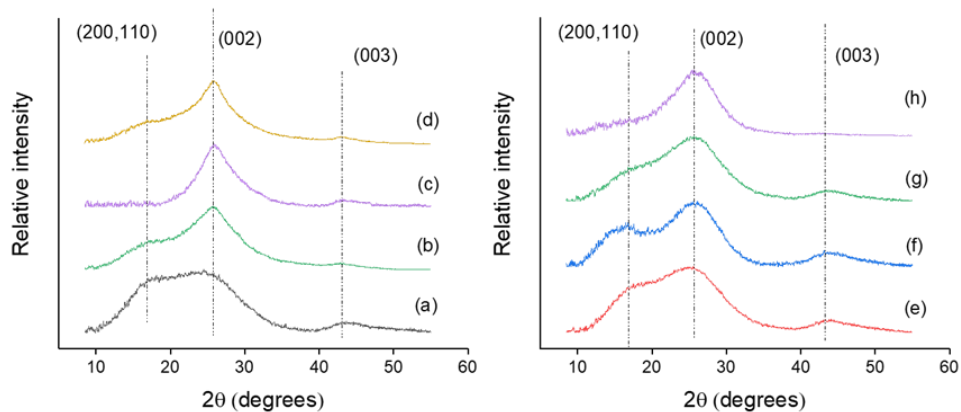


Figure D6. Left: Integrated scan of WAXD patterns of (a) PAN, (b) PAN/CNT-1, (c) PAN/CNT-2, and PAN/CNT-3 after 2-hours stabilization; Right: Integrated scan of WAXD patterns of PAN fibers after (e) 3-hours, (f) 4-hours, (g) 5-hours, and (h) 6-hours stabilization at 250 °C under air environment.

The porous structure observed under SEM qualitatively explained the increase of oxygen diffusion in PAN/CNT sheaths. To quantitatively evaluate the effect of porous structure on gas diffusion, we established a diffusion equation to estimate the average apparent diffusion coefficient of O₂ (D_{O_2}) [181,182]:

$$\frac{\partial C}{\partial t} = D_{O_2} \nabla^2 C \quad (D-1)$$

Where C is the concentration of O₂ in fiber and t is the time. The average apparent D_{O_2} of pure PAN fiber was estimated in previous literature to be $\sim 3 \times 10^{-12}$ cm²/s at 250 °C when considering diffusion is limited due to an oxidized interphase skin layer [76,183].

The aspect ratio of fiber bundles when conducting stabilization was about 170 with 17 cm length, the equivalent diameter of 20-filament bundle about 100 μm, and thus when estimated the O₂ diffusion in fiber, we only consider the diffusion along the radial direction. Based on this assumption, the equation (D-1) can be simplified as:

$$\frac{\partial C}{\partial t} = D_{O_2} \frac{\partial^2 C}{\partial r^2} \quad (D-2)$$

Assuming the surface concentration remains constant, the diffusion of O₂ starts from $t = 0$ s, the solution to equation (D-2) becomes

$$\frac{C}{C_0} = 1 - 2 \sum_{n=1}^{\infty} e^{-\beta_n^2 \tau} \frac{J_0\left(\frac{r\beta_n}{r_0}\right)}{\beta_n J_1(\beta_n)} \quad (D-3)$$

Where β_n ($n = 1, 2, \dots$) are roots of the Bessel equation $J_0(\beta) = 0$, which are documented by Carslaw and Jaeger [182]. C_0 is the concentration of O_2 in air, which is assumed constant at 21% with continuous pumping air. And $\tau = \frac{D_{O_2}t}{r_0^2}$ where t is the total time of the diffusion process. It should be noted that the equation above may not strictly apply to the systems with reaction. In this simplified equation, D_{O_2} is a function of reaction. Moreover, the reaction would change the morphology and surface area of the PAN/CNT in fibers, which would influence gas diffusion. It is not feasible to measure the real D_{O_2} by experiment nor calculate it analytically. To simplify the problem, we only estimate the average apparent D_{O_2} of PAN/CNT fiber.

Figure D7 shows the estimated normalized concentration profile of PAN and PAN/CNT fibers. PAN fibers required ~ 6 hours to stabilize (Figure D6). To reach the comparable concentration profile, the apparent D_{O_2} of PAN/CNT-2 is estimated to be about 3-4 times of that of pure PAN fiber for a complete stabilization within 2-hours. In other words, the simulated results indicated the CNT that displayed porosity induced by phase separation led to an average apparent D_{O_2} that was up to 3-4 times higher than control PAN fibers for stabilization.

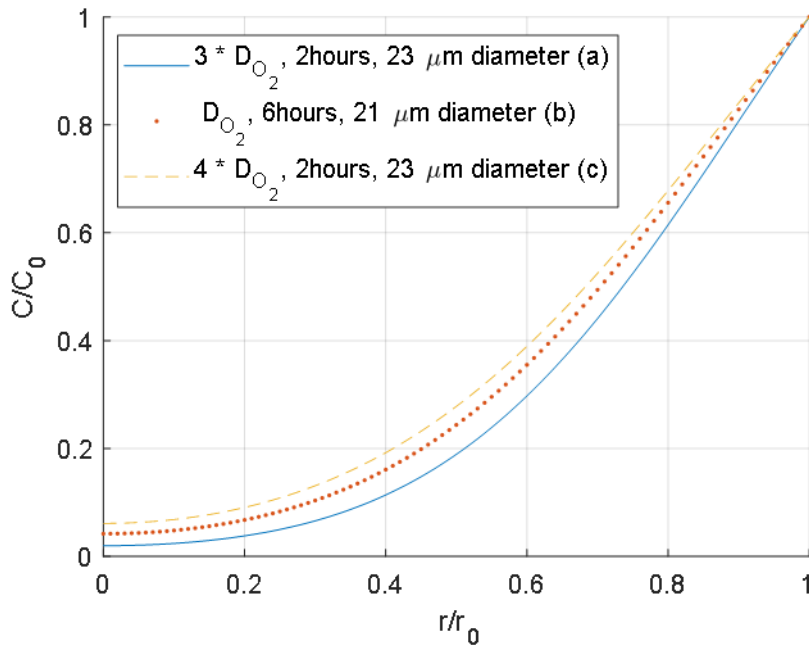


Figure D7. Normalized O₂ concentration profile calculated by Equation (D-2) of (a) PAN/CNT-2 fiber of 23 μm diameter and 3 * D_{O₂} after 2-hours stabilization, (b) PAN fiber of 21 μm diameter and D_{O₂} after 6-hours stabilization (c) PAN/CNT-2 fiber of 23 μm diameter and 4 * D_{O₂} after 2-hours stabilization. D_{O₂} ~ 3 x 10⁻¹² cm²/s at 250 °C was used for calculation for PAN fiber

APPENDIX E. SUPPORTING INFORMATION FOR CHAPTER 5

Table E1. Summary of solution preparation and fiber spinning parameters for single and bi-component fibers.

	Single- component	Bi- component (sheath solution)	Bi- component (core solution)
CNT wt%	7	10	0
PAN polymer wt%	93	90	100
PAN M_v g/mol*	500,000 (75%) 964,000 (25%)	247,000	247,000
CNT concentration for sonication (mg/L DMF)	200	120	-
Sonication time (hours)	24	24	-
Solid content (g/100 mL DMF)	11	11.5	15.5
Solution quantity (L)	1.5	1.5	3
Solution preparation temperature	75	90	75
Spinneret diameter (μm)	200	200	200
No. of holes in the spinneret	40	40	40
Spinneret temperature ($^{\circ}\text{C}$)	95	90	90

*All PAN polymer contains 4 wt% methacrylic acid (MAA) copolymer.



Figure E1. Photographs of stabilized bi-component fiber tow via joule heating; (A) and (B) 6000 filaments.

Table E2. Joule heating conditions for single-component fibers.

Applied Voltage (kV)	Current (mA)	Number of filaments	Fiber moving speed (m/hour)	Joule heating time (hour)	Temperature measured (°C)
1.95	9.1	200	8	0.25	250
	11.2		4	0.5	250
	11.3		2	1	250

Table E3. Joule heating conditions for bi-component fibers.

Applied Voltage (kV)	Current (mA)	Number of filaments	Fiber moving speed (m/hour)	Joule heating time (hour)	Temperature measured (°C)
1.2	77.4	6000	1	2	250
1.6	23.7	1000	0.5	4	250

Table E4. The electrical conductivity of single and bi-component fibers before and after various annealing conditions.

Sample	Annealing process*	Annealing temperature (°C)	Annealing time (min)	Electrical conductivity (S/m)
Single-component	-	-	-	10^{-3}
	Batch	210	10	0.8 ± 0.8
	Batch	210	30	5.9 ± 3.1
	Batch	210	60	5.9 ± 2.9
	Continuous	210	30	11.5 ± 3.1
Bi-component	-	-	-	1.1 ± 0.6
	Batch	210	10	7.1 ± 0.7
	Batch	210	30	8.5 ± 0.3

*Batch annealing was done in a vacuum oven at a constant length, and continuous annealing was done in a laboratory scale continuous carbonization facility at Georgia Tech[12].

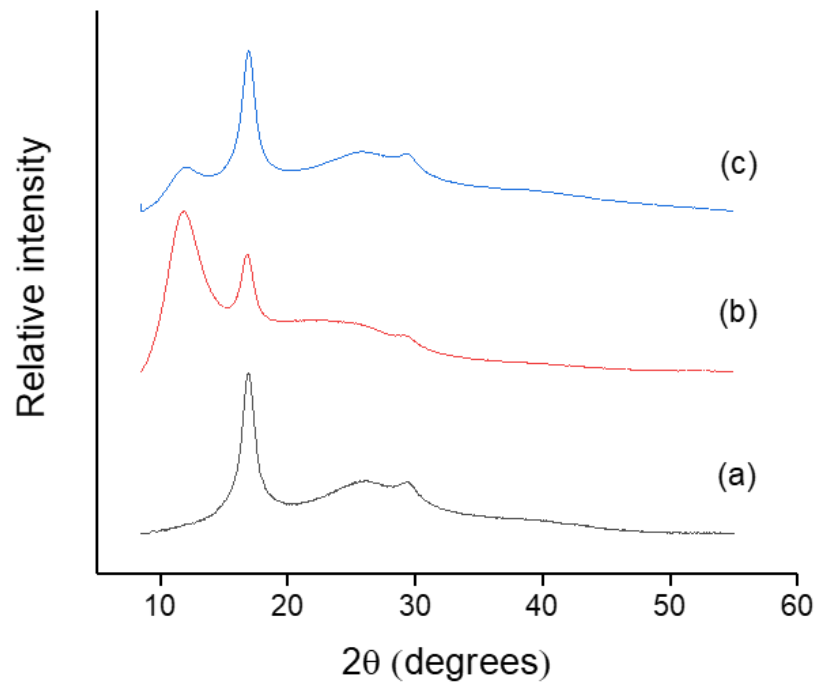


Figure E2. WAXD integrated scan of bi-component fibers. (a) without spin finish, (b) fiber immersed into the spin finish bath for 6-hours followed by drying at 80 °C in a vacuum oven, (c) after rinsing and washing fiber (b) in water and followed by drying. This figure confirms that 12 degree peak is due to spin finish (MATSUMOTO YUSHI-SEIYAKU Co., Ltd. Osaka, Japan)

Table E5. Summary of tensile properties and structural parameters for single and bi-component precursor fibers used for this study.

Sample	CNT wt%	DR	Diameter (μm)	Tensile strength (GPa)	Tensile modulus (GPa)	Strain at break (%)	Xc (%)	f_{PAN}	Crystal size (nm)	f_{CNT}
Single-component	7	1.2	33 ± 2	0.18 ± 0.01	9.7 ± 0.6	7.5 ± 2.7	56	0.37	9.3	0.35
Bi-component	4.6	1.1	52 ± 2	0.1 ± 0.003	7.6 ± 0.3	6.4 ± 1.5	51	0.43	7.7	0.06

DR: draw ratio, Xc – Crystallinity of PAN, f – Herman’s orientation factor.

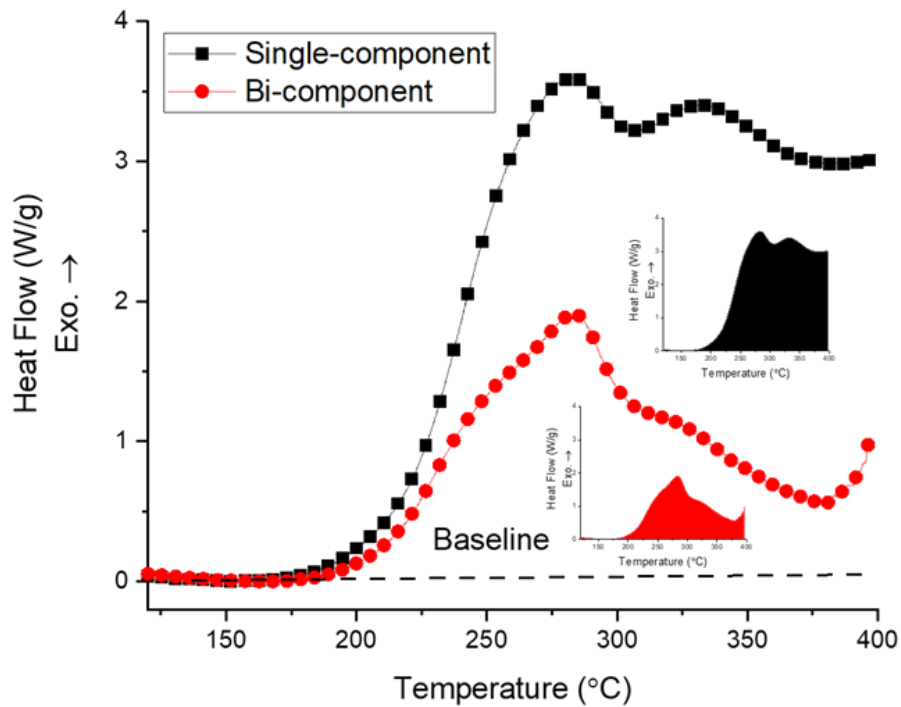


Figure E3. DSC scan of single-component and bi-component fibers at 10 °C/min in air. The area (inlet) under the DSC curve and above the baseline between 200 and 400 °C were used to calculate the heat released from the stabilization reaction. The enthalpy of reaction is 2980 and 1194 J/g for single and bi-component fibers, respectively.

Before analyzing the Joule heating process, it is essential to know whether the fiber bundles are uniformly heated during Joule heating. Biot number, the ratio between internal thermal resistance (through conduction) and external thermal resistance (through convection), was calculated by

$$Bi = \frac{hD}{k} \quad (\text{E-1})$$

where h is the convective coefficient of air ($\sim 10 \text{ W/m}^2\text{-K}$ for low air flowrate [184]), D is the diameter of fiber bundles ($\sim 0.5 \text{ mm}$ for single-component and $\sim 1.6 \text{ mm}$ for bi-component fibers), and k is the thermal conductivity of fibers (estimated $\sim 1 \text{ W/m-K}$ [34,96]). The Bi number is estimated to be about 0.005 for single component fibers (~ 0.016 for bi-component fibers), which indicates internal conductive resistance through conduction is much smaller than external convective resistance. Therefore, the solid fiber is uniformly heated.

Detailed analysis of the Joule heating process is shown below:

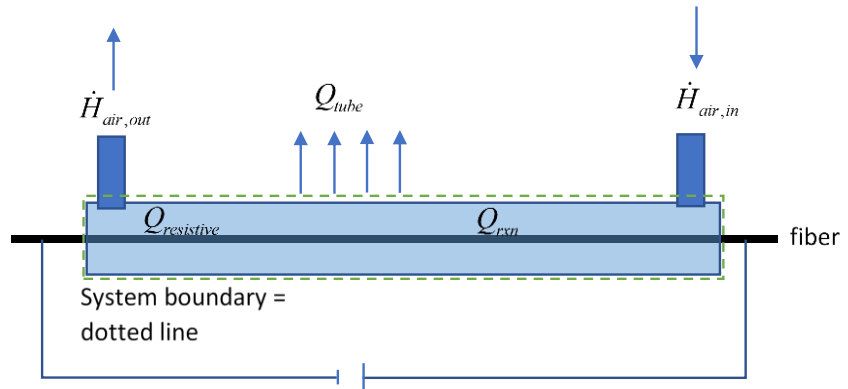


Figure E4. Schematic of an external macroscopic system.

Figure E4 shows the schematic of the macroscopic system. The total energy balance, including transient accumulation is the following:

$$[\text{Rate of Energy in} - \text{rate of Energy out}] + \text{Energy generation rate} = dE_{sys}/dt$$

The only energy streams that cross the system boundary are the current, the inlet air, outlet air, and the convective heat loss off of the quartz tube surface. In addition to the energy

and mass crossing the system boundary above there is internal heat generation inside the system through the following processes, including:

The heat generated by reactions of stabilization: Q_{rxn}

Heat generated by Joule heating of filaments: Q_{JH}

The dE_{sys}/dt is the rate of accumulation of energy in the system, which includes the fiber, the air, and the quartz tube, and any other parts within the system boundary.

$$\dot{H}_{air,in} - \dot{H}_{air,out} + Q_{tube} + Q_{rxn} + Q_{JH} = \frac{dE_{sys}}{dt} \quad (E-2)$$

$$-\Delta\dot{H}_{air} + Q_{tube} + Q_{rxn} + Q_{JH} = \frac{dE_{sys}}{dt} \quad (E-3)$$

The electrical conductivity of the PAN/CNT fibers likely increased during the Joule heating process, which was also shown in one previous study [3]. During the initial stage or transient period of Joule heating (15 ~ 30 minutes), the measured current value by a source meter increased gradually, and the current kept a steady state after the transient period. Thus, the analysis was separated into the transient period and the steady-state period.

During the transient period in the initial 30 minutes, Equation (E-3) becomes:

$$-\Delta\dot{H}_{air} + Q_{tube} + Q_{rxn} + Q_{JH} = \frac{dE_{sys}}{dt} \quad (E-4)$$

$$E_{sys} = E_{fiber} + E_{quartz} + E_{air} \quad (E-5)$$

$$= (mC_v\Delta T)_{fiber} + (mC_v\Delta T)_{quartz} + (mC_v\Delta T)_{air}$$

Where E_{fiber} , E_{quartz} , E_{air} , m , c_v , ΔT , are heat accumulation of fiber, tube, the air inside the tube mass, heat capacity, and temperature change. The enthalpy change of air inside the quartz tube (E_{air}) was ignored in the further calculation since the volume ($\sim 6 \times 10^{-4} \text{ m}^3$) and density of air ($< 1 \text{ kg/m}^3$ [184]) in the tube was quite small. The mass of fiber, the heat capacity of PAN fiber[185], and the temperature difference between the inlet (room temperature, 20°C) and average final temperature of fibers (250 °C) were used to calculate the E_{fiber} .

Moreover, the energy generated by the electric current was calculated by:

$$Q_{JH} = I * V \quad (E-6)$$

where \dot{m}_{air} , $c_{p,air}$, ΔT , t are flow rate of air during Joule heating (0.03 cfm), the average heat capacity of air (1 J/g-K), the average temperature difference between air inlet (room temperature, 20°C), air outlet (average temperature over time, 125 °C was used for calculation), and time of the Joule heating. Q_{rxn} was estimated from the DSC study (Figure S3). And Q_{tube} and $\frac{dE_{quartz}}{dt}$, which were energy loss to and heating up the tubes, were calculated through subtracting the $\frac{dE_{fiber}}{dt}$, $\Delta\dot{H}_{air}$ from the total energy generated Q_{JH} and Q_{rxn} .

During steady state after 30 minutes of Joule heating, the temperature of fiber and air became constant, then $dE_{sys}/dt = 0$. Equation (E-3) becomes:

$$-\Delta\dot{H}_{air} + Q_{tube} + Q_{rxn} + Q_{JH} = 0 \quad (\text{E-7})$$

Q_{JH} was calculated using Equation (E-6). using the measured current value in Table E2 and Table E3. $\Delta\dot{H}_{air}$ was calculated using Equation (E-7). The average temperature of the air outlet was about 230-240 °C during the steady state. Q_{rxn} was estimated from the DSC study (Figure E3), and Q_{tube} was calculated through subtracting the ΔH_{fiber} , $Q_{loss\ to\ convection\ air\ flow}$ from Q_{JH} and Q_{rxn} .

REFERENCES

- [1] M. Lewin, Handbook of Fiber Chemistry, CRC Press, 2006.
doi:10.1201/9781420015270.
- [2] S. Das, J. Warren, D. West, S.M. Schexnayder, Global Carbon Fiber Composites Supply Chain Competitiveness Analysis, 2016. www.osti.gov/scitech (accessed October 9, 2020).
- [3] V.B. Gupta and V.K. Kothari, Manufactured Fibre Technology, First Edit, Springer Science+Business Media Dordrecht, 1997. doi:10.1007/978-94-011-5854-1.
- [4] A.K. Gupta, D.K. Paliwal, P. Bajaj, Melting behavior of acrylonitrile polymers, J. Appl. Polym. Sci. (1998). doi:10.1002/(sici)1097-4628(19981226)70:13<2703::aid-app15>3.0.co;2-2.
- [5] B.G. Frushour, A new thermal analytical technique for acrylic polymers, Polym. Bull. 4 (1981) 305–314. doi:10.1007/BF00255108.
- [6] D. Grove, P. Desai, A.S. Abhiraman, Exploratory experiments in the conversion of plasticized melt spun PAN-based precursors to carbon fibers, Carbon N. Y. (1988). doi:10.1016/0008-6223(88)90233-3.
- [7] S. Francis, Fraunhofer presents melt-spinning technology for carbon fiber precursor manufacture, (2018).
<https://www.compositesworld.com/news/fraunhofer-presents-melt-spinning->

technology-for-carbon-fiber-precursor-manufacture (accessed October 20, 2020).

- [8] H. Chang, J. Luo, P. V. Gulgunje, S. Kumar, Structural and Functional Fibers, *Annu. Rev. Mater. Res.* 47 (2017) 331–359. doi:10.1146/annurev-matsci-120116-114326.
- [9] B. Qian, W. Lin, J. He, P. Hu, C. Wu, The Role of Macromolecular Entanglements in the Gel Spinning Process and Properties of High Performance Polyacrylonitrile Fibers, *J. Polym. Eng.* 15 (1995). doi:10.1515/polyeng.1995.15.3-4.327.
- [10] Y. Liu, H.G. Chae, S. Kumar, Gel-spun carbon nanotubes/polyacrylonitrile composite fibers. Part II: Stabilization reaction kinetics and effect of gas environment, *Carbon N. Y.* 49 (2011) 4477–4486.
doi:<https://doi.org/10.1016/j.carbon.2011.06.042>.
- [11] H.G. Chae, M.L. Minus, S. Kumar, Oriented and exfoliated single wall carbon nanotubes in polyacrylonitrile, *Polymer.* 47 (2006) 3494–3504.
doi:10.1016/j.polymer.2006.03.050.
- [12] H.G. Chae, B.A. Newcomb, P. V Gulgunje, Y. Liu, K.K. Gupta, M.G. Kamath, K.M. Lyons, S. Ghoshal, C. Pramanik, L. Giannuzzi, K. Şahin, I. Chasiotis, S. Kumar, High strength and high modulus carbon fibers, *Carbon N. Y.* 93 (2015) 81–87. doi:<https://doi.org/10.1016/j.carbon.2015.05.016>.
- [13] W. Du, H. Chen, Y. Xu, D. Pan, Constant rotational rheological behaviors of the PAN/DMSO/nonsolvent systems, *J. Appl. Polym. Sci.* 114 (2009) 598–602.
doi:10.1002/app.30568.

- [14] L. Tan, D. Pan, N. Pan, Rheological study on thermal-induced gelation behavior of polyacrylonitrile solution, *J. Polym. Res.* 16 (2009) 341–350. doi:10.1007/s10965-008-9234-y.
- [15] Y. Wang, W. Liu, G. Mo, R. Zhang, Rheological manifestation of the second self-similar structure in gelation process of PAN/DMSO/H₂O system, *Polymer*. 73 (2015) 149–155. doi:10.1016/j.polymer.2015.07.033.
- [16] M. Bercea, S. Morariu, C.-E. Brunchi, Rheological Investigation of Thermal-Induced Gelation of Polyacrylonitrile Solutions, *Int. J. Thermophys.* 30 (2009) 1411–1422. doi:10.1007/s10765-009-0637-8.
- [17] L. Tan, S. Liu, D. Pan, Water effect on the gelation behavior of polyacrylonitrile/dimethyl sulfoxide solution, *Colloids Surfaces A Physicochem. Eng. Asp.* 340 (2009) 168–173. doi:10.1016/j.colsurfa.2009.03.025.
- [18] W. Li, J. Hao, P. Zhou, Y. Liu, C. Lu, Z. Zhang, Solvent-solubility-parameter-dependent homogeneity and sol-gel transitions of concentrated polyacrylonitrile solutions, *J. Appl. Polym. Sci.* (2017) 45405. doi:10.1002/app.45405.
- [19] S. Arbab, P. Noorpanah, N. Mohammadi, M. Soleimani, Designing index of void structure and tensile properties in wet-spun polyacrylonitrile (PAN) fiber. I. Effect of dope polymer or nonsolvent concentration, *J. Appl. Polym. Sci.* 109 (2008) 3461–3469. doi:10.1002/app.28458.
- [20] H. Chen, W. Du, W. Ye, D. Pan, Structure of PAN precursor in thermal-induced gel spinning, *J. Appl. Polym. Sci.* 122 (2011) 1176–1181. doi:10.1002/app.34249.

- [21] J. Zhang, Y. Zhang, J. Zhao, Thermodynamic study of non-solvent/dimethyl sulfoxide/polyacrylonitrile ternary systems: effects of the non-solvent species, *Polym. Bull.* 67 (2011) 1073. doi:10.1007/s00289-011-0525-9.
- [22] S. Iijima, Helical microtubules of graphitic carbon, *Nature.* 354 (1991) 56. <http://dx.doi.org/10.1038/354056a0>.
- [23] E.T. Thostenson, Z. Ren, T.-W. Chou, Advances in the science and technology of carbon nanotubes and their composites: a review, *Compos. Sci. Technol.* 61 (2001) 1899–1912. doi:10.1016/S0266-3538(01)00094-X.
- [24] M. Moniruzzaman, K.I. Winey, Polymer Nanocomposites Containing Carbon Nanotubes, *Macromolecules.* 39 (2006) 5194–5205. doi:10.1021/ma060733p.
- [25] M. Miao, Electrical conductivity of pure carbon nanotube yarns, *Carbon N. Y.* 49 (2011) 3755–3761. doi:10.1016/j.carbon.2011.05.008.
- [26] R. Ramasubramaniam, J. Chen, H. Liu, Homogeneous carbon nanotube/polymer composites for electrical applications, *Appl. Phys. Lett.* 83 (2003) 2928–2930. doi:10.1063/1.1616976.
- [27] R.H. Baughman, A.A. Zakhidov, W.A. de Heer, Carbon Nanotubes--the Route Toward Applications, *Science (80-.).* 297 (2002) 787–792. doi:10.1126/science.1060928.
- [28] J.B. Bai, A. Allaoui, Effect of the length and the aggregate size of MWNTs on the improvement efficiency of the mechanical and electrical properties of

- nanocomposites—experimental investigation, *Compos. Part A Appl. Sci. Manuf.* 34 (2003) 689–694. doi:10.1016/S1359-835X(03)00140-4.
- [29] F. Du, J.E. Fischer, K.I. Winey, Effect of nanotube alignment on percolation conductivity in carbon nanotube/polymer composites, *Phys. Rev. B.* 72 (2005) 121404. doi:10.1103/PhysRevB.72.121404.
- [30] J.Z. Kovacs, B.S. Velagala, K. Schulte, W. Bauhofer, Two percolation thresholds in carbon nanotube epoxy composites, *Compos. Sci. Technol.* (2007). doi:10.1016/j.compscitech.2006.02.037.
- [31] B. Bryning, F. Islam M, M. Kikkawa J, G. Yodh A, Very Low Conductivity Threshold in Bulk Isotropic Single-Walled Carbon Nanotube–Epoxy Composites, *Adv. Mater.* 17 (n.d.) 1186–1191. doi:10.1002/adma.200401649.
- [32] M. Horio, T. Kondo, Crimping of Wool Fibers, *Text. Res. J.* 23 (1953) 373–386. doi:10.1177/004051755302300601.
- [33] 1965 Du Pont Vintage Ad “Cantrece,” (n.d.). <https://www.vintage-adventures.com/vintage-clothing-shoe-accessory-ads/4436-1965-du-pont-ad-cantrece.html> (accessed October 9, 2020).
- [34] A.T. Chien, P. V. Gulgunje, H.G. Chae, A.S. Joshi, J. Moon, B. Feng, G.P. Peterson, S. Kumar, Functional polymer-polymer/carbon nanotube bi-component fibers, *Polymer.* 54 (2013) 6210–6217. doi:10.1016/j.polymer.2013.08.061.
- [35] R. Jeffries, *Bicomponent fibres*, Watford, Merrow Publishing Co. Ltd, 1971.

<https://catalogue.nla.gov.au/Record/392405> (accessed October 9, 2020).

- [36] Y. Liu, F. Tovia, J. John D. Pierce, Consumer Acceptability of Scent-infused Knitting Scarves Using Functional Melt-spun PP/PLA Bicomponent Fibers, *Text. Res. J.* 79 (2009) 566–573. doi:10.1177/0040517508094397.
- [37] M. Bognitzki, H. Hou, M. Ishaque, T. Frese, M. Hellwig, C. Schwarte, A. Schaper, J.H. Wendorff, A. Greiner, Polymer, metal, and hybrid nano- and mesotubes by coating degradable polymer template fibers (TUFT process), *Adv. Mater.* 12 (2000) 637–640. doi:10.1002/(SICI)1521-4095(200005)12:9<637::AID-ADMA637>3.0.CO;2-W.
- [38] M. Naeimirad, A. Zadhoush, R. Kotek, R. Esmaeely Neisiany, S. Nouri Khorasani, S. Ramakrishna, Recent advances in core/shell bicomponent fibers and nanofibers: A review, *J. Appl. Polym. Sci.* 135 (2018) 46265. doi:10.1002/app.46265.
- [39] S. Mazinani, A. Ajji, C. Dubois, Structure and properties of melt-spun PET/MWCNT nanocomposite fibers, *Polym. Eng. Sci.* 50 (2010) 1956–1968. doi:10.1002/pen.21727.
- [40] S.S. Ojha, D.R. Stevens, K. Stano, T. Hoffman, L.I. Clarke, R.E. Gorga, Characterization of Electrical and Mechanical Properties for Coaxial Nanofibers with Poly(ethylene oxide) (PEO) Core and Multiwalled Carbon Nanotube/PEO Sheath, *Macromolecules.* 41 (2008) 2509–2513. doi:10.1021/ma702634a.
- [41] M. Miyauchi, J. Miao, T.J. Simmons, J.-W. Lee, T. V Doherty, J.S. Dordick, R.J. Linhardt, Conductive Cable Fibers with Insulating Surface Prepared by Coaxial

Electrospinning of Multiwalled Nanotubes and Cellulose, *Biomacromolecules*. 11 (2010) 2440–2445. doi:10.1021/bm1006129.

- [42] M. Strååt, M. Rigdahl, B. Hagström, Conducting bicomponent fibers obtained by melt spinning of PA6 and polyolefins containing high amounts of carbonaceous fillers, *J. Appl. Polym. Sci.* 123 (2012) 936–943. doi:10.1002/app.34539.
- [43] T.J. Longson, R. Bhowmick, C. Gu, B.A. Cruden, Core–Shell Interactions in Coaxial Electrospinning and Impact on Electrospun Multiwall Carbon Nanotube Core, Poly(methyl methacrylate) Shell Fibers, *J. Phys. Chem. C*. 115 (2011) 12742–12750. doi:10.1021/jp201077p.
- [44] B. Glauß, W. Steinmann, S. Walter, M. Beckers, G. Seide, T. Gries, G. Roth, Spinnability and characteristics of polyvinylidene fluoride (PVDF)-based bicomponent fibers with a carbon nanotube (CNT) modified polypropylene core for piezoelectric applications, *Materials (Basel)*. 6 (2013) 2642–2661. doi:10.3390/ma6072642.
- [45] Z. Tang, S. Jia, F. Wang, C. Bian, Y. Chen, Y. Wang, B. Li, Highly Stretchable Core–Sheath Fibers via Wet-Spinning for Wearable Strain Sensors, *ACS Appl. Mater. Interfaces*. 10 (2018) 6624–6635. doi:10.1021/acsami.7b18677.
- [46] W. Bauhofer, J.Z. Kovacs, A review and analysis of electrical percolation in carbon nanotube polymer composites, *Compos. Sci. Technol.* 69 (2009) 1486–1498. doi:10.1016/j.compscitech.2008.06.018.
- [47] P. Sunthar, Polymer rheology, in: *Rheol. Complex Fluids*, Springer New York,

New York, NY, 2010: pp. 171–191. doi:10.1007/978-1-4419-6494-6_8.

- [48] P. Pötschke, T.D. Fornes, D.R. Paul, Rheological behavior of multiwalled carbon nanotube/polycarbonate composites, *Polymer*. 43 (2002) 3247–3255.
doi:10.1016/S0032-3861(02)00151-9.
- [49] F. Du, R.C. Scogna, W. Zhou, S. Brand, J.E. Fischer, K.I. Winey, Nanotube networks in polymer nanocomposites: Rheology and electrical conductivity, *Macromolecules*. (2004). doi:10.1021/ma049164g.
- [50] P. Pötschke, M. Abdel-Goad, I. Alig, S. Dudkin, D. Lellinger, Rheological and dielectrical characterization of melt mixed polycarbonate-multiwalled carbon nanotube composites, *Polymer*. 45 (2004) 8863–8870.
doi:10.1016/j.polymer.2004.10.040.
- [51] S.C. Mun, M. Kim, K. Prakashan, H.J. Jung, Y. Son, O.O. Park, A new approach to determine rheological percolation of carbon nanotubes in microstructured polymer matrices, *Carbon N. Y.* (2014). doi:10.1016/j.carbon.2013.09.056.
- [52] R.J. Moon, A. Martini, J. Nairn, J. Simonsen, J. Youngblood, Cellulose nanomaterials review: structure, properties and nanocomposites, *Chem. Soc. Rev.* 40 (2011) 3941. doi:10.1039/c0cs00108b.
- [53] H. Chang, J. Luo, H.C. Liu, A.A. Bakhtiary Davijani, P.-H. Wang, G.S. Lolov, R.M. Dwyer, S. Kumar, Ductile polyacrylonitrile fibers with high cellulose nanocrystals loading, *Polymer*. 122 (2017) 332–339.
doi:10.1016/j.polymer.2017.06.072.

- [54] J. Luo, H. Chang, A.A. Bakhtiary Davijani, H.C. Liu, P.-H. Wang, R.J. Moon, S. Kumar, Influence of high loading of cellulose nanocrystals in polyacrylonitrile composite films, *Cellulose*. 24 (2017) 1745–1758. doi:10.1007/s10570-017-1219-8.
- [55] K.M. Yearsley, M.R. Mackley, F. Chinesta, A. Leygue, The rheology of multiwalled carbon nanotube and carbon black suspensions, *J. Rheol.* (N. Y. N. Y). (2012). doi:10.1122/1.4751871.
- [56] K. Lakdawala, R. Salovey, Rheology of polymers containing carbon black, *Polym. Eng. Sci.* (1987). doi:10.1002/pen.760271403.
- [57] X. Zhang, J. Liu, Y. Wang, W. Wu, Effect of polyamide 6 on the morphology and electrical conductivity of carbon black-filled polypropylene composites, *R. Soc. Open Sci.* (2017). doi:10.1098/rsos.170769.
- [58] C. Gao, S. Zhang, F. Wang, B. Wen, C. Han, Y. Ding, M. Yang, Graphene networks with low percolation threshold in abs nanocomposites: Selective localization and electrical and rheological properties, *ACS Appl. Mater. Interfaces*. (2014). doi:10.1021/am501843s.
- [59] K. Liu, E. Andablo-Reyes, N. Patil, D.H. Merino, S. Ronca, S. Rastogi, Influence of reduced graphene oxide on the rheological response and chain orientation on shear deformation of high density polyethylene, *Polymer* . (2016). doi:10.1016/j.polymer.2016.01.056.
- [60] A.P. Isfahani, M. Mehrabzadeh, J. Morshedian, The effects of processing and

using different types of clay on the mechanical, thermal and rheological properties of high-impact polystyrene nanocomposites, *Polym. J.* (2013).

doi:10.1038/pj.2012.138.

- [61] K.Q. Xiao, L.C. Zhang, I. Zarudi, Mechanical and rheological properties of carbon nanotube-reinforced polyethylene composites, *Compos. Sci. Technol.* (2007).

doi:10.1016/j.compscitech.2006.07.027.

- [62] Q. Zhang, D.R. Lippits, S. Rastogi, Dispersion and rheological aspects of SWNTs in ultrahigh molecular weight polyethylene, *Macromolecules.* (2006).

doi:10.1021/ma051031n.

- [63] K. Menzer, B. Krause, R. Boldt, B. Kretzschmar, R. Weidisch, P. Pötschke, Percolation behaviour of multiwalled carbon nanotubes of altered length and primary agglomerate morphology in melt mixed isotactic polypropylene-based composites, *Compos. Sci. Technol.* (2011).

doi:10.1016/j.compscitech.2011.09.009.

- [64] P.J. Arias-Monje, M. Lu, J. Ramachandran, M.H. Kirmani, S. Kumar, Processing, structure and properties of polyacrylonitrile fibers with 15 weight percent single wall carbon nanotubes, *Polymer* . (2020). doi:10.1016/j.polymer.2020.123065.

- [65] M.S.A. Rahaman, A.F. Ismail, A. Mustafa, A review of heat treatment on polyacrylonitrile fiber, *Polym. Degrad. Stab.* 92 (2007) 1421–1432.

doi:10.1016/j.polymdegradstab.2007.03.023.

- [66] J.W. Johnson, W. Potter, P.G. Rose, G. Scott, Stabilization of polyacrylonitrile by

oxidative transformation, *Br. Polym. J.* (1972). doi:10.1002/pi.4980040606.

- [67] L. Chen, Z. Shen, J. Liu, J. Liang, X. Wang, Effects of oxygen on the structural evolution of polyacrylonitrile fibers during rapid thermal treatment, *RSC Adv.* (2020). doi:10.1039/c9ra08881d.
- [68] W. WATT, W. JOHNSON, Mechanism of oxidation of polyacrylonitrile fibres, *Nature.* 257 (1975) 210–212. doi:10.1038/257210a0.
- [69] X. Huang, Fabrication and Properties of Carbon Fibers, *Materials (Basel).* 2 (2009) 2369–2403. doi:10.3390/ma2042369.
- [70] E. Fitzer, D.J. Müller, The influence of oxygen on the chemical reactions during stabilization of pan as carbon fiber precursor, *Carbon N. Y.* 13 (1975) 63–69. doi:10.1016/0008-6223(75)90259-6.
- [71] H.C. Liu, A.T. Chien, B.A. Newcomb, A.A. Bakhtiary Davijani, S. Kumar, Stabilization kinetics of gel spun polyacrylonitrile/lignin blend fiber, *Carbon N. Y.* 101 (2016) 382–389. doi:10.1016/j.carbon.2016.01.096.
- [72] J. Luo, H. Chang, P.H. Wang, R.J. Moon, S. Kumar, Cellulose nanocrystals effect on the stabilization of polyacrylonitrile composite films, *Carbon N. Y.* 134 (2018) 92–102. doi:10.1016/j.carbon.2018.03.078.
- [73] T. -H Ko, H. -Y Ting, C. -H Lin, Thermal stabilization of polyacrylonitrile fibers, *J. Appl. Polym. Sci.* 35 (1988) 631–640. doi:10.1002/app.1988.070350306.
- [74] A. Shiedlin, G. Marom, A. Zilkha, Catalytic initiation of polyacrylonitrile

stabilization, *Polymer* . 26 (1985) 447–451. doi:10.1016/0032-3861(85)90210-1.

- [75] US3656882A - ACRYLIC FIBER STABILIZATION CATALYZED BY Co(II) AND Ce(III) CATIONS - Google Patents, (n.d).
<https://patents.google.com/patent/US3656882> (accessed October 23, 2019).
- [76] S.B. Warner, L.H. Peebles, D.R. Uhlmann, Oxidative stabilization of acrylic fibres, *J. Mater. Sci.* 14 (1979) 556–564. doi:10.1007/BF00772714.
- [77] David Warren, *Lower Cost Carbon Fiber Precursors*, 2010.
https://www.energy.gov/sites/prod/files/2014/03/f11/lm004_warren_2010_o.pdf
(accessed August 26, 2019).
- [78] F.L. Paulauskas, K.D. Yarborough, O. Ridge, T.T. Meek, US 6,372,192 B1 CARBON FIBER MANUFACTURING VIA PLASMA TECHNOLOGY, US006372192B1, 2002.
- [79] Z. Han, A. Fina, Thermal conductivity of carbon nanotubes and their polymer nanocomposites: A review, *Prog. Polym. Sci.* 36 (2011) 914–944.
doi:10.1016/j.progpolymsci.2010.11.004.
- [80] C. Huang, X. Qian, R. Yang, Thermal conductivity of polymers and polymer nanocomposites, *Mater. Sci. Eng. R Reports.* 132 (2018) 1–22.
doi:10.1016/j.mser.2018.06.002.
- [81] B.A. Newcomb, Processing, structure, and properties of carbon fibers, *Compos. Part A Appl. Sci. Manuf.* 91 (2016) 262–282.

doi:10.1016/j.compositesa.2016.10.018.

- [82] This Month Physics History: December 1840: Joule's abstract on converting mechanical power into heat, *APS News Arch.* 18 (2009).
<https://www.aps.org/publications/apsnews/200912/physicshistory.cfm> (accessed November 24, 2019).
- [83] J. Park, Functional fibers, composites and textiles utilizing photothermal and joule heating, *Polymers.* (2020). doi:10.3390/polym12010189.
- [84] S. Hong, H. Lee, J. Lee, J. Kwon, S. Han, Y.D. Suh, H. Cho, J. Shin, J. Yeo, S.H. Ko, Highly Stretchable and Transparent Metal Nanowire Heater for Wearable Electronics Applications, *Adv. Mater.* (2015). doi:10.1002/adma.201500917.
- [85] H. Wang, S. Lin, D. Zu, J. Song, Z. Liu, L. Li, C. Jia, X. Bai, J. Liu, Z. Li, D. Wang, Y. Huang, M. Fang, M. Lei, B. Li, H. Wu, Direct Blow Spinning of Flexible and Transparent Ag Nanofiber Heater, *Adv. Mater. Technol.* (2019). doi:10.1002/admt.201900045.
- [86] Y. Cheng, H. Zhang, R. Wang, X. Wang, H. Zhai, T. Wang, Q. Jin, J. Sun, Highly Stretchable and Conductive Copper Nanowire Based Fibers with Hierarchical Structure for Wearable Heaters, *ACS Appl. Mater. Interfaces.* (2016). doi:10.1021/acsami.6b09293.
- [87] Y. Wang, Z. Yu, G. Mao, Y. Liu, G. Liu, J. Shang, S. Qu, Q. Chen, R.W. Li, Printable Liquid-Metal@PDMS Stretchable Heater with High Stretchability and Dynamic Stability for Wearable Thermo-therapy, *Adv. Mater. Technol.* (2019).

doi:10.1002/admt.201800435.

- [88] Q. Liu, J. Huang, J. Zhang, Y. Hong, Y. Wan, Q. Wang, M. Gong, Z. Wu, C.F. Guo, Thermal, Waterproof, Breathable, and Antibacterial Cloth with a Nanoporous Structure, *ACS Appl. Mater. Interfaces*. (2018). doi:10.1021/acsami.7b16422.
- [89] S.H. Jang, Y.L. Park, Carbon nanotube-reinforced smart composites for sensing freezing temperature and deicing by self-heating, *Nanomater. Nanotechnol.* (2018). doi:10.1177/1847980418776473.
- [90] R. Wang, Z. Xu, J. Zhuang, Z. Liu, L. Peng, Z. Li, Y. Liu, W. Gao, C. Gao, Highly Stretchable Graphene Fibers with Ultrafast Electrothermal Response for Low-Voltage Wearable Heaters, *Adv. Electron. Mater.* (2017). doi:10.1002/aelm.201600425.
- [91] S.G. Prolongo, R. Moriche, A. Jiménez-Suárez, A. Delgado, A. Ureña, Printable self-heating coatings based on the use of carbon nanoreinforcements, *Polym. Compos.* (2020). doi:10.1002/pc.25367.
- [92] H. Chu, Z. Zhang, Y. Liu, J. Leng, Self-heating fiber reinforced polymer composite using meso/macropore carbon nanotube paper and its application in deicing, *Carbon N. Y.* (2014). doi:10.1016/j.carbon.2013.08.053.
- [93] B. Mas, J.P. Fernández-Blázquez, J. Duval, H. Bunyan, J.J. Vilatela, Thermoset curing through Joule heating of nanocarbons for composite manufacture, repair and soldering, *Carbon N. Y.* (2013). doi:10.1016/j.carbon.2013.07.029.

- [94] X. Xu, Y. Zhang, J. Jiang, H. Wang, X. Zhao, Q. Li, W. Lu, In-situ curing of glass fiber reinforced polymer composites via resistive heating of carbon nanotube films, *Compos. Sci. Technol.* (2017). doi:10.1016/j.compscitech.2017.06.001.
- [95] S.H. Noh, W. Eom, W.J. Lee, H. Park, S.B. Ambade, S.O. Kim, T.H. Han, Joule heating-induced sp²-restoration in graphene fibers, *Carbon N. Y.* (2019). doi:10.1016/j.carbon.2018.10.041.
- [96] A.-T. Chien, S. Cho, Y. Joshi, S. Kumar, Electrical conductivity and Joule heating of polyacrylonitrile/carbon nanotube composite fibers, *Polymer*. 55 (2014) 6896–6905. doi:10.1016/j.polymer.2014.10.064.
- [97] D.R. Paul, A study of spinnability in the wet-spinning of acrylic fibers, *J. Appl. Polym. Sci.* 12 (1968) 2273–2298. doi:10.1002/app.1968.070121006.
- [98] A. Ziabicki, R. Takserman-Krozer, Mechanism of breakage of liquid threads, *Kolloid-Zeitschrift Und Zeitschrift Für Polym.* 198 (1964) 60–65. doi:10.1007/BF01499455.
- [99] A. Ziabicki, R. Takserman-Krozer, Effect of rheological factors on the length of liquid threads, *Kolloid-Zeitschrift Zeitschrift Für Polym.* 199 (1964) 9–13. doi:10.1007/BF01499686.
- [100] C.D. Han, A theoretical study on fiber spinnability, *Rheol. Acta.* 9 (1970) 355–365. doi:10.1007/BF01975402.
- [101] Y. Ide, J.L. White, The spinnability of polymer fluid filaments, *J. Appl. Polym.*

Sci. 20 (1976) 2511–2531. doi:10.1002/app.1976.070200919.

- [102] J. Wang, T. Wang, J. Xu, J. Yu, Y. Zhang, H. Wang, Study on spinnability of polyacrylonitrile solution based on dynamics simulation of dry-jet wet spinning, *J. Appl. Polym. Sci.* 135 (2018) 46377. doi:10.1002/app.46377.
- [103] Q. Liu, Y. Wang, F. Niu, L. Ma, C. Qu, S. Fu, M. Chen, Spinnability of Polyacrylonitrile Gel Dope in the Mixed Solvent of Dimethyl Sulfoxide/Dimethylacetamide and Characterization of the Nascent Fibers, *Polym. Sci. Ser. A.* 60 (2018) 638–646. doi:10.1134/S0965545X18050103.
- [104] E.A. Morris, M.C. Weisenberger, S.B. Bradley, M.G. Abdallah, S.J. Mecham, P. Pisipati, J.E. McGrath, Synthesis, spinning, and properties of very high molecular weight poly(acrylonitrile-co-methyl acrylate) for high performance precursors for carbon fiber, *Polymer* . 55 (2014) 6471–6482. doi:10.1016/j.polymer.2014.10.029.
- [105] R. Jain, Carbon Nanotube Reinforced Polyacrylonitrile and Poly(etherketone) Fibers, Georgia Institute of Technology, 2009.
- [106] P.-H. Wang, S. Sarkar, P. Gulgunje, N. Verghese, S. Kumar, Structure and rheological behavior of polypropylene interphase at high carbon nanotube concentration, *Polymer*. 150 (2018) 10–25. doi:10.1016/j.polymer.2018.06.050.
- [107] J. Sato, V. Breedveld, Evaporation Blocker for Cone-Plate Rheometry of Volatile Samples, *Appl. Rheol.* 15 (2005) 390–397. doi:10.1515/arh-2005-0019.
- [108] P. Pötschke, T.D. Fornes, D.R. Paul, Rheological behavior of multiwalled carbon

nanotube/polycarbonate composites, *Polymer*. 43 (2002) 3247–3255.

doi:10.1016/S0032-3861(02)00151-9.

[109] Q. Zhang, F. Fang, X. Zhao, Y. Li, M. Zhu, D. Chen, Use of dynamic rheological behavior to estimate the dispersion of carbon nanotubes in carbon

nanotube/polymer composites, *J. Phys. Chem. B*. 112 (2008) 12606–12611.

doi:10.1021/jp802708j.

[110] A.W.K. Ma, K.M. Yearsley, F. Chinesta, M.R. MacKley, A review of the

microstructure and rheology of carbon nanotube suspensions, *Proc. Inst. Mech.*

Eng. Part N J. Nanoeng. Nanosyst. 222 (2008) 71–94.

doi:10.1243/17403499JNN153.

[111] M.R. Nobile, Rheology of polymer-carbon nanotube composites melts, in: *Polym.*

Nanotub. Compos. Prep. Prop. Appl., Woodhead Publishing, 2011: pp. 428–481.

doi:10.1533/9780857091390.2.428.

[112] H.C. Liu, C.-C. Tuan, A.A. Bakhtiary Davijani, P.-H. Wang, H. Chang, C.-P.

Wong, S. Kumar, Rheological behavior of polyacrylonitrile and

polyacrylonitrile/lignin blends, *Polymer*. 111 (2017) 177–182.

doi:10.1016/j.polymer.2017.01.043.

[113] T. Chatterjee, R. Krishnamoorti, Steady Shear Response of Carbon Nanotube

Networks Dispersed in Poly(ethylene oxide), *Macromolecules*. 41 (2008) 5333–

5338. doi:10.1021/ma800640w.

[114] C.D. Han, J. Kim, J.K. Kim, Determination of the order-disorder transition

temperature of block copolymers, *Macromolecules*. 22 (1989) 383–394.
doi:10.1021/ma00191a071.

[115] H.-K. Chuang, C.D. Han, Rheological behavior of polymer blends, *J. Appl. Polym. Sci.* 29 (1984) 2205–2229. doi:10.1002/app.1984.070290625.

[116] B.A. Newcomb, P. V Gulgunje, Y. Liu, K. Gupta, M.G. Kamath, C. Pramanik, S. Ghoshal, H.G. Chae, S. Kumar, Polyacrylonitrile solution homogeneity study by dynamic shear rheology and the effect on the carbon fiber tensile strength, *Polym. Eng. Sci.* 56 (2016) 361–370. doi:10.1002/pen.24261.

[117] Y. Liu, S. Kumar, Polymer/Carbon Nanotube Nano Composite Fibers—A Review, *ACS Appl. Mater. Interfaces*. 6 (2014) 6069–6087. doi:10.1021/am405136s.

[118] F. Faridirad, S. Ahmadi, M. Barmar, Polyamide/Carbon Nanoparticles Nanocomposites: A Review, *Polym. Eng. Sci.* 57 (2017) 475–494.
doi:10.1002/pen.24444.

[119] R. Jain, Y.H. Choi, Y. Liu, M.L. Minus, H.G. Chae, S. Kumar, J.-B. Baek, Processing, structure and properties of poly(ether ketone) grafted few wall carbon nanotube composite fibers, *Polymer*. 51 (2010) 3940–3947.
doi:10.1016/J.POLYMER.2010.06.034.

[120] P. Wang, P. Gulgunje, S. Ghoshal, N. Verghese, S. Kumar, Rheological behavior of polypropylene nanocomposites with tailored polymer/multiwall carbon nanotubes interface, *Polym. Eng. Sci.* 59 (2019) 1763–1777.
doi:10.1002/pen.25176.

- [121] P. Wang, P. Gulgunje, S. Ghoshal, I.N. Odeh, N. Verghese, S. Kumar, Effect of interfacial chemistry on crystallization of polypropylene/multiwall carbon nanotube nanocomposites, *Polym. Eng. Sci.* 59 (2019) 1570–1584. doi:10.1002/pen.25155.
- [122] R. Arrigo, R. Teresi, C. Gambarotti, F. Parisi, G. Lazzara, N.T. Dintcheva, Sonication-induced modification of carbon nanotubes: Effect on the rheological and thermo-oxidative behaviour of polymer-based nanocomposites, *Materials (Basel)*. 11 (2018). doi:10.3390/ma11030383.
- [123] C.J. Kerr, Y.Y. Huang, J.E. Marshall, E.M. Terentjev, Effect of filament aspect ratio on the dielectric response of multiwalled carbon nanotube composites, *J. Appl. Phys.* 109 (2011) 94109. doi:10.1063/1.3569596.
- [124] Y.Y. Huang, T.P.J. Knowles, E.M. Terentjev, Strength of Nanotubes, Filaments, and Nanowires From Sonication-Induced Scission, *Adv. Mater.* 21 (2009) 3945–3948. doi:10.1002/adma.200900498.
- [125] A.-T. Chien, B.A. Newcomb, D. Sabo, J. Robbins, Z.J. Zhang, S. Kumar, High-strength superparamagnetic composite fibers, *Polymer*. 55 (2014) 4116–4124. doi:http://dx.doi.org/10.1016/j.polymer.2014.06.028.
- [126] T. V Sreekumar, T. Liu, B.G. Min, H. Guo, S. Kumar, R.H. Hauge, R.E. Smalley, Polyacrylonitrile Single-Walled Carbon Nanotube Composite Fibers, *Adv. Mater.* 16 (2004) 58–61. doi:10.1002/adma.200305456.
- [127] T. Liu, S. Kumar, Quantitative characterization of SWNT orientation by polarized

Raman spectroscopy, *Chem. Phys. Lett.* 378 (2003) 257–262.

doi:[https://doi.org/10.1016/S0009-2614\(03\)01287-9](https://doi.org/10.1016/S0009-2614(03)01287-9).

- [128] H. Chang, J. Luo, H.C. Liu, A.A.B. Davijani, P.-H. Wang, S. Kumar, Orientation and interfacial stress transfer of cellulose nanocrystal nanocomposite fibers, *Polymer*. 110 (2017) 228–234. doi:<https://doi.org/10.1016/j.polymer.2017.01.015>.
- [129] H.G. Chae, T. V. Sreekumar, T. Uchida, S. Kumar, A comparison of reinforcement efficiency of various types of carbon nanotubes in polyacrylonitrile fiber, *Polymer*. 46 (2005) 10925–10935. doi:[10.1016/j.polymer.2005.08.092](https://doi.org/10.1016/j.polymer.2005.08.092).
- [130] J. Rahul, M.M. L., C.H. Gi, K. Satish, Processing, Structure, and Properties of PAN/MWNT Composite Fibers, *Macromol. Mater. Eng.* 295 (2010) 742–749. doi:[10.1002/mame.201000083](https://doi.org/10.1002/mame.201000083).
- [131] I. Balberg, N. Binenbaum, N. Wagner, Percolation thresholds in the three-dimensional sticks system, *Phys. Rev. Lett.* 52 (1984) 1465–1468. doi:[10.1103/PhysRevLett.52.1465](https://doi.org/10.1103/PhysRevLett.52.1465).
- [132] A. V. Kyrylyuk, P. Van Der Schoot, Continuum percolation of carbon nanotubes in polymeric and colloidal media, *Proc. Natl. Acad. Sci. U. S. A.* 105 (2008) 8221–8226. doi:[10.1073/pnas.0711449105](https://doi.org/10.1073/pnas.0711449105).
- [133] I. Alig, P. Pötschke, D. Lellinger, T. Skipa, S. Pegel, G.R. Kasaliwal, T. Villmow, Establishment, morphology and properties of carbon nanotube networks in polymer melts, *Polymer*. 53 (2012) 4–28. doi:[10.1016/j.polymer.2011.10.063](https://doi.org/10.1016/j.polymer.2011.10.063).

- [134] I. Balberg, N. Binenbaum, Computer study of the percolation threshold in a two-dimensional anisotropic system of conducting sticks, *Phys. Rev. B.* 28 (1983) 3799–3812. doi:10.1103/PhysRevB.28.3799.
- [135] S.H. Munson-McGee, Estimation of the critical concentration in an anisotropic percolation network, *Phys. Rev. B.* 43 (1991) 3331–3336. doi:10.1103/PhysRevB.43.3331.
- [136] R. Zhang, A. Dowden, H. Deng, M. Baxendale, T. Peijs, Conductive network formation in the melt of carbon nanotube/thermoplastic polyurethane composite, *Compos. Sci. Technol.* 69 (2009) 1499–1504. doi:10.1016/j.compscitech.2008.11.039.
- [137] H. Deng, E. Bilotti, R. Zhang, J. Loos, T. Peijs, Effect of thermal annealing on the electrical conductivity of high-strength bicomponent polymer tapes containing carbon nanofillers, *Synth. Met.* 160 (2010) 337–344. doi:10.1016/j.synthmet.2009.11.001.
- [138] P. Miaudet, C. Bartholome, A. Derré, M. Maugey, G. Sigaud, C. Zakri, P. Poulin, Thermo-electrical properties of PVA-nanotube composite fibers, *Polymer.* 48 (2007) 4068–4074. doi:10.1016/j.polymer.2007.05.028.
- [139] Y. Liu, Y.H. Choi, H.G. Chae, P. Gulgunje, S. Kumar, Temperature dependent tensile behavior of gel-spun polyacrylonitrile and polyacrylonitrile/carbon nanotube composite fibers, *Polymer.* 54 (2013) 4003–4009. doi:https://doi.org/10.1016/j.polymer.2013.05.051.

- [140] M. Arjmand, M. Mahmoodi, G.A. Gelves, S. Park, U. Sundararaj, Electrical and electromagnetic interference shielding properties of flow-induced oriented carbon nanotubes in polycarbonate, *Carbon N. Y.* 49 (2011) 3430–3440. doi:10.1016/j.carbon.2011.04.039.
- [141] G. Pandey, E.T. Thostenson, Carbon Nanotube-Based Multifunctional Polymer Nanocomposites, *Polym. Rev.* 52 (2012) 355–416. doi:10.1080/15583724.2012.703747.
- [142] K.J. Loh, J. Kim, J.P. Lynch, N.W.S. Kam, N.A. Kotov, Multifunctional layer-by-layer carbon nanotube–polyelectrolyte thin films for strain and corrosion sensing, *Smart Mater. Struct.* 16 (2007) 429–438. doi:10.1088/0964-1726/16/2/022.
- [143] M. Park, H. Kim, J.P. Youngblood, Strain-dependent electrical resistance of multi-walled carbon nanotube/polymer composite films, *Nanotechnology.* 19 (2008) 055705. doi:10.1088/0957-4484/19/05/055705.
- [144] N. Hu, Y. Karube, M. Arai, T. Watanabe, C. Yan, Y. Li, Y. Liu, H. Fukunaga, Investigation on sensitivity of a polymer/carbon nanotube composite strain sensor, *Carbon N. Y.* 48 (2010) 680–687. doi:10.1016/j.carbon.2009.10.012.
- [145] S. V Anand, D. Roy Mahapatra, Quasi-static and dynamic strain sensing using carbon nanotube/epoxy nanocomposite thin films, *Smart Mater. Struct.* 18 (2009) 045013. doi:10.1088/0964-1726/18/4/045013.
- [146] G.T. Pham, Y.-B. Park, Z. Liang, C. Zhang, B. Wang, Processing and modeling of conductive thermoplastic/carbon nanotube films for strain sensing, *Compos. Part B*

Eng. 39 (2008) 209–216. doi:10.1016/J.COMPOSITESB.2007.02.024.

- [147] M.H.G. Wichmann, S.T. Buschhorn, L. Böger, R. Adelong, K. Schulte, Direction sensitive bending sensors based on multi-wall carbon nanotube/epoxy nanocomposites, *Nanotechnology*. 19 (2008) 475503. doi:10.1088/0957-4484/19/47/475503.
- [148] R.K. Srivastava, V.S.M. Vemuru, Y. Zeng, R. Vajtai, S. Nagarajiah, P.M. Ajayan, A. Srivastava, The strain sensing and thermal–mechanical behavior of flexible multi-walled carbon nanotube/polystyrene composite films, *Carbon N. Y.* 49 (2011) 3928–3936. doi:10.1016/j.carbon.2011.05.031.
- [149] N. Yusof, A.F. Ismail, Polyacrylonitrile/acrylamide-based carbon fibers prepared using a solvent-free coagulation process: Fiber properties and its structure evolution during stabilization and carbonization, *Polym. Eng. Sci.* 52 (2012) 360–366. doi:10.1002/pen.22090.
- [150] M.K. Jain, A.S. Abhiraman, Conversion of acrylonitrile-based precursor fibres to carbon fibres, *J. Mater. Sci.* 22 (1987) 278–300. doi:10.1007/BF01160584.
- [151] M. Ji, C. Wang, Y. Bai, M. Yu, Y. Wang, Structural Evolution of Polyacrylonitrile Precursor Fibers during Preoxidation and Carbonization, *Polym. Bull.* 59 (2007) 527–536. doi:10.1007/s00289-007-0796-3.
- [152] H.G. Chae, M.L. Minus, A. Rasheed, S. Kumar, Stabilization and carbonization of gel spun polyacrylonitrile/single wall carbon nanotube composite fibers, *Polymer*. 48 (2007) 3781–3789. doi:10.1016/j.polymer.2007.04.072.

- [153] E. Fitzer, W. Frohs, M. Heine, Optimization of stabilization and carbonization treatment of PAN fibres and structural characterization of the resulting carbon fibres, *Carbon N. Y.* 24 (1986) 387–395. doi:10.1016/0008-6223(86)90257-5.
- [154] A. Gupta, I.R. Harrison, New aspects in the oxidative stabilization of PAN-based carbon fibers, *Carbon N. Y.* 34 (1996) 1427–1445. doi:10.1016/S0008-6223(96)00094-2.
- [155] Y. Liu, S. Kumar, Polymer/Carbon Nanotube Nano Composite Fibers—A Review, (2014). doi:10.1021/am405136s.
- [156] B.A. Newcomb, P. V. Gulgunje, K. Gupta, M.G. Kamath, Y. Liu, L.A. Giannuzzi, H.G. Chae, S. Kumar, Processing, structure, and properties of gel spun PAN and PAN/CNT fibers and gel spun PAN based carbon fibers, *Polym. Eng. Sci.* 55 (2015) 2603–2614. doi:10.1002/pen.24153.
- [157] A. Gupta, I.R. Harrison, New aspects in the oxidative stabilization of PAN-based carbon fibers, *Carbon N. Y.* 34 (1996) 1427–1445. doi:10.1016/S0008-6223(96)00094-2.
- [158] E. Fitzer, D.J. Müller, The influence of oxygen on the chemical reactions during stabilization of pan as carbon fiber precursor, *Carbon N. Y.* 13 (1975) 63–69. doi:10.1016/0008-6223(75)90259-6.
- [159] Q. Ouyang, L. Cheng, H. Wang, K. Li, Mechanism and kinetics of the stabilization reactions of itaconic acid-modified polyacrylonitrile, *Polym. Degrad. Stab.* 93 (2008) 1415–1421. doi:10.1016/j.polymdegradstab.2008.05.021.

- [160] H. Chang, M. Lu, J. Luo, J.G. Park, R. Liang, C. Park, S. Kumar,
Polyacrylonitrile/boron nitride nanotubes composite precursor and carbon fibers,
Carbon N. Y. 147 (2019) 419–426. doi:10.1016/j.carbon.2019.03.026.
- [161] H.E. Kissinger, Reaction Kinetics in Differential Thermal Analysis, Anal. Chem.
29 (1957) 1702–1706. doi:10.1021/ac60131a045.
- [162] C.P. Reghunadhan Nair, K. Krishnan, K.N. Ninan, Differential scanning
calorimetric study on the Claisen rearrangement and thermal polymerisation of
diallyl ether of bisphenols, Thermochim. Acta. 359 (2000) 61–67.
doi:10.1016/S0040-6031(00)00504-9.
- [163] O. Nder Yargı, S. Aziye Ugur, O. Nder Pekcan, Temperature Dependence of
Oxygen Diffusion Into Polymer/Carbon Nanotube Composite Films, (n.d.).
doi:10.1002/pen.22061.
- [164] J. Simitzis, S. Soulis, Correlation of chemical shrinkage of polyacrylonitrile fibres
with kinetics of cyclization, Polym. Int. (2008). doi:10.1002/pi.2322.
- [165] Y. Wang, B. Fugetsu, Z. Wang, W. Gong, I. Sakata, S. Morimoto, Y. Hashimoto,
M. Endo, M. Dresselhaus, M. Terrones, Nitrogen-doped porous carbon monoliths
from polyacrylonitrile (PAN) and carbon nanotubes as electrodes for
supercapacitors, Sci. Rep. 7 (2017) 40259. doi:10.1038/srep40259.
- [166] C. Dollinger, Bandwidth study on energy use and potential energy saving
opportunities in manufacturing food and beverages, in: Sustain. Eng. Forum 2016 -
Core Program. Area 2016 AIChE Annu. Meet., 2016: pp. 103–114.

https://www.energy.gov/sites/prod/files/2017/12/f46/Carbon_fiber_bandwidth_study_2017.pdf (accessed September 22, 2019).

- [167] P.-H. Wang, S. Ghoshal, P. Gulgunje, N. Verghese, S. Kumar, Polypropylene nanocomposites with polymer coated multiwall carbon nanotubes, *Polymer* . 100 (2016) 244–258. doi:10.1016/j.polymer.2016.07.070.
- [168] M.K. Jain, M. Balasubramanian, P. Desai, A.S. Abhiraman, Conversion of acrylonitrile-based precursors to carbon fibres, *J. Mater. Sci.* 22 (1987) 301–312. doi:10.1007/BF01160585.
- [169] Y. Liu, H.G. Chae, S. Kumar, Gel-spun carbon nanotubes/polyacrylonitrile composite fibers. Part I: Effect of carbon nanotubes on stabilization, *Carbon N. Y.* 49 (2011) 4466–4476. doi:10.1016/j.carbon.2011.06.043.
- [170] Y. Liu, H.G. Chae, S. Kumar, Gel-spun carbon nanotubes/polyacrylonitrile composite fibers. Part III: Effect of stabilization conditions on carbon fiber properties, *Carbon N. Y.* 49 (2011) 4487–4496. doi:10.1016/j.carbon.2011.06.045.
- [171] Vincent P. Kelly, *Energy Costs in Carbon Fiber Production*, (n.d.).
<http://www.carbon-fiber.com/eccf.pdf> (accessed September 22, 2019).
- [172] P. Smith, P.J. Lemstra, Ultra-high-strength polyethylene filaments by solution spinning/drawing, *J. Mater. Sci.* 15 (1980) 505–514. doi:10.1007/BF02396802.
- [173] R. Schaller, K. Feldman, P. Smith, T.A. Tervoort, High-Performance Polyethylene Fibers “Al Dente”: Improved Gel-Spinning of Ultrahigh Molecular Weight

Polyethylene Using Vegetable Oils, *Macromolecules*. 48 (2015) 8877–8884.

doi:10.1021/acs.macromol.5b02211.

[174] H.H. Winter, Can the gel point of a cross-linking polymer be detected by the G' – G'' crossover?, *Polym. Eng. Sci.* 27 (1987) 1698–1702.

doi:10.1002/pen.760272209.

[175] C.M. Hansen, *Hansen Solubility Parameters A User's Handbook*, 2nd ed., CRC Press, 2007. <https://www.taylorfrancis.com/books/9780429127526> (accessed October 18, 2020).

[176] U. Tilstam, Sulfolane: A Versatile Dipolar Aprotic Solvent, *Org. Process Res. Dev.* 16 (2012) 1273–1278. doi:10.1021/op300108w.

[177] Z. Wangxi, L. Jie, W. Gang, Evolution of structure and properties of PAN precursors during their conversion to carbon fibers, *Carbon N. Y.* 41 (2003) 2805–2812. doi:10.1016/S0008-6223(03)00391-9.

[178] O. Takashi, I. Koichi, M. Naomasa, Process for preparing a carbon fiber of high strength, US4925604A, 1985.

[179] T. Kobashi, S. Takao, High strength polyacrylonitrile fiber and method of producing the same, US4535027A, 1984.

[180] P.H. Lindenmeyer, R. Hosemann, Application of the Theory of Paracrystals to the Crystal Structure Analysis of Polyacrylonitrile, *J. Appl. Phys.* 34 (1963) 42–45. doi:10.1063/1.1729086.

- [181] B.R. Bird, W.E. Stewart, E.N. Lightfoot, *Transport Phenomena*, 2nd ed., Wiley, 2007.
- [182] H.S. Carslaw, J.C. Jaeger, *Conduction of Heat in Solids*, Second Edi, Oxford at the Clarendon Press, 1959.
- [183] S. White, *Fundamental Studies of Stabilization of Polyacrylonitrile Precursor*, Masters Theses. (2005). https://trace.tennessee.edu/utk_gradthes/4601 (accessed July 16, 2019).
- [184] R. Perry, *Chemical engineering handbook*, manual, 2007.
- [185] D. Liu, C. Zhong, Modeling of the heat capacity of polymers with the variable connectivity index, *Polym. J.* 34 (2002) 954–961. doi:10.1295/polymj.34.954.